![HITIT UNIVERSITY]

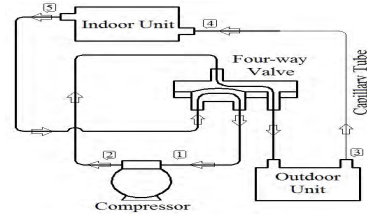JOURNAL OF SCIENCE & ENGINEERING

HITTITE

Volume 4, Issue 2, 2017

In this study, influence of hydrolic pressure or gas pressure on the powder injection molding of 316L stainless steel was investigated. Variations in the microstructure, hardness and density of the porduced samples were discussed in the frame of presure type.

50 μm

In this study, previously synthesized Ni (II) phthalocyanine compound bearing 2,10,16,24-tetrakis(2-isopropyl-5-methylphenoxy group was chosen for its interaction with calf thymus-DNA.

In this study, the values obtained by heat and humidity sensors which are placed in different locations of agricultural field are transmitted to a database by using a central operation unit. The water requirement based on the product is determined according to that database.

The potential of an arid-land plant, Euphorbia rigida (E. rigida), for the removal of heavy metals [Pb(II), Zn(II), Cu(II), Cd(II), Ni(II)] from aqueous solutions was studied in the current work.

In this study, a novel In-Drum Brushless Direct Current (ID-BLDC) motor is proposed to Eddy Current Separator (ECS) which separates nonferrous metals from waste. The ECS's separation efficiency depends on magnetic drum speed.

TRIP parameter (K) is determined experimentally for both martensitic and bainitic transformations by using the stressed dilatometry technique. A new method for extraction of for an incomplete transformation is suggested for the martensitic transformation

HITTITE

JOURNAL OF SCIENCE & ENGINEERING

This new issue of Hittite Journal of Science and Engineering contains twelve manuscripts from the disciplines of chemistry, mathematics, chemical engineering, electrical and electronics engineering, materials science and engineering, mechanical engineering. These manuscripts was first screened by Section Editors using plagiarism prevention software and then reviewed and corrected according to the reviewer's comments. I would like to express my gratitude to all our authors and contributing reviewers of this issue.

I would like to thank to the President of Hitit University, Dr. Reha Metin Alkan, for his constant interest in HJSE and also to the Associate Editors of HJSE, namely Dr. Dursun Ali Kose and Dr. Oncu Akyildiz, as well as our Production Editors Dr. Kazim Kose, Mustafa Guzel and Mustafa Resit Haboglu for their invaluable efforts in making of the journal.

It's my pleasure to invite the researchers and scientists from all branches of science and engineering to join us by sending their best papers for publication in Hittite Journal of Science and Engineering.

Dr. Ali Kilicarslan

Editor-in-Chief

Influence of Pressure Type on Powder Injection Moulding of Stainless Steel (316L) Powder

Yunus Türen
Karabuk University, Department of Metallurgical and Materials Engineering, Karabuk, Turkey

ABSTRACT

In this study, influence of hydrolic pressure or gas pressure on the powder injection molding of 316L stainless steel was investigated. Variations in the microstructure, hardness and density of the porduced samples were discussed in the frame of presure type. In the injection molding applied molding pressure, ratio of powder/binder, binder leacing time, sintering temperature also were examined. Experimental works showed that the gas pressure system was observed to be more effective than hydrolic pressure system for each parameters. Experimental results also showed that the powder ratio in the feedstock and sintering temperature had dominant effect on hardness and microstructure of the samples. The leaching time of Polyethylene Glycol (PEG) 600 binder has been decreased with increasing molding pressure. Increasing hardness and density of samples were achieved by increasing metal powder ratio. The increasing in hardness and density were also observed by increasing sintering temperature.

Keywords:
Powder injection molding; Hydrolic pressure system; Gas pressure system; Debinding times; Sintering temperature; Powder/binder ratio.

INTRODUCTION

Powder injection molding (PIM) used in the production of small-sized complex machine parts, prostheses and medical device parts is a method of filling metal or ceramic powders into molds with the aid of a binder or carrier[1-4]. Powder and binder mixtures prepared for powder injection molding are called "feedstock". In order to obtain the feedstock, metal and ceramic powders are mixed with thermoplastic binders and other additives. Nowadays water and many inorganic materials are successfully used as the other additives. The amount of binder varies from 15% to 50% in volume [2]. In practice, feedstocks containing numerous binders and similar additives are multifunctional systems. Figure 1 shows flow chart steps of the PIM process. Firstly, the appropriate selected powder/binder is mixed and then granulated. The granular mixture is placed into the injection machine.

The mixture coming to the toothpaste consistency is delivered to the cavity of the mold which is connected to the injection machine with a suitable pressure at given temperature.Thereby the green part is obtained by taking the shape of the mold. In the next step of the process the binder is removed from the green part. The removing process can be carried out in essentially two different ways. The decomposition of the binder is carried out with firstly the solvent and then thermally. After removing the binder from the green part sintering is performed.Sintering should be carried out in a suitable atmosphere to prevent losses of critical elements, such as carbon in the steel, from being degraded by nitrogen or oxygen. At the end of the sintering process, a part is found which is almost completely dense and has a relatively low porosity level. By appropriate separation and sintering it is possible to obtain 90-99% of the theoretical density of the material. Mechanical properties of the fully dense parts are similar to that of the as-cast and/or forged parts[3].

Therefore, the PIM method has important advantages over other methods for the production of advanced parts with complex shapes. The main advantages of PIM are related to lower costs and shorter debinding time. The PIM enables to mold metal/ceramic parts with soft and low cost molds. For the fabrication of samples without cracks and distortion, the rheological behaviour of feedstock is very important [5–7]and it is clearly influenced by powder characteristics and binder
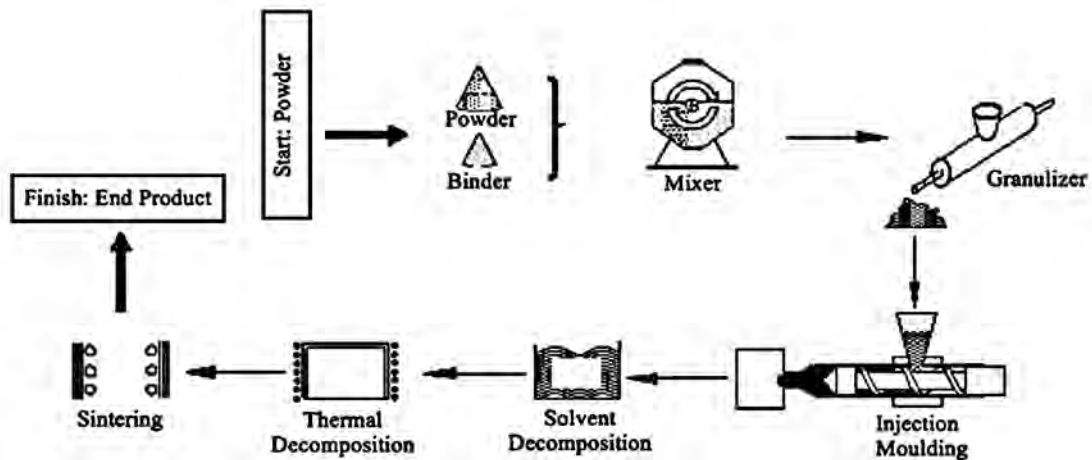
Figure1. Manufacturing process of powder injection moulding [2].

properties. The knowledge of characteristics of powder and binder is essential for successful PIM manufacturing [8]. PIM of stainless steels has been widely investigated[9-11]. In spite of various studies [7-11] on the PIM, a systematic investigation on the effect of processing parameters with gas and/or hydraulic piston pressure have not been reported. Thus, the present work was performed to investigate the effect of applied molding pressure, ratio of powder/binder, binder leacing time, sintering temperature on the density, hardness and microstructureof samples in two different (gas or hydrolic) pressurized molding system

EXPERIMENTAL

In experimental studies 316L stainless steel powder sized with 45 µm produced by water atomization method were used. A water-soluble mixture of 80% PEG 600 and 20% PMMA was used as the binder.The binder and powder mixtures (50%, 52% and %54 of solid volume ratio) were first dried and then mixed in semi-solid state on the heating plate. The prepared binding powder mixtures were injected into the mold of the PIM.In order to injection of the powder materials, two types of molding systems were used as given in Figure 2.During the filling

feedstock into the mold in the molding process, the feedstock and the mold temperature were held constant at 160 °C and 60 °C, respectively.Molten feedstock was injected into the mold cavity by means of the hydraulic and/or gas pressureunder 20, 30 and 40 bar.After that the binder (PEG 600) was dissolved in a ceramic pot filled with distilled water at 60 °C for different times (2-6h). Termal removing of binder(PMMA) was carried outin an argon atmosphere controlled furnace at 360 °C for 1.5 hours and then sintering was performed at different temperatures (1250, 1300, 1350 °C).Density measurement was taken before and after sintering in the device with AD-1653 density kit.Microstructural characterization of the investigated samples was carried out by Nicon Epiphot 200 model optical microscopy. In the microscopic examination studies, the samples ground and polished with standard metallographic methods were electrolytically etched in the oxalic acid solution under 1.5 volts for 15 seconds.The hardness measurements were determined using Schimatzu HMV-2 microhardness machine having Vickers indenter under 10 g.load.

RESULTS AND DISCUSSION

Changes in the binder (PEG 600) loss are given in Figure 3 with respect to the water dissolving times and the molding pressure. As seen Figure 3, the loss of the binder in each molding pressure appears to be insoluble after 6 hours.Also it has been determined in Figures 3 that applied the molding pressure is an important factor for PEG 600 weight loss. The PEG 600 loss decreased with increasing the molding pressure in accordance with Ref. [12].

Figure 4 shows SEM images of samples before and after the binder dissolution. It is seen that the 316L stainless steel powders are coated with the binder mixtures
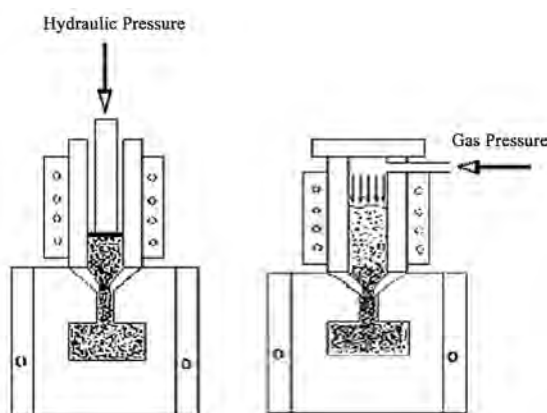

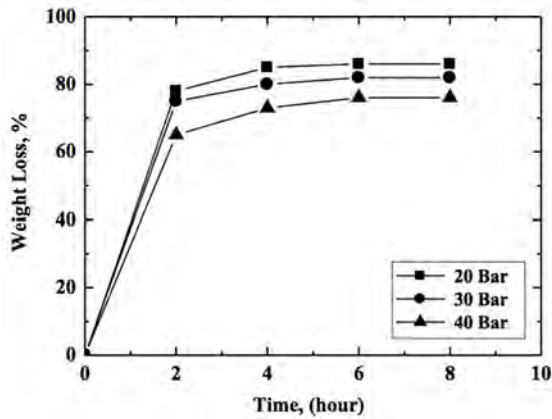**Figure 2.** Moulding systems of powder injection moulding machine.

Figure3. PEG loss as a function of leaching time and pressure (solid volume fraction: 50%)

(PEG + PMMA) before the dissolution.Figure 4b shows the formation of voids and channels between powders by dissolution of PEG 600 obtained after 6 hours at 60 °C. During the dissolution, the PMMA remains in the structure and provides the connection of the powder particles with each other.The smilar results were reported by Omar et al. [13,14]. The presence of void and channels between powders helped burning out of the PMMA during thermal dissolution and prevented distortions owing to gas expansion.
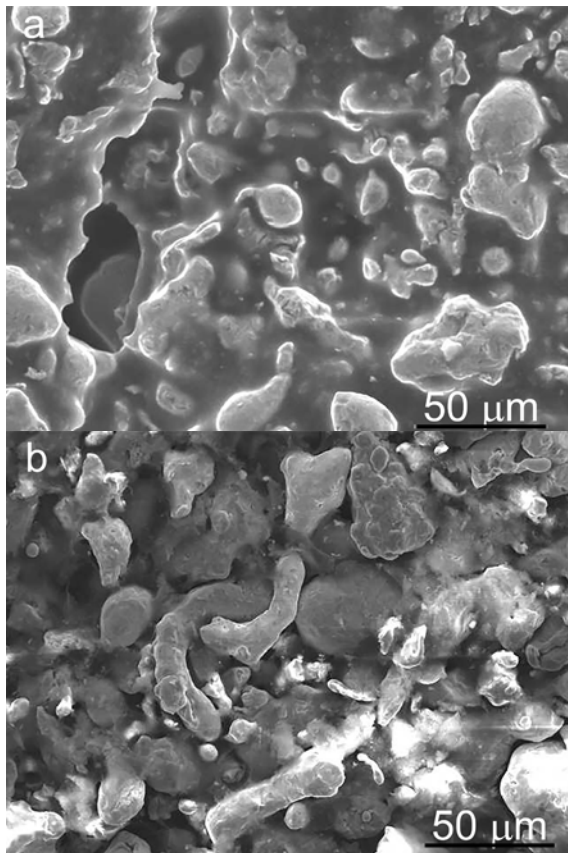
Figure4. 316L stainless steel samples (a) before and (b) after dissolution process (500X).
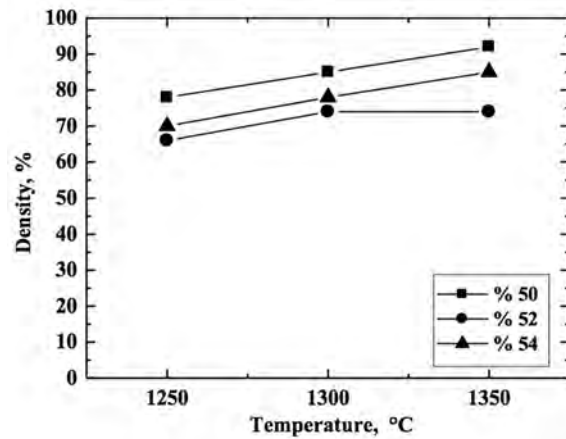
(a) Method: Gas pressure
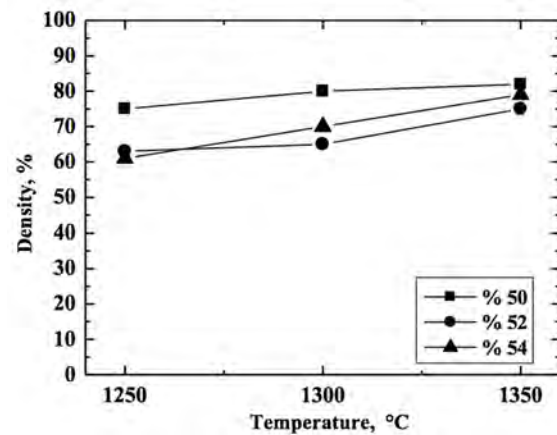
(b) Method: Hydraulic pressure

Figure 5. Density change as a function of sintering temperature.

It is shown in Figure 5 that the density increases with sintering temperature and decreases with solid volume ratio in two different systems. Figure 5 shows that the density of the samples with 50 % solid volume ratio sintered at 1350 °C is 83% for the hydraulic system (Fig 5b) and 92% for the gas system (Fig. 5a). This can be attributed to the closed of the gaps and insufficient binder for packaging by hydrolic pressure. It has also been reported in the literature [14] that when the amount of binder increased from 10% to 25%, the sintering density rised from 92 % to 95%.It is reported that [12] addition of fewer binders caused powder to lock between each other due to insufficient sliding during the flow.

It has been observed in Figure 6 that the hardness increases with sintering temperature and decreases with increasing solid volume ratio in both molding systems. As seen in Figure 6, the hardness of samples produced by gas press is higher at 1350 °C.Omar et al. [14] also indicated that the hardness of the samples would increase due to the better condensation with increasing binder ratio and sintering temperature.
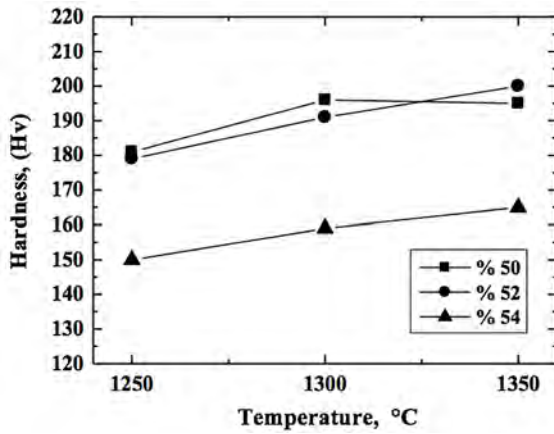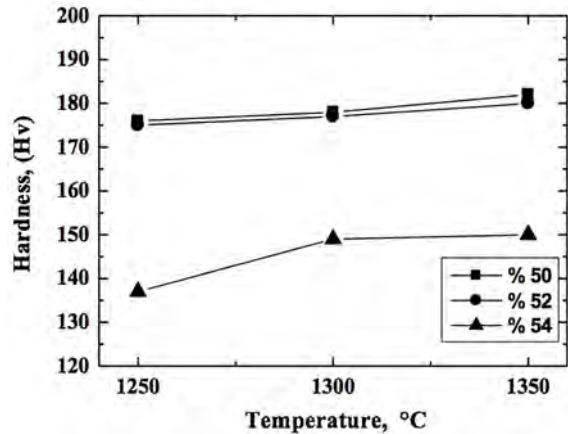
(a) Method: Gas pressure   (b) Method: Hydraulic pressure

Figure 6. Hardness change as a function of sintering temperature.

In this study in contrast to the gas pressure system, hydrolic system led to the heterogenus powder distrubution(Figure 7). This can be explained with pushing the binders towards the edge zone of the mold by the effect of the hydraulic pressure and forming too many gaps at the edges after the binders dissolution during sintering.

The sintering applied at 1250 ^{o}C led to the very porous microstructure (Figure 8a). As the sintering temperature increased, the pores disappeared and the powder grains bonded to each other better (Figure 8b). When the sintering temperature reached to 1350 ^{o}C grain growth was be more significient (Figure 8c). Relaeted to increased sintering temperature the pores decreased and became more spherical. This is supported by the literature [15,16].

EDGE SECTION   CENTER SECTION

Figure 7. Optical microstructures of the samples with a volume fraction of 50% produced by hydraulic and gas pressure methods.

(a) 1250 ºC

(b) 1300 ºC
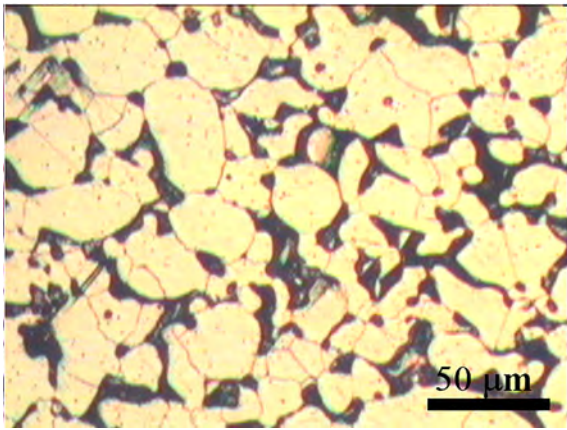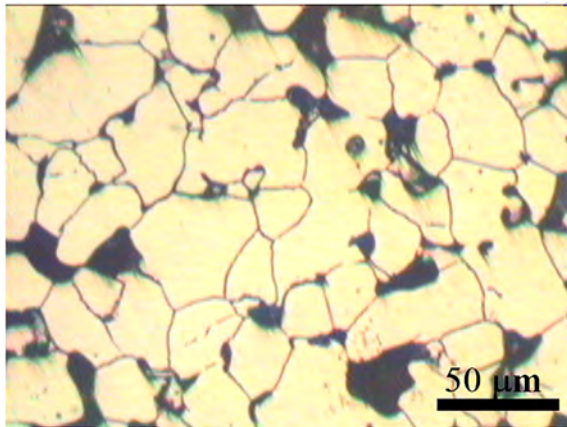
(c) 1350 ºC

Figure 8. Optical microstructures of the samples with a volume fraction of 50% sintered at (a) 1250 ºC, (b) 1300 ºC and (c) 1350 ºC for 1 h.

CONCLUSION

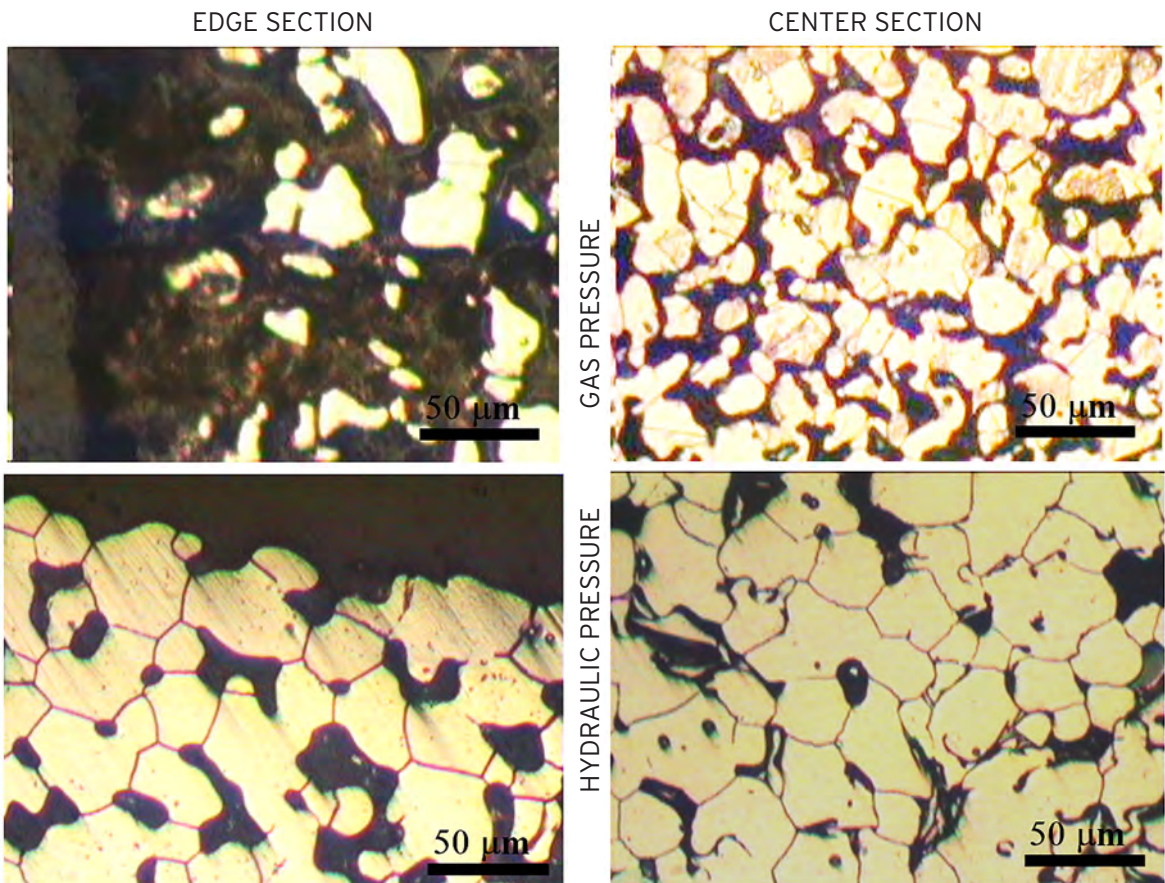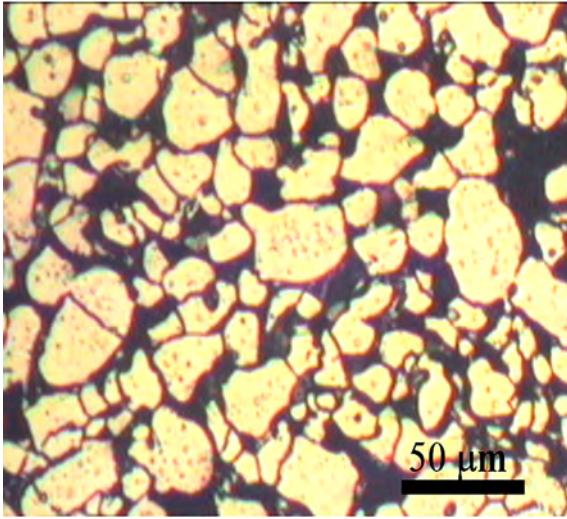The results of the experimental studies can be summarized as follows

1. Experiment results showed that the 6 hours leaching time for both molding systems is sufficient to dissolve the PEG 600 binder.
2. Hydrolic pressure system has pushed the binders towards the edge zone of the mold and formed excessive gaps at the edges after the binders dissolution during sintering.
3. In both molding systems, the hardness and density of the samples increased with sintering temperature and decreased with solid volume ratio.
4. It has been shown that the samples produced by the gas pressure system in the experiments exhibited a homogeneous distribution of the powder in the microstructure compared to the hydraulic pressure system.

REFERENCES

1. Candan E. Injection Molding of Co–Cr–Mo Powder with a Novel Binder System, M. Sc. Thesis, Engineering Materials Faculty of Engineering the University of Sheffield, 1994.
2. German RM. Powder Injection Moulding, Metal Powder Industries Federation, Princeton, NJ, ABD 1990.
3. Cornwall RG, German RM. An analysis of the powder injection molding industry global market Advances in Powder Metallurgy and Particulate Materials. Proceeding of International Conference (PM2TEC 2000), Compiled by H. Ferguson and D. T. Whychell, Metal Powder Industries Federation, Princeton, N J, USA, 4, pp. 55–60, 2000.
4. Gökten M. Stearit ve 316L Paslanmaz Çelik Tozları ile PEG Ağırlıklı Reçinelerden Meydana Gelen Besleme Stoklarının Reolojik Özelliklerinin İncelenmesi, M. Sc. Thesis, Gazi University Institute of Natural and Applied Sciences, Ankara, 2003.
5. Huang YLB, Qu, X. Viscosity and melt rheology of metal injection molding feedstocks. Powder Metallurgy 42 (1) (1999) 86–90.
6. Agote I, Odriozola A, Gutiérrez M, Santamaría A, Quintanilla J, Coupelle P, Soares, J. Rheological study of waste porcelain feedstocks for injection moulding. Journal of the European Ceramic Society 21 (2001) 2843-2853.
7. Suri P, Atre SV, German RM, Souza, JP. Effect of mixing on the rheology and particle characteristics of tungsten–based powder injection molding feedstock. Materials Science and Engineering A 356 (2003) 337-344.
8. Ahn S, Park SJ, Lee S, Atre SV, German, RM. Effect of powders and binders on material properties and molding parameters in iron and stainless steel powder injection molding process. Powder Technology 193 (2009) 162-169.

Y. Türen / Hittite J Sci Eng, 2017, 4 (2) 85–90

9. Li YM, Liu SJ, Qu XH, Huang, B. Thermal debinding processing of 316L stainless steel powder injection molding compacts. Journal of Materials Processing Technology 137 (2003) 65-69.

10. Koseski RP, Suri P, Earhardt NB, German RM, Kwon YS. Microstructural evolution of injection molded gas–and water–atomized 316L stainless steel powder during sintering. Materials Science and Engineering 390 (2005) 171-177.

11. Berginc B, Kampus Z, Sustarsic, B. Influence of Feedstock Characteristics and Process Parameters on Properties of MIM Parts Made of 316L. Powder Metallurgy 50 (2) (2007) 172-183.

12. Oğulcu F. Toz Enjeksiyon Kalıplamada Besleme Stoğunun Akıcılığına İşlem Parametrelerinin Etkisi, M. Sc. Thesis, Gazi University Instiute of Natural and Applied Sciences, Ankara, 2006.

13. Omar MA, Ibrahim R, Sidik MI, Mustapha M, Mohamad, M. Rapid debinding of 316L stainless steel injection moulded component. Powder Metallurgy Programme, Malaysia 140 (2003) 397–400.

14. Omar MA, Davies HA, Messer PF, Ellis, B. (2001) The influence of PMMA content on the properties of 316L stainless steel MIM compact. Powder Metallurgy Group, Advanced Materials Research Centre, SIRIM Berhad, Lot 34, Man 2∕3, Kulim Hi– Tech Park, 09000 Kulim, Kedah, Malaysia Department of Engineering Materials, University of Sheffield, Sir Robert Hadfield Building, Mappin Street, Sheffield SI 3TD, UK, 477, pp. 4–81, 2001.

15. Kurt AO. Lecture Notes, Sakarya University Engineering Faculty Metallurgical and Materials Engineering Department, Sakarya, 2003.

16. Ji CH, Loh NH, Khor KA, Tor, SB. Sintering study of 316L stainless steel metal injection molding parts using Taguchi method: final density. School of Mechanical & Production Engineering, Nanyang Technological University, 50 Nanyang Avenue, Singapore, 311, pp. 74–82, 2000.

Study on DNA Binding Properties of Nickle (II) Phthalocyanine Compound with 2-Isopropyl-5-Methylphenoxy Substituents.

Ali Arslantaş[1] and M. Salih Ağırtaş[2]
[1] Karabuk University, Department of Biomedical Engineering, Karabuk, Turkey
[2] Yüzüncü Yıl University, Department of Chemistry, Van, Turkey

ABSTRACT

In this study, previously synthesized Ni (II) phthalocyanine compound bearing 2,10,16,24-tetrakis(2-isopropyl-5-methylphenoxy group was chosen for its interaction with calf thymus-DNA. Calf thymus-DNA was used to determine DNA binding properties of Ni (II) phthalocyanine compound. The DNA binding activities of Ni (II) phthalocyanine compound bearing 2-isopropyl-5-methylphenoxy substituent was investigated by using absorption titration, fluorescence emission, cyclic voltammetry, gel elctrophoresis in Tris-HCl buffer at pH 7.0. In addition to above methods, melting point and viscosity experiment were performed to determine the DNA intercation of the compound in Tris-HCl buffer solution. The results showed that Ni (II) phthalocyanine compound binds strongly to calf thymus-DNA via intercalation binding.

Keywords:
Uv-Vis spectroscopy; DNA binding; phthalocyanines; cyclic voltametry; electrophoresis.

INTRODUCTION

Phthalocyanine compounds show important features such as chemical stability, eminent thermal, dense luminescence, and electron transfering impact [1, 2]. Feasibilities of phthalocyanine compounds have been studied in terms of varied fields, in photodynamic therapy, therapeutical drug and antioxidant properties [3]. Metallophthalocyanine compounds indicate unique electrochemical, physical properties due to their large correlated π regulations that are kept in close affinity with metallic ions [4-6]. The derivatives of phthalocyanine compounds are very suitable tool for photodynamic cancer therapy [7]. For this reason, nowadays, the biological studies of phthalocyanine metal compounds for anticancer treatment have been increased because of their effects in medical treatment [8].

For treatment of genetic diseases such as cancer, DNA molecule is a signifacant target in cancer therapy. Nowadays, transition metal complexes have gained great attatention as anticancer medicine due to their significant effect in medical treatment. Some cancer medicines give an important beginning information about the mechanism of DNA interaction. Transition metal compounds have multiple electrochemical and spectral characteristics which increase their DNA cleavage properties and DNA interaction [9, 10]. DNA molecule has been a substantial target for treatment of genetic disorders such as cancer disease. The interaction probe of phthalocyanine metal compounds with DNA not only ensures an opportunity to find out the intercation methods of some antitumor but also permits to design new DNA targeted phthalocyanine metal compounds [9, 10]. The many studies conducted so far targeting the DNA molecule is a significant intracellular targets of medications interaction of tiny chemical compounds with DNA results in DNA harm, disrupting the division of cell and cell death. As a consequence, the interreactivity of chemical compounds by DNA molecule is an important study area for the developing of novel curing drugs [11].

In this study, we studied the interaction of previously synthesized Ni (II) phthalocyanine compound (**PcNi**) bearing 2-isopropyl-5-methylphenoxy group which is synthesized and characterized according to literature procedure [2], substituents on the peripherial positions by calf thymus-DNA using absorption spectra, fluorescence spectroscopies, cyclic voltammetry, gel

electrophoresis, thermal denaturation profile and viscosity measurement in a Tris-HCl buffer solution (pH 7.0).

METHODS

Chemicals and equipments

In this work, Ni (II) phthalocyanine compound bearing 2-isopropyl-5-methylphenoxy substituent was used. Calf Thymus-DNA (CT-DNA), and Tris-HCl were provided from Sigma Aldrich company. Sodium chloride (NaCl) was purchased from Merck. All chemical compounds were analytical grade and used without further purification. All CT-DNA solutions were prepared by using Milli-Q water. The experiments were carried out in an the medium of Tris-HCl buffer solution at pH 7.0.

UV-Vis spectroscopy studies of binding activities of Ni (II) phthalocyanine compound (**PcNi**) with the DNA were performed in aquartz cuvette using Agilent Technologies Cary 60 UV/Vis spectroscopy (Karabuk, MARGEM, Turkey), fluorescence spectroscopy was conducted using Perkin Elmer LS Fluorescence Spectrometer and Cyclic voltametry (CV) experiments was carried using Ivisumstat Electrochemical Interface electrochemical analyzer. Agarose gel electrophoresis studies were performed with Thermo Owl electrophoresis system. Thermal denaturation profile was performed at 260 nm wavelenght using Agilent Technologies Cary 60 UV-vis spectrocopy and viscosity experiments were carried out using Ubbelohde viscositymeter.

Synthesis of compounds

The synthesis of 4-(2-isopropyl-5-methylphenoxy) phthalonitrile compound and the synthesis of 2,10,16,24-tetrakis(2-isopropyl-5-methylphenoxy phthalocyaninato) nickel(II) (PcNi) is synthesized and characterized according to literature procedure [2].

UV/Vis absorption spectra and fluorescence titration studies

Absorption tittration spectra for DNA binding properties were performed at room temperature at pH 7.0 in a 20 mM Tris-HCl buffer solution containing 20 mM NaCl. The concentration of CT-DNA was calculated by absorbance at 260 nm using a DNA molar extinction coefficient (ε) of 6600 $M^{-1}cm^{-1}$ indicating that the DNA solution was free of proteins [12]. Absorption titration experiments were carried out in the region of 300-800 nm. Absorption titrations of the compound at constant concentration of **PcNi** in Tris-HCl buffer were conducted by adding between 0 to 3.5 μM of CT-DNA. In order to determine the dilution impacts were carried out by control titrations with Tris-HCl buffer solution instead of DNA [13].

Following excitation fluorescence spectroscopy experiments were conducted in the region of 400-750 nm. Fluorescence titration of the compound with the DNA were carried out by increasing concentration of the DNA solution to the compound solution at fixed concentration. In this study, the solutions were allowed to reach to equilibrium for a certain time before measurements were performed [14].

Cyclic Voltammetry studies

Cyclic voltametry experiments at the glass carbon elctrode were carried out by using Ivisumstat Electrochemical Interface electrochemical analyzer at the following setting. Beginning potential was -1.5 V and ultimate potential was 1.5 V and the rate of scan was 10 mV/s. Carbon working electrode, Ag/AgCl reference electrode and plantinnum wire counter electrode were used in this work. A standard single chamber three electrode cell system of 10 mL capacity were used to conducted the all measurements [15, 16]. Cyclic voltametry experiments were performed at ambient temperature in a Tris-HCl buffer.

Melting point Temperature studies

Melting point studies were conducted for the DNA and **PcNi**. The compound and the DNA in Tris-HCl buffer comprising NaCl solution were heated from 20 °C to 95 °C gradually. UV-Vis absorption spectra values were recorded. Thermal denaturation temperature of the DNA was determined in the absence and presence of the compound. Thermal denaturation temperatures were recorded at 260 nm wavelenght [17] by using Agilent Technologies Cary 60 UV/Vis spectroscopy.

Viscosity measurements

In this work, the relative viscosity experiments of **PcNi** with CT-DNA were conducted by using Ubblohde viscometer which was sunmerged in a bathtub maitaining at a fixed temperature (30 °C). The proximate time of flow was achieved after each sample was tested three times. The relative viscosity of the DNA was computed by using $\eta_i=(t_i-t_0)/t_0$, where η_i is the viscosity values of the DNA; t_i is the time of flow of the solution in the absence and presence of the compound; and t_0 is the time of flow of Tris-HCl buffer solution (pH 7.0). The viscosity values were indicated as $(\eta/\eta_0)^{1/3}$ vs [**PcNi**] / [CT-DNA], where η is the relative viscosity of the DNA in the presence of compound and η_0 is the relative viscosity value of the DNA [18].

Agarose gel electrophoresis experiment

For gel electrophoresis study, CT-DNA in 20 mM Tris-HCl buffer at pH 7.0 containing 20 mM NaCl, was allowed to interact with **PcNi**.

The binding activities of the compound with the DNA were investigated by 1% agarose gel in Tris-HCl buffer EDTA (ethylenediaminetetraacetic acid) (TBE) solution. 20 µL of samples of DNA + **PcNi** was loaded with loading dye. Agarose gel electrophoresis experiment for DNA + **PcNi** sample was carried out at 80 volt during 3 hours in Tris -HCl buffer ethelendiaminetetraacetic acid (EDTA) (TBE) solution. After gel electrophoresis experiment, the DNA bands were visualized by using Vilber Lourmat UV lamb. For this experiment, Thermo owl gel electrophoresis sytem was used.

RESULTS AND DISCUSSION

Synthesis and characterization

Nickle (II) phthalocyanine compound was obtained by using 4-(2-isopropyl-5-methylphenoxy) phthalonitrile derivative. Ni (II) phthalocyanine compound bearing 2,10,16,24-tetrakis (2-isopropyl-5-methylphenoxy phthalocyaninato) Ni (II) was previously synthesized and characterized according to literature procedure [2]. The chemical structure of nickle (II) phthalocyanine compound bearing 2,10,16,24-tetrakis(2-isopropyl-5-methylphenoxy) group [2] is given in the following
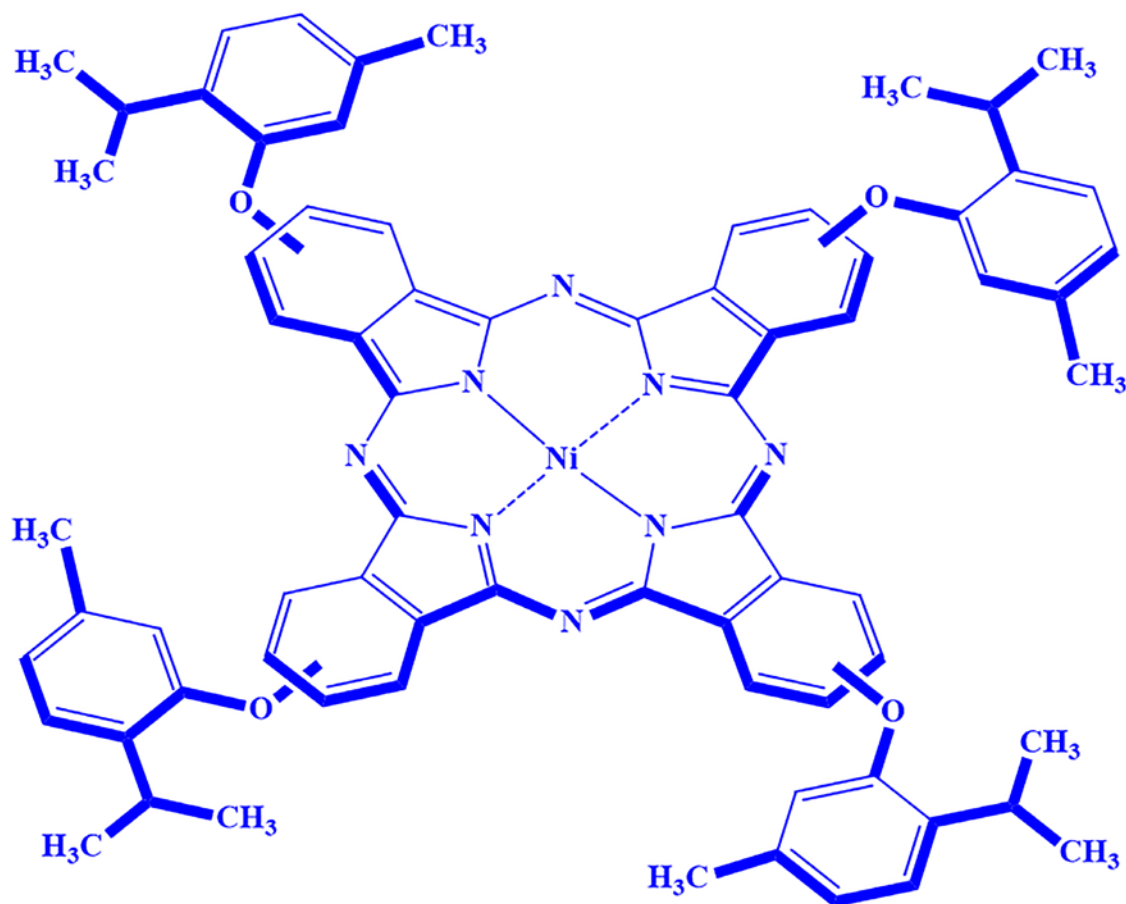
Fig. 1. The characterization of previously synthesized Ni (II) phthalocyanine compound was carried out by using NMR, FTIR and UV/Vis absorption spectroscopy analyses and their findings are in reference to literature [2].

The study of DNA-binding

Absorption spectra and fluorescence titration studies Phthalocyanine metal compounds indicate two types of absorption spectra band in the ground state. One of the these bands, which is renowned Q band, is sighted at about 600-750 nm in the visible area of spectrum because of the π→π* transition from HOMO (the highest occupied molecular orbital) to LUMO (the lowest unoccupied molecular orbital) of phthalocyanine ring. The other absorption band, which is known as B band, is observed in the ultraviolet region of spectrum at approximately 300-450 nm arising from deeper π levels to LUMO of the ring of phthalocyanine [9, 19]. Due to the intense absorption spectra in the red visible zone and high capacity in generating, metallophthalocyanines are found out to be considerably encouraging as an important photosensitizers.

Fig. 1. Chemical structure of nickle (II) phthalocyanine compound (**PcNi**).

Phthalocyanine metal compounds can bind to the DNA via intercalation and non-intercalative binding modes. In general, intercalation interaction of a tiny chemical compound with DNA causes changes in absorbance (hyperchromism or hypochromism) and a red or blue change in wavelength [19] of compound because of π-packing interaction between aromatic groups [20] in comparison with DNA non-intercalation binding mode causes small changes in absorbances and wavelengths in absorption spectra [9, 21]. Generally, an interaction such as intercalation binding mode is involved a hypochromism and a red shift [19].

Absorption titrations of **PcNi** in the absence and presence of the DNA were carried out to investigate binding activities of nickle (II) phthalocyanine compound with the DNA. In order to study the DNA binding properties of nickle (II) phthalocyanine compound, UV-Vis absorption titration was carried out between the range of 300 and 800 nm wavelengths. The absorption titration of **PcNi** in
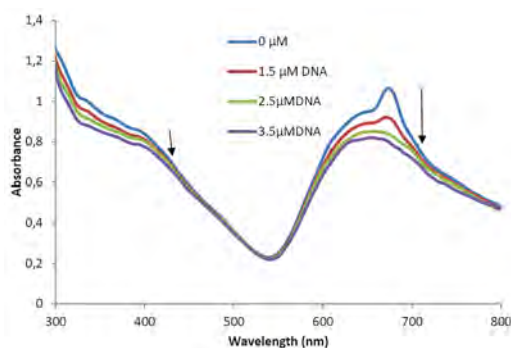
Fig. 2. UV/Vis absorption spectra of **PcNi** in Tris-HCl buffer solution at pH 7.0 on increasing amount of the DNA. The arrows indicate changes in absorbance on increasing amount of CT-DNA.

DMF was observed at about 678 for Q-band absorption and around 390 nm for B-band absorption in the absence of the DNA. Absorption titration of the compound showed hypochromism and red shifts in the presence of the DNA as shown in Fig. 2. As the amount of CT-DNA was increased from 0 to 3.5 μM, a strong hyprochromic change was observed with a small wavelength changing. The significant hypochromic change suggests that a strong interaction occures between nickle (II) phthalocyanine compound and the DNA molecule. These findings indicate that **PcNi** binds to the DNA via intercalative binding mode.

Fluorescence spectroscopy technique is also performed to determine binding activities between metal compounds and DNA [18]. Owing to fluorescence titration method is a prevalent and precision technique in the studies of DNA-binding, this method gives an important information about the binding activities between chemical compound and DNA molecules**.**
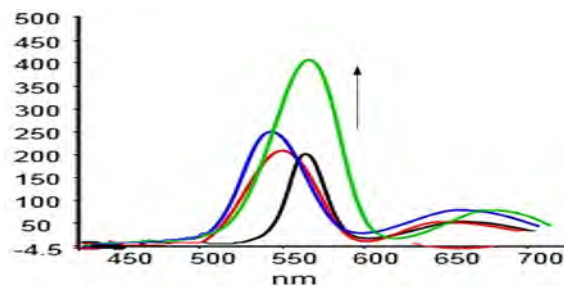
Fig. 3. Fluorescence emission titration of 1.5 μM **PcNi** (black curve) in the absence of CT-DNA in the buffer solution at pH 7.0. Tthe arrow indicates the intensity shift on increasing the DNA concentration (1.5 μM (red curve), 2.5 μM (blue curve) and 3.5 μM (green curve)), where **I** shows intensity.

As shown in Fig. 3, **PcNi** gives intense emission in the absence of DNA in a Tris-HCl buffer solution at ambient temperature with peak displaying at about 563 nm. On the addition of CT-DNA, a clear change in intensities of emission of the compound was observed comparing to the original for **PcNi** as indicated in Fig. 3. The compound gives emission at about 578 nm in the presence of CT-DNA. These results indicate that Ni (II) phthalocyanine compound interacts with CT-DNA in the buffer solution at 7.0.

Cyclic Voltammetry studies

Cyclic voltametry technique is largely operated to investigate binding activities between DNA and chemical compounds and it procures a substantial supplementary information to preliminary evaluated spectral studies [22]. This method is very practical for metal compounds because of their oxidation states. If metal compounds interact with DNA, peak potential and peak current of metal compound change in the presence of DNA molecule [23].

Cyclic voltametry measurements were performed to find out the binding activities between CT-DNA and **PcNi** in the buffer solution at pH 7.0 and the results were shown in Fig. 4. In this study, in the absence and presence of the DNA cyclic voltametric measurements were conducted. The compound has a couple of waves pertains to **PcNi** with the cathodic (EPc) and anodic peak potential (EPa) in the absence of CT-DNA. Anodic peak potential (EPa) and cathodic (EPc) potential were determined to be - 0.11 V (EPc) and - 0.52 V and 0.05 V (EPa) for the compound as shown in Fig. 4a.
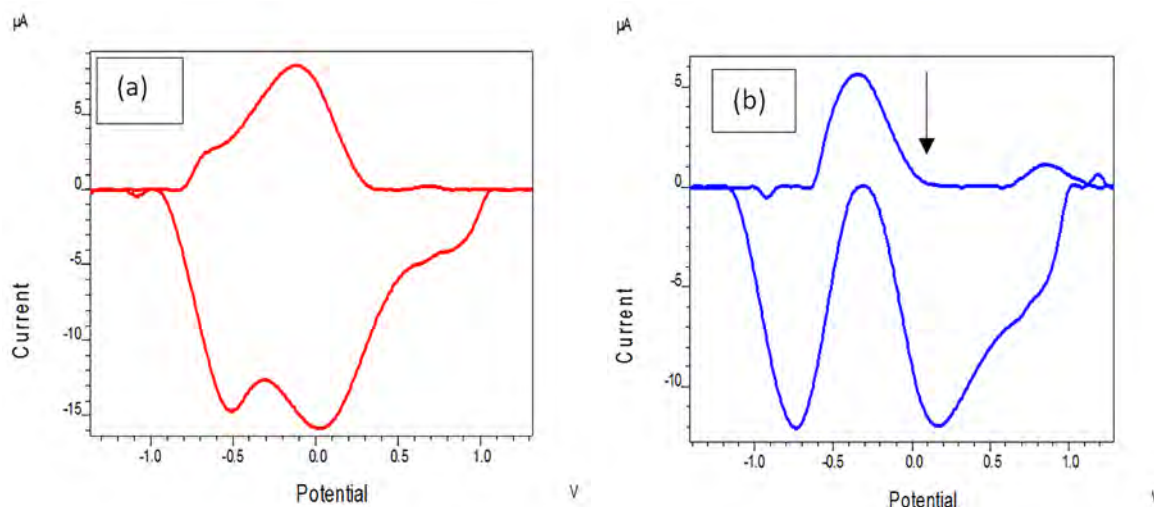
Fig. 4. Cyclic voltammogram of **PcNi** in the a) absence (red line) and b) presence (blue line) CT-DNA of increasing concentration of the DNA. The arrow shows decrease in cathodic peak on increasing amount of the DNA.

On the addition of CT-DNA to the compound, the cyclic voltametric peak currents in the presence of the DNA decreased substantialy. Cathodic peak potential (EPc) and anodic peak potential (EPa) were recorded to be − 0.34 V (EPc) and − 0.72 V and 0.18 V (EPa) for **PcNi** as indicated in Fig. 4b. These results show that the DNA interacts with the compound [24, 25]. In the presence of the DNA, the dropping of the voltametric peak current is referred to low diffusion of **PcNi** binding to CT-DNA. All these results demonstrate that Ni (II) phthalocyanine compound binds to CT-DNA.

Melting point temperature studies

Melting point temperature values for DNA can provide substantial information regarding DNA double helix stability along temperature at 260 nm. The intercalation binding mode of compounds with DNA molecule can cause to increase in melting temperature due to strength of binding mode. In process of non-intercalative interaction of compounds with DNA molecule can decrease melting point temperature [26, 27]. In this study, melting point experiments were conducted to investigate the interaction of compound **PcNi** with CT-DNA in the absence and presence of **PcNi** were indicated in Table 1. In the absence of the compound**,** melting point of the DNA was observed 73.58 ℃, and in the presence of the compound**,** melting point of the DNA was found to 82.82 ℃. The findings show that **PcNi** binds strongly to the DNA through intercalation binding owing to increase in melting point temperature.

Viscosity measurements

In general, binding modes between DNA and molecular compounds are determined by increasing and dropping of relative viscosity of DNA molecule after adding of compounds. An incerase in relative viscosity shows that

Table.1 In the absence and presence of Ni (II) phthalocyanine compound, melting point temperatures (T_m) of the DNA.

Sample	Melting point temperature (Tm)
CT- DNA	73.58 ℃
CT-DNA + PcNi	80.82 ℃

compounds interact with DNA via intercalative binding mode and DNA base pairs which induces disintegration and elongation of DNA molecule and decreasing in the relative viscosity shows that compounds have non-intercalation interaction between base pairs of DNA. This disintergation of DNA molecule arises from the packing of the ligands between DNA base pairs. The packing of compounds between the base pairs causes a significant change in the structure of DNA molecule [13, 28]. In this work, viscosity measurements were performed in the absence and presence of **PcNi** to investigate binding mode of the compound. Fig. 6 indicates that there is incease in CT-DNA relative viscosity after the inceasing in the amount of **PcNi** because of its successive addition. The findings demonstrate that the compound interacts with the DNA through intercalation binding mode.
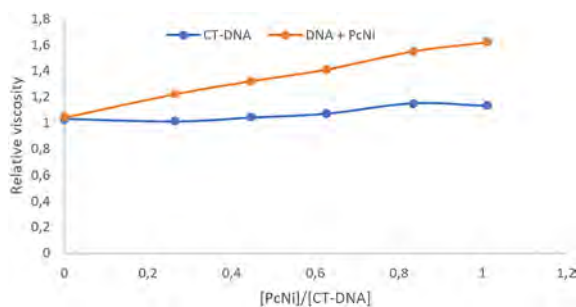

Fig. 6. In the absence and presence of Ni (II) phthalocyanine compound, relative viscosity of the DNA.

Gel Electrophoresis Studies

In this study, agarose gel electrophoresis experiments [27, 29] was conducted to investigate interaction of compound **PcNi** with CT-DNA at room temperature in the absence and presence of the previously synthesized the compound. The interaction of **PcNi** with the DNA was conducted to investigate the effects of varied concentration of the compound on the DNA using gel electrophoresis. The results are indicated in Fig. 7. As compared to band of control DNA (C), the results show that the intensity of the DNA bands were dropped after binding of the compound to DNA. The dropped in intensity of the DNA bands after interaction **PcNi** with the DNA is thought to be deformation of DNA double stranded [30].

The gel electrophoresis experiments clearly showed that Ni (II) phthalocyanine compound interacted with the DNA as there was shift in lane 1-3 bands as compared to CT-DNA control (C) as shown in Fig. 7. The interaction of the compound as compared with that of C is because of its efficient the DNA binding ability. As indicated in Fig. 7, it
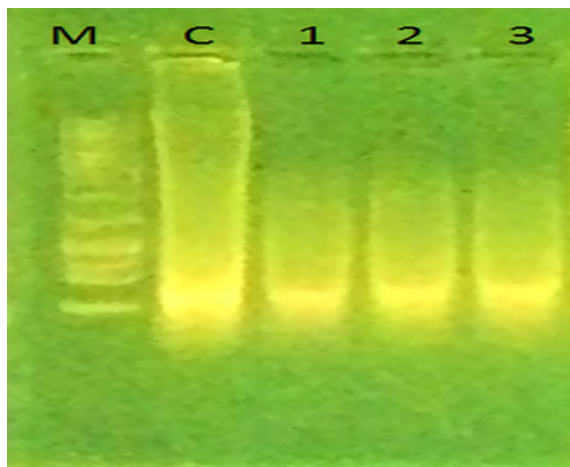

Fig. 7. Agarose gel electrophoresis of CT-DNA in the absence and presence of **PcNi** in a Tris-HCl buffer at pH 7.0. Lane M: DNA Marker; lane C: control DNA; Lanes 1-3: -DNA + **PcNi** (20 µM), respectively.

was found that DNA control (Lane C) band did not indicate any remarkable change of the band of lane C. Lane 1, 2 and 3 belong to **PcNi**. It was clearly seen that the compound interacted with the DNA as compared with the control DNA (C). In addition to this, the interaction of the compound with the DNA caused partial DNA neutralization [31]. The exsiting of smearing in gel diagram showed some cleavage as seen in Fig.7 and the cleavage effect of **PcNi** is comparable to that of C band is due to its effective interaction ability with DNA. As a result, these results indicate that compound Ni (II) phthalocyanine compound can strongly interact with CT-DNA.

CONCLUSION

The binding activities of Ni (II) phthalocyanine compound with the DNA were investigated using UV/Vis absorption spectra and fluoresence titration and the findings showed that the compound interacts strongly with the DNA molecule. The big change in melting point of DNA after binding of the compound also confirms intercalation binding. Cyclic voltametric experiment values indicate that the clear negative peak potentials were recorded on the addition of the DNA also support the intercalation binding of the compound to DNA. Gel electrophoresis experiments also showed that the compound interacts strongly with DNA. The results obtained from viscosity measurements also supports intercalation binding mode between the DNA and Ni (II) phthalocyanine compound. As a result, the compound indicates intense binding activities with the DNA. These results show that nickle (II) phthalocyanine compound could be a candidate compound in cancer treatment due to its DNA binding activities.

ACKNOWLEDGMENTS

REFERENCES

1. Leznoff CC, Lever ABP. Phthalocyanine: Properties and Applications. VCH publishers, New York, pp. 1–4, 1996.

2. Agirtas MS, Karatas C, Gümüş S. Synthesis, Aggregation Behavior, and Electronic properties of some metallophthalocyanines with 2−Isopropyl−5−methylphenoxy substituents. Z Anorg Allg Chem 641(7) (2015) 1334−1339.

3. Agirtas MS, Karatas C, Özdemir S. Synthesis of some metallophthalocyanines with dimethyl 5−(phenoxy)−isophthalate substituents and evaluation of their antioxidant−antibacterial activities. Spectrochimica Acta Part A: Molecular and Biomolecular Spectroscopy 135 (2015) 20−24.

4. McKeown NB. Phthalocyanines Materials: Synthesis, Structure and Functions. Cambridge, MA: Cambridge University Press, 1998.

5. Agirtas MS, Altındal A, Salih B, Saydam S, Bekaroglu Ö. Synthesis, characterization, and electrochemical and electrical properties of novel mono and ball−type metallophthalocyanines with four 9,9−bis(4−hydroxyphenyl) fluorine. Daltons Trans 40 (2011) 3315− 24.

6. Peng Y, Zhang H, Wu H, Huang B, Gan L, Chen Z. The sysnthesis and photophysical properties of zinc (II) phthalocyanine bearing poly (aryl benzyl ether) dendritic substituents. Dyes and Pigments 87 (2010) 10−16.

7. Jori G. photosensitized processes in vivo: proposed phototherapeutic applications. J Photoch Photobio 52 (1990) 439–443.

8. Eshkourfu R, Cobeljic B, Vujcic M, Turel I, Pevec A, Sepcic K, Zec M, Radulovic S, Srdic–Radic T, Mitic D, Andjelkovic K, Sladic D. Synthesis, characterization, cytotoxic activity and DNA binding properties of the novel dinuclear cobalt (II) complex with the condensation product of 2–acetylpyrine and malonic acid dihydrazide. Inorg Biochem 105 (2011) 1196–1203.

9. Uslan C, Sesalan BS. Synthesis of novel DNA–interacting phthalocyanines. Dyes and Pigments 94 (2012) 127–135.

10. Janjua NK, Shaheen A, Yaqup A, Perveen F, Sabahat S, Mumtaz M, Yacob C, Ba LA, Mohammed HA. Flavonoid–DNA binding studies and thermodynamic parameters. Spectrochim Acta A 79 (2011) 1600–1604.

11. Palchaudhuri R, Hergenrother PJ. DNA as a target for anticancer compounds: methods to determine the mode of binding and the mechanism of action. Curr Opin Biotechnol 18 (2007) 497–503.

12. Wolfe A, Shimer GH, Meehan T. Polycyclic aromatic hydrocarbons physically intercalate into duplex regions of denatured DNA. Biochemistry 26 (1987) 6392–6396.

13. Lopez Zeballos NC, Gauna GA, Garcia Vior MC, Awruch J, Dicelio LE. Interaction of cationic phthalocyanines with DNA. Importance of the substituents. J Photochem Photobiol B Biology 136 (2014) 29–33.

14. Özçesmeci M, Ecevit ÖB, Sürgün S. Humuryudan S. Tetracationic fluorinated zinc (ii) phthalocyanine: Synthesis, characterization and DNA–binding properties E. Hamuryudan, Dyes and Pigments 96 (2013) 52–58.

15. Apilux A, Tabata MChailapakul O. Electrochemical bihaviors of native and thermal denatured fish DNA in the presence of cytosine derivatives and porphyrin by cyclic voltammetry using boron–drobed diamond electrode. Bioelectrochemistry 70 (2007) 435–439.

16. Demirezen N, Tarınc D, Polat D, Cesme M, Golcu A, Tumer M. Synthesis of trimethoprim metal complexes: Spectral, electrochmical, thermal, DNA–binding and surface morp hology studies. Spectrochimica Acta Part A 94 (2012) 243–255.

17. Reddy PR, Shilpa A, Raju N, Raghavaiah P. Synthesis, structure, DNA binding and cleavage properties of ternaryamino acid Schiff base–phen/bipy C(II) complexes. J Inorg Bioochem 105 (2011) 1603–1612.

18. Liu X–W, Shen Y–M, Li Z–X, Zhong X, Chen Y–D, Zhang S–B. Study on DNA binding behavior and light switch effect of new coumarin–derived Ru (II) complexes. Spectrochimica Acta Part: Molecular and Biomolecular Specrtoscopy 149 (2015) 150–156.

19. Ozluer C, Satana Kara HE. In vitro DNA binding studies of anticancer drug idarubicin using spectroscopic techniques. J Photochem Photobiol B 138 (2014) 36-42.

20. Pradeepa SM, Bhojya Naik HS, Vinay Kumar B, Indira Priyadarsini K, Barik A, Prabhakara MC. DNA binding, photoactivated DNA cleavage and cytotoxic activity of Cu(II) and Co(II) based Schiff–base azo ptotosensitizers. Spectrochim Acta A 141 (2015) 141:34-42.

21. Özel A, Barut B, Demirbaş Ü, Biyiklioglu Z. Invetigation of DNA binding, DNA photocleavage, topoisomerase I inhibition and antioxidant activities of water soluble titanium (IV) phthalocyanine compounds. J Photoch and Photobiol B Biology 157 (2016) 32–38.

22. Mahadevan S, Palaniandavar M. Spectroscopic and voltametric studies on copper complexes of 2,9–dimethyl–1,10–phenanthrolines bound to calf thymus DNA. J Inorg Chem 37 (1998) 693–706.

23. Sirajuddin M, Ali S, Badshah A. Drug–DNA interactions and their study by UV–Visible, fluorescence spectroscopies and cyclic voltametry. J Photochem Photobiol B Biology 124 (2013) 1–19.

24. Song YM, Yang PJ, Yang ML, Kang JW, Qin SQ, Lu BQ. Spectroscopic and voltammetric studies of the cobalt (II) complexe of morin bound to calf thymus DNA. Transition Met Chem 28 (2003) 712– 721.

25. Zhang SS, Niu SY, Qu B, Jie GB, Xu H, Ding CF. Studies on the interaction mechanism between hexakis(imidazole) manganese (II) terephthalate and DNA and preparation of DNA electrochemical sensor. J Inorg Biochem 99 (2005) 2340–2347.

26. Cater MT, Rodriguez M, Bard AJ. Voltammetric studies of the interaction of metal chelated with DNA. 2. Tris–chelated complexes of cobalt (III) and iron (II) with 1,10–phenanthroline and 2, 20– bipryridine. J Am Chem Soc 111 (1989) 8901–8911.

27. Pravin P, Utthra PP, Kumaravel G, Raman N. Effective DNA binding and cleavage tendencies of malonic acid coupled transition metal complexes. J Mol Struc 1123 (2016) 162–70.

28. Keleş T, Barut B, Biyiklioglu Z, Özel A. A comparative study on DNA/BSA binding, DNA pA comparative study on DNA/BSA binding, DNA photocleavage and antioxidant activities of water soluble peripherally and non–peripherally tetra–3–pyridin–3–ylpropoxy–substituted Mn(II), Cu (II). Dyes and Pigments 2017; doi: 10.1016/j.dyepig. 2016.12.045.

29. Azza A S, Mohamed MS. DNA binding, spectrocopic and antimicrobial studies of palladium (II) complexes containin 2,2o–bipyridin and 1–phenypiperazine. Spectrochimica Acta Part A Molecular and Biomolecular Spectroscopy 96 (2012) 586–593.

30. Hassani L, Hakimian F, Safaei E, Fazzeli Z. Antibacterial effect of cationic porphyrazines and anionic phthalocyanine and their interaction with plasmid DNA. J Mol Struc 1052 (2013) 221–227.

31. Al–Mogren MM, Alaghaz MA, Ebrahem EA. Synthesis, spectroscopic, molecular orbital calculation, cytotoxic, molecular docking of DNA binding and DNA cleavage studies of of transition metal complexes with N–benzylidene-N´–salicylidene–1,1–diaminopropane. Spectrochimica Acta Part A Molecular and Biomolecular Spectroscopy 114 (2013) 695–707.

A Monitoring and Control System Integrated with Smart Phones for The Efficient Use of Underground Water Resources in Agricultural Product Growing

Mehmet Fatih IŞIK[1] **Mustafa Reşit HABOĞLU**[2] **Ercan IŞIK**[3]

¹ Hitit University, Department of Electrical and Electronics Engineering, Çorum, TURKEY
² Hitit University, Department of Mechanical Engineering, Çorum, TURKEY
³ Bitlis Eren University, Department of Civil Engineering, Bitlis, TURKEY

ABSTRACT

Monitoring and control system is very important for crop development process in agriculture zones. A structure which is carried out based on the type of the product with the knowledge of temperature and humidity values of the agricultural land can contribute to the efficient use of underground water resources. Additionally, it can also contribute to the establishment of the administration of the land besides the economical contributions to the farmer. In this study, the values obtained by heat and humidity sensors which are placed in different locations of agricultural field are transmitted to a database by using a central operation unit. The water requirement based on the product is determined according to that database. Those values are transferred to the smart phones by using a Wi-Fi connection. A real time monitoring system is established on the smart phone. The energy supply of the system is obtained by solar cells. The design offers several advantages such as saving of the water, time and energy with the efficient use of underground water resources. Thus, by using clean energy, the design constitutes an environmental friendly system.

Keywords:
Agriculture zone, Smart phone, Underground water, Sensor networks

INTRODUCTION

The insufficiency of the water resources in the world has led to the necessity for the watering to be more sensitive. Especially for the fields that does not have any watering system, the watering is supplied with underground water resources by using wells. The true use of underground water resources is important for the economical reasons as well as for the ecological balance. That situation has made interdisciplinary work necessary for both commercial and academically studies. When the situation is considered in Turkey, the technological developments should contribute more in ecological system and the administration of agricultural lands. Many new technological procedures are being used for the monitoring and control of agricultural lands [1-4]. Tablets and smart phones are becoming more widespread as the technology develops [5-15].

The main aim of this study is to develop an overall monitoring and control system for the efficient use of underground water resources in agricultural lands. An information platform is established for the agricultural land by temperature and humidity sensors. The values obtained by the sensors are transferred to a central database. That database is also present on a web based server as it can be reached by a Wi-Fi structure. The only arrangement that the farmer should do is choosing the plant for that season. The system performs all the operations according to the chosen plant automatically. Those operations contain initial, crop development, mid season and late season periods. This study also comes forward with the usage of clean energy. The energy costs are reduced by using renewable energy with the help of solar panels placed on the agricultural land.

The determination of the water requirement ac-

cording to the product development periods can contribute to the true use of underground water resources. Especially in drip irrigation systems, the plant is subjected to a small amount of water continuously. In this study, smart use of water according to the production stage is used instead of that system. The United Nations Food and Agriculture Organization (FAO) recommends Penman Monteith method developed to determine crop water requirement. It is aimed to calculate the healthy evapotranspiration with the crop coefficient (kc) determined by the specific data of the irrigation area. The reference evapotranspiration (ET0) has been used and required climate data have been obtained from internet site of Turkish State Meteorological Service (www.mgm.gov.tr) in order to account using the FAO Penman Monteith method [16].

$$ET_O = \frac{0,408*\Delta*(R_n - G)+\gamma*(\frac{900}{T+273})*u_2*(e_s - e_a)}{\Delta+\gamma*(1+0,34*u_2)} \quad (1)$$

Here,

ET_0: Reference evapotranspiration (mm day^{-1}),
R_n: Net radiation (MJ m^{-2} day^{-1}),
G: Soil temperature flux density (MJ m^{-2} day^{-1}),
T: The average daily air temperature (°C),
U_2: 2 m height wind speed (m s^{-1}),
e_s: Saturated vapor pressure (kPa),
e_a: Actual steam pressure (kPa),
Δ: The slope of the vapor pressure curve (kPa /°C^{-1}),
γ: Psychometric constant (kPa).

EXPERIMENTAL STUDY

The Agriculture Zone situated in the Çorum/Mecitözü in the Middle Black Sea region of Turkey has the latitude 41°51'N and the longitude 35°29'E. The altitude is 750 m above the sea level. Climate data obtained from the me-

teorological station that belong to Çorum/Mecitözü are shown in Table 1.

The obtained climate data and the values of crop water requirements depending on seasonal development are shown in Table 2. According to the table, the total water demand in the process of growing the product has been identified as 362,1 mm/dec.

The experimental study is carried out in a tomato land with 200 m² in Mecitözü. The plan of the control and monitoring system along with the home page screenshot of smart phone are given in Figure 1. Ground water that is transfer-
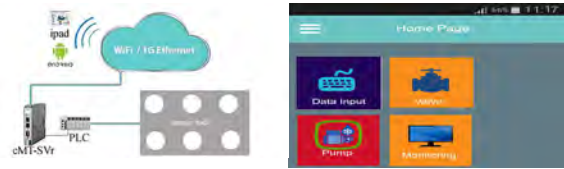
Figure 1. Functional diagram of the monitoring and control and home page screenshot

red from the well to the water tank with 500 Lt by the booster has been connected to irrigation laterals via a filter. The required energy for the agriculture zone control and monitoring system are obtained by solar panels.

A Programmable Logic Controller (PLC) is used as the hardware in the study. The output of the PLC is a pump while the inputs are sensors. An IOS/Android server is connected to the PLC and the mobile devices are communicating with the server via a Wi-Fi router. The server provides direct communication between the mobile devices and the addresses on the PLC. At this point, monitoring and control of the system with the IOS/Android devices is possible with a developed software. The program called Easy Builder Pro

Table 1. Çorum/Mecitözü Climate/ETo data

Month	Avg. Temp	Humidity	Wind	Sun	Rad	ETo
	°C	%	km/day	hours	MJ/m²/day	mm/day
January	0.2	77	120	2.5	5.7	0.61
February	1.5	75	155	3.6	8.5	0.89
March	5.3	68	164	5	12.6	1.57
April	10.9	64	172	6.1	16.7	2.58
May	15.5	60	172	7.2	19.9	3.63
June	18.9	53	172	8.7	22.7	4.62
July	21.6	45	216	9.9	23.9	5.64
August	21.4	47	207	9.9	22.3	5.22
September	17.4	57	172	8.3	17.4	3.53
October	12.4	65	130	5.6	11.2	1.95
November	7	70	147	3.6	7	1.16
December	2.2	78	130	2.1	4.9	0.66
Average	**11.2**	**63**	**163**	**6**	**14.4**	**2.67**

Table 2. Crop Water Requirements

Month	Stage	Kc [coeff]	ETc [mm/dec]	Eff rain [mm/dec]	Irr. Req. [mm/dec]
April	Initial	0.57	7.7	10.8	0
April	Initial	0.57	14.7	19.7	0
April	Development	0.57	16.8	19	0
May	Development	0.64	21	18.4	2.6
May	Development	0.74	27	18.2	8.9
May	Mid	0.85	37.2	16.1	21
June	Mid	0.89	38.1	14.1	23.9
June	Mid	0.89	41	12.4	28.6
June	Mid	0.89	44	9.5	34.5
July	Mid	0.89	47.6	5.7	41.9
July	Mid	0.89	50.9	2.5	48.4
July	Mid	0.89	54.3	3.2	51.2
August	Late	0.89	48.1	4	44
August	Late	0.77	41.1	4.2	36.9
August	Late	0.6	25.6	4.3	20.3
			514.9	162.2	362.1
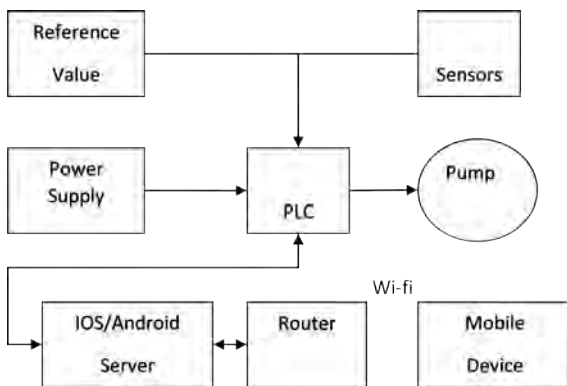
Figure 2. The block diagram of the designed set

that is developed by Weintek Corporation is used as that software. The program starts with introducing the PLC to
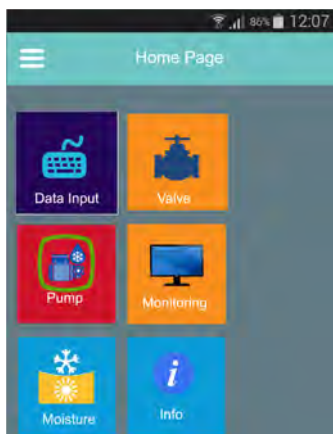
Figure 3. The mobile application screen

the software. After that, the addresses to monitor and control the desired parameters should be identified. In this study, the data collected from the sensors is transmitted to the

Figure 4. The moisture screen on mobile device

PLC through the web. Each parameter has a valid address that can be accessed from the Easy Builder Pro which is installed on the mobile device. The closed loop block diagram of the designed system is presented in Fig. 2.

The mobile interface initialization screen is presented in Fig. 3. The parameters for different crops can be specified through the "Data Input" option. Thus, an irrigation chart for different crops can be obtained. The manual control of the valves can be obtained via the "Valve" option while the "Pump" option controls the on/off actions for the pump. The "Monitoring" option shows the situations for the pump and the valves. The data collected from the sensors can be viewed with the "Moisture" option. Finally, the "Info" option

Figure 5. The moisture values obtained from Sensor 2.

presents information about the software.

The Fig. 4 shows the moisture screen that collects data from DS200 moisture sensors that are located in the different points of the field. There are 9 moisture sensors used in this study. Fig. 5 shows an example data collected from Sensor 2. The moisture values collected from sensors are displayed as percentages. It is possible for the user to monitor the moisture values in a desired time interval.

Fig. 6 shows the example execution field that the study is applied.

Figure 6. An example of the application

RESULTS AND DISCUSSION

Planting date from April to harvest; average monthly temperature results obtained from sensors in agriculture zone have been given in Fig. 7. As can be seen in Fig. 7, temperature rate is almost constant during the all stages. The temperature values of the land are measured in initial, development, mid-season and late season stages. That period covers a total time of 5 months. The highest temperature is about 18°C which appears to occur in the mid-season. On the other hand, the lowest temperature is about 13°C that is around the initial stage. The graph contains data which are the average of the daily measured values..
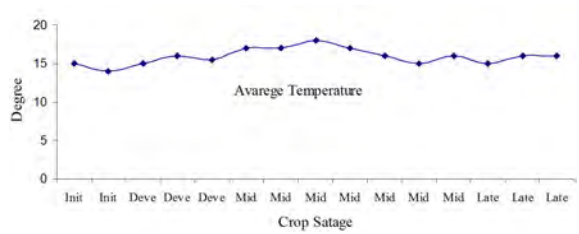
Figure 7. Monthly average temperature

Figure 8 shows the processing screen for the moisture values collected from the sensors. The data presented in the graph is collected in the mid-season and it shows the percentage of the moisture. Moisture rate decreases especially during the effects of the sun. When this situation is compared with the climatic data, it is seen that these results are close to the average values.
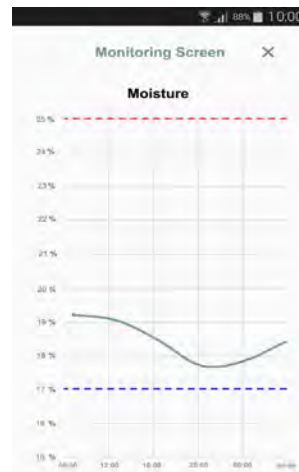
Figure 8. The average moisture values occurring in the sensors during day

The water consumption values for the growth stages are presented in Figure 9. The figure contains the irrigation values for both the developed system and conventional drip irrigation systems. Additionally, the water requirements for the growth stages are also presented in the figure. It can be seen that the irrigation values for the developed system fits very well with the water requirements curve. As a result, the developed system contributes %38 more underground water savings when compared with the conventional drip irrigation system.
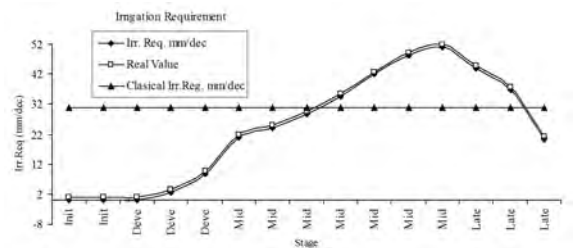
Figure 9. Comparison amount of water depending on the stage of plant growth and used amount of water

CONCLUSION

This study shows that ground water irrigation system with moisture and temperature sensors are extremely advantageous for growing crops in agricultural systems. A very important advantage is obtained by adjusting the amount of ground water needed in the plant growth stages and by consuming the water depending on the soil moisture and temperature with classic drip irrigation systems. Amount savings has been achieved in energy costs by using solar energy. The system can be operated integrating with smart phones. Hence, the whole system can be controlled and monitored by these devices which is an indispensable instrument of modern technology. Besides the efficient use of underground water resources, this study also constitutes an effective structure for the administration of the agricultural lands.

The designed system constitutes the monitoring and control of the amount of water inside the land which is based on the stage of the plant growth. A future work may focus on the optimization techniques to provide more precise irrigation for the plant growth. The combination of the data gathered from past rainfall values and moisture levels inside the land might be the main contributions for the optimization. The agricultural systems will benefit from that system as more precise information is gathered for the facts such as the need of water for the plant growth and the exact time of growth stages.

REFERENCES

1. Weng Q. Advances in environmental remote sensing: sensors, algorithms, and applications (remote sensing applications series). CRC Press Taylor & Francis Group; (2011).

2. Committee on the earth system science for decisions about human welfare: contributions of remote sensing, contributions of land remote sensing for decisions about food security and human health, workshop report. Washington: National Academies Press, (2007).

3. Pierce FJ, Clay D. GIS applications in agriculture. CRC PressTaylor & Francis Group; (2007).

4. El-Kader SMA, Basma M. Mohammad El-Basioni. Precision farming solution in Egypt using the wireless sensor network technology. Egyptian Informatics Journal 14(3) (2013) 221–233.

5. Broeders J, Croux D, Peeters M, Beyens T, Duchateau S, Cleij TJ, Wagner P, Thoelen R, De Ceuninck W. Mobile application for impedance-based biomimetic sensor readout. IEEE Sensors Journal 13(7) (2013) 2659–2665.

6. Ishigaki Y, Matsumoto Y, Ichimaya R, Tanaka K. Development of mobile radiation monitoring system utilizing smartphone and its field tests in Fukushima. IEEE Sensors Journal 13(10) (2013) 3520–3526.

7. Lee J, Reyes BA, McManus DD, Maitas O, Chon KH. Atrial fibrillation detection using an iPhone 4S. IEEE Transactions on Biomedical.Engineering 60(1) (2013) 203–206.

8. Koukomidis E, Martonosi M, Peh LS. Leveraging smartphone cameras for collaborative road advisories. IEEE Transactions on Mobile Computing 11(5) (2012) 707–723.

9. Qin C, Bao X, Choudhury RR, Nelakuditi S. TagSense: Leveraging smartphones for automatic image tagging. IEEE Transactions on Mobile Computing 13(1) (2014) 61–74.

10. Car NJ, Christen EW, Hornbuckle JW, Moore GA. Using a mobile phone short messaging service (SMS) for irrigation scheduling in Australia-Farmers' participation and utility evaluation. Computers and Electronics in Agriculture 84 (2012) 132–143.

11. Sallabi F, Fadel M, Hussein A, Jaffar A, El Khatib H. Design and implementation of an electronic mobile poultry production documentation system. Computers and Electronics in Agriculture 76(1) (2011) 28–37.

12. Arroqui M, Mateos C, Machado C, Zunino A. RESTful Web services improve the efficiency of data transfer of a whole-farm Simulator accessed by Android smartphones. Computers and Electronics in Agriculture 87 (2012) 14–18.

15. Montoya FG, Gomez J, Cama A, Zapata-Sierra A, Martinez F, De La Cruz JL, Manzano-Agugliaro F. A monitoring system for intensive agriculture based on mesh networks and the Android system. Computers and Electronics in Agriculture 99 (2013) 14–20.

16. M. Sait TAHMISCIOGLU "T.C. Orman ve su isleri bakanlıgı devlet su isleri genel müdürlügü, Türkiye' de bitki su tüketimi çalısmaları", Etüt, Planlama ve Tahsisler Dairesi Baskanlıgı, Mart, (2015).

Biosorption Behaviour of an Arid Land Plant, *Euphorbia rigida*, Towards to Heavy Metals: Equilibrium, Kinetic and Thermodynamic Studies

Murat Kılıç[1] **Gamzenur Özsin**[2] **Esin Apaydın-Varol**[1], **Ayşe Eren Pütün**[1]
[1] Anadolu University, Department of Chemical Engineering, Eskişehir, TURKEY
[2] Bilecik Şeyh Edebali University, Department of Chemical and Process Engineering, Bilecik, TURKEY

ABSTRACT

The potential of an arid-land plant, *Euphorbia rigida* (*E. rigida*), for the removal of heavy metals [Pb(II), Zn(II), Cu(II), Cd(II), Ni(II)] from aqueous solutions was studied in the current work. Batch sorption experiments were conducted to investigate the effects of pH, particle size, initial metal ion concentration, contact time and temperature. Besides, biosorption data was analysed by different isotherm and kinetic models. Equilibrium studies showed that the biosorption closely follows the Langmuir and Freundlich isotherms. From the kinetic point of view, pseudo-second order model gave the best fitting with the experimental results. The evaluated thermodynamic parameters showed that biosorption onto *E. rigida* was a feasible, spontaneous and endothermic process. The affinities of metal ions onto *E. rigida* decreased as Pb(II) > Zn(II) > Cd(II) > Cu(II) > Ni(II) in single metal biosorption. Besides, binary and ternary metal sorption studies were conducted to investigate the co-ion effect. Experimental results showed that *E. rigida* can be used as an alternative and effective low cost biosorbent for the removal of heavy metals from aqueous solutions.

Keywords:

Euphorbia rigida; Single-multi heavy metal biosorption; Equilibrium; Kinetics; Thermodynamics

INTRODUCTION

High release of heavy metals from industries like metal processing, refining, paint, battery industry and mining causes serious wastewater contamination because of the non-degradable nature of metals. Released metal ions become poisonous for both plants and living organisms after certain concentrations since they tend to pile up in living organisms and cause various disturbances and disorders [1-4]. Hence, various physical and/or chemical treatment techniques have been applied for many years, such as chemical reduction, precipitation, solvent extraction, coagulation, flocculation and filtration, membrane processes [5-7]. However, feasible applications of the mentioned techniques are limited due to high operational and initial capital costs, low efficiency and production of undesirable sludge. Many of the mentioned techniques have substantial penalties, such as demand for high-priced equipment, high reagent consumption, high energy requirement, inadequate metal removal, and generation of toxic sludge. On the other hand, adsorption systems are rapidly gaining prominence in water treatment processes because of advantages such as easy design, control and operation [8]. The versatility and simplicity of adsorption directed researchers to search alternative sorbents to the time-honored sorbents. Therefore, the biosorption study of metal ions on natural adsorbents which are abundant in nature and require little processing is important for finding low-cost adsorbents [9-11]. Biosorption involves metal binding by ionic and covalent bonds to the surface matrix of the biomass [12]. It is known as an alternative technique to treat dilute heavy metal wastewaters because of availability of unlimited bio sources, high efficiency and surface porosity of biomass [13]. To this end, agricultural wastes and non-edible plants are considered as a viable option for utilization in biosorption processes.

In the literature, different biomass samples like nutshells [14], sawdust [15], algae [16] and their modified forms [17] were reported as alternative biosorbents. However, attention should be should be drawn on naturally

growing land plants considering both their abundancies and biosorption abilities. Among various types of biomass species, terpene hydrocarbons could be an effective candidate for biosorption processes. A well-known terpenoid biomass is the Euphorbiaceae family and *Euphorbia rigida*, a member of Euphorbiaceae, grows on the arid lands of Middle Anatolia in abundant quantities and without requiring special labour. About 2000 species of *E. rigida* is known all along the world and it is reported that 80 species of *Euphorbia* are found in Turkey. This biomass drew the attention of several researchers interested in converting it to petroleum substitute oil by pyrolysis [18]. Also, in another study, highly porous activated carbons were produced from *E. rigida* by chemical activation [19]. But direct utilization of *E. rigida* without applying any thermal treatment process for the removal of hazardous species has not been sufficiently studied. It is believed that usage of *E. rigida* as a biosorbent would lead to a new evaluation route for the other non-edible biomass species. In biosorption processes, it is also well known that interpretation and representation of multi-metallic systems is more complex than that of monometallic systems because of competition phenomena and hence there are limited published works on it. Therefore, the scope of this study was to determine the sorption characteristics of *E. rigida* for the removal of Pb(II), Zn(II), Cu(II), Cd(II) and Ni(II). Batch biosorption experiments were focused on to investigate the effects of solution pH, particle size, initial metal ion concentration, contact time and temperature. Equilibrium and kinetic studies together with the thermodynamic analysis were made with the obtained data. In addition, experiments were conducted in multi-metal solutions to investigate the co-ion effect.

METHODS

Biomass Preparation and Characterization

Raw *E. rigida* (leaves and stalks) samples were obtained from South-western Anatolia. Before biosorption experiments, *E. rigida* was washed to remove contaminants and dried at room temperature. Proximate, ultimate and component analysis of *E. rigida* were performed to determine characteristics of the biomass and all the results were summarized in Table 1.

In order to characterize surface chemistry of *E. rigida* modified Boehm titration was performed and surface acidic and basic groups were quantified. For this purpose, 0.5 g of biomass samples were placed to a series of flasks which include 50 mL of 0.05 N NaHCO$_3$, Na$_2$CO$_3$, NaOH and HCl. The flasks were shaken for 24 h and then filtered and titrated with 0.05 N NaOH or HCl depending on the nature of surface groups. By observing the end points in the presence of phenolphthalein and methyl red indicators, amount of the surface groups was determined quantitatively.

The pH point of zero charge (pHpzc) of *E. Rigida* was also determined by pH drift method. For this purpose, 0.15 g of biomass sample was added 50 mL solution of 0.01 M NaCl whose initial pH had been measured and adjusted by 0.01 M NaOH or HCl. The pH values of the solutions were measured after 48 h. The pHpzc of biosorbent is noted as the point where pH$_{initial}$ equals to pH$_{final}$.

The surface microstructure of E. rigida was also characterized using scanning electron microscope combined with Energy Dispersive X-ray Spectroscopy , SEM-EDX (Zeiss Supra 50VP).

Biosorption Experiments

The salts used were Pb(NO$_3$)$_2$, N$_2$O$_6$Zn.6H$_2$O, Cu(NO$_3$)$_2$.3H$_2$O, Cd(NO$_3$)$_2$.4H$_2$O and Ni(NO$_3$)$_2$.6H$_2$O, for Pb(II), Zn(II), Cu(II), Cd(II), Ni(II), respectively. Stock solutions of 1000 mg/L were prepared by analytical grade salts in double deionized water which has a conductivity of 18.2 MΩ/cm. Then, stock solutions were diluted to acquire desired concentrations. The initial pH values were regulated to the required value with 0.1 mol/L and/or 0.01 mol/L of NaOH and HCl solution. Batch biosorption experiments were performed by mixing metal solutions with *E. rigida* in a temperature programmed shaker and by taking samples at different time intervals. Each experiment is performed twice and average values were considered. The effects of biosorption parameters such as, pH (3-9), particle size (0.112-0.850 mm), biosorbent dosage (1-10 g/L), initial metal ion concentration (10-50 mg/L), contact time (up to 24 h) and temperature (20-40 °C) were investigated in a batch mode. After sorption process, biomass separated from the samples by filtering and the filtrate was analysed by atomic adsorption spectrometer (Varian Spectra A240 FS)

The amount of metal biosorbed per unit mass of the biosorbent at equilibrium (q_e) and at each time interval (q_t) were calculated by the following equations,

$$q_e = \frac{(C_i - C_e)\, V}{w} \tag{1}$$

$$q_t = \frac{(C_i - C_t)\, V}{w} \tag{2}$$

where C_i is the initial and C_e is the equilibrium concentration of the metal ion (mg/L). In the equations, C_t is the concentration of the metal ion at any time (mg/L), V is the volume of aqueous solution (L), and w is the mass of biosorbent (g).

In the last stage of the study, binary and ternary biosorption experiments were conducted to conclude whether *E. rigida* is applicable for the treatment of solutions including the combination of heavy metals.

Theoretical Approach

Biosorption Isotherms

For convenient design and fundamental knowledge of the process, biosorption isotherm, the specific relationship between sorbate and sorbents in equilibrium, is necessary. In order to gain information about the mutual effects of sorbent and sorbate, different isotherm models should be applied to experimental data. In this study, Langmuir, Freundlich, and Dubinin-Radushkevich (D-R) models were used to investigate the biosorption equilibrium between the metal ions and the biosorbent.

Langmuir model assumes that sorption occurs by distribution of sorbate molecules in a single layer throughout the sorbent surface and dynamic equilibrium exists between sorbed and non-adsorbed free molecules [20-22]. The linearized form of the Langmuir is given as follows:

$$\frac{C_e}{q_e} = \frac{1}{q_m K_L} + \frac{C_e}{q_m} \tag{3}$$

where q_m is the monolayer adsorption capacity of the activated carbon (mg/g), and K_L is the constant (L/mg).

Freundlich model accepts multilayer adsorbate uptake on the sorbent surface and heterogeneous sorbate surface with active sites [23]. The linearized Freundlich equation is given by;

$$\ln qe = \ln K_F + \frac{1}{n} \ln C_e \tag{4}$$

where K_F ((mg/g)(L/mg)1/n) is a constant related with the adsorption capacity and n is an empirical parameter indicating the adsorption intensity.

Dubinin-Radushkevich (D-R) model designates the adsorption on uniform pores and a variable adsorption potential throughout a heterogeneous surface [24]. The linear D-R isotherm equation is as follows:

$$\ln q_e = \ln q_m - \beta \varepsilon^2 \tag{5}$$

where β is a constant related to the adsorption energy (mol²/kJ²), q_m is the theoretical saturation capacity, and ε is the Polanyi potential.

The last isotherm model used in the study, Temkin [25] considers the effects of indirect sorbent/sorbate interactions and assumes non-uniformly distributed binding energies of sorbate molecules. The linear form of Temkin isotherm equation is expressed as:

$$q_e = B \ln K_T + B \ln C_e \tag{6}$$

Biosorption Kinetics

The biosorption processes can be controlled by different mechanisms and various kinetic models (pseudo-first order, pseudo-second order, intraparticle diffusion and Elovich) were used to look into the mechanism and influential parameters of the sorption.

The pseudo-first order model expresses the rate equation by assuming the rate of change of solute uptake with time is related with the difference in saturation concentration and instantaneous concentration [26]. The pseudo-first order equation is formulized as follows:

$$\frac{dq_t}{dt} = k_1(q_e - q_t) \tag{7}$$

where k_1 is the rate constant which is belonging to pseudo-first order model (1/min). Integration of this equation is turned out a linearized form as:

$$\log(q_e - q_t) = \log(q_e) - \frac{k_1 t}{2.303} \tag{8}$$

Apart from the first order equation, the rate of change of solute uptake with time varies with the square of the difference in saturation concentration and the quantity of solid uptake in pseudo-second order equation as follows:

$$\frac{dq_t}{dt} = k_2(q_e - q_t)^2 \tag{9}$$

where k_2 is the rate constant of pseudo-second order model (g/mg.min) [27]. Integration of this equation also resulted in a linearized form as:

$$\frac{t}{q_t} = \frac{1}{k_2 q_e^2} + \frac{1}{q_e} t \tag{10}$$

Although pseudo-first order together with pseudo-second order are convenient to describe sorption kinetics, they don't take into account the diffusion effect. At this point, intraparticle diffusion model [28] is beneficial for in-depth investigation of transportation process of sorbate molecules. The intraparticle diffusion equation expresses variation of solute uptake proportional with $t^{1/2}$ and is written by the following equation:

$$q_t = k_p t^{1/2} + C \tag{11}$$

where k_p is the intraparticle diffusion rate constant (mg/g min$^{1/2}$) and C is the intercept of intraparticle model plot which gives an opinion about the thickness of the boundary layer. Accordingly, if intraparticle diffusion is included in the sorption, the model plot should be linear. Either, intraparticle diffusion is the rate-controlling step in the case of model lines go across the origin then. Otherwise, some other mechanisms are accepted to be present which effects the boundary layer [29, 30].

On the other hand, Elovich kinetic model [31] may be suitable when there is a chemical interaction between sorbate ions and surface sites. The linear Elovich equation can be represented by:

$$q_t = \frac{1}{\beta} \ln(\alpha \beta) + \frac{1}{\beta} \ln t \tag{12}$$

Table 1. Characteristics of *E. rigida*

Proximate analysis (%)		Ultimate analysis (%)		Component analysis (%)	
Moisture	3.00	C	49.56	Extractive	12.55
Ash	6.40	H	5.16	Lignin	37.92
Volatiles	76.80	N	1.20	Hemicellulose	29.50
Fixed C*	13.80	O+inorganics*	44.08	Cellulose inorganics *	19.17

*Calculated as difference
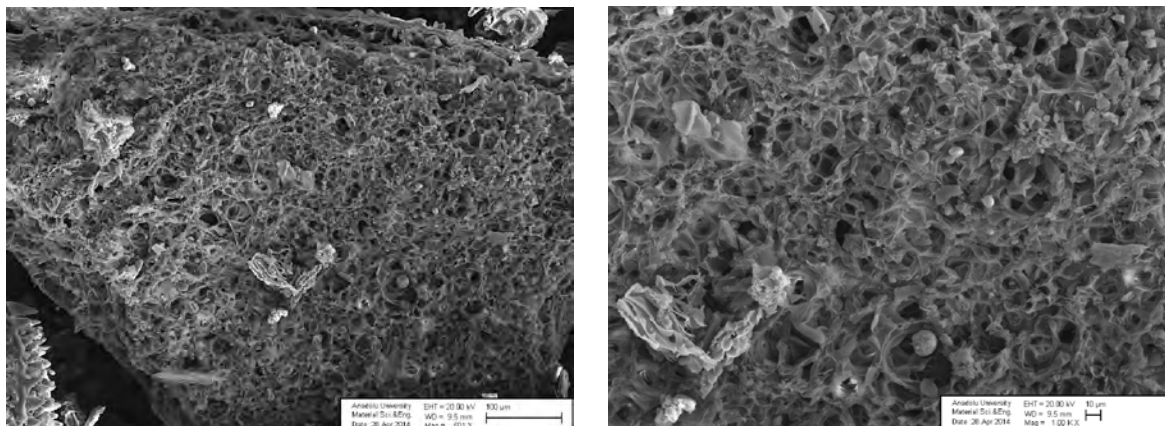
Figure 1. SEM micrographs of raw *E. rigida*

Biosorption Thermodynamics

For detection of the effects of temperature, spontaneity and feasibility of sorption process, thermodynamic parameters (Change in Gibbs free energy, enthalpy and entropy) should be interpreted.

The Gibbs free energy change (ΔG°) of biosorption process can be determined from the given equation:

$$\Delta G^o = -RT \ln K_L \qquad (13)$$

where R is the gas constant (8.314 J/mol.K), K_L is equilibrium Langmuir constant and T is the temperature (K). Relationship between ΔG°, enthalpy change (ΔH°) and entropy change (ΔS°) can be demonstrated by:

$$\Delta G^o = \Delta H^o - T\Delta S^o \qquad (14)$$

and manipulation of Eq.13 is resulted in a linear equation for calculating thermodynamic parameters as:

$$\ln K_L = -\frac{\Delta G^o}{RT} = -\frac{\Delta H^o}{RT} + \frac{\Delta S^o}{R} \qquad (15)$$

RESULTS AND DISCUSSION

Characteristics of *E. rigida*

Fig 1 presents two electron micrograph examples of the *E. rigida* with a magnification of 500x and 1000x. According to secondary electron images, surface of raw *E. rigida* seems heterogeneous which includes some interconnected pores and channels. This topographical feature of E. rigida shows that it can be useful for sorption of metal ions. According to EDX analysis C and O are the main atomic constituents with minor amounts of Si, Mg, Ca. Ultimate analysis results given in Table 1 also supports that the main constituent of *E. rigida* is C which is 50 wt.% approximately.

Surface chemistry of E. rigida (Table 2) was studied by determination of pHpzc and surface functional groups using Boehm titration. According to the results, quantity of acidic surface groups are more than basic surface groups. Approximately 90 % of acidic surface groups are determined as phenolics.

Biosorption of single-metal solutions

Effect of pH

Since pH affects solubility of metal ions metal binding sites by dissociation of active functional groups and surface charges, it is one of the important factors that should be considered throughout the biosorption process. The effect of pH on heavy metal sorption was determined by performing the experiments in a pH range of 3-9 with a constant particle size range as 0.112-0.224 mm. The results are given in Fig. 2 and pHpzc and amount of surface functionalities were summarized in Table 2. Accordingly, pHpzc, value of *E. Rigida* can be deduced close to 5.0 because of acidic surface groups. It is known that, when pH is less than pHpzc the surface of the biosorbent becomes positively charged, and metal sorption is hindered, because of electrostatic repulsion between ions and surface functional groups. On the contrary, in the case of higher pH values than pHpzc, the quantity of negative charges increases and hence metal sorption is frequently favou-

Table 2. Surface chemistry of *E. rigida*

PH_{PZC}	Carboxylic (meq/g)	Lactonic (meq/g)	Phenolic (meq/g)	Acidic (meq/g)	Basic (meq/g)
4.82	0.2662	0.0888	3.4510	3.8060	0.1443

red. The further increase in pH also causes an increase of the dissociation degree of functional groups from biosorbent surface and electrostatic interactions increases as a consequence. The amounts of Zn (II) and Cd(II) biosorbed onto *E. rigida* was found to increase with an increase in pH from 3 to 7. But further increasing pH caused to decreases in biosorption capacities of these two ions. According to this, optimum pH value for Zn (II) and Cd(II) ions was determined as 7. On the other hand, the highest Ni (II), Cu (II) and Pb(II) uptake were obtained at a pH value of 6. The differences in biosorption capacities of heavy metals onto *E. rigida* at different pH values could be due to the differences in the affinities of metal ions to the molecules on the biosorbent surface. At a pH value of 9, the biosorption capacity of all metal ions were at their lowest. This may be due to the formation of anionic hydroxide complexes. These complexations may decrease the dissolved metal ion quantity and their competition with active surface sites. Therefore, all the subsequent experiments were followed by adjustment of pH values of the solutions.

Effect of particle size of biosorbent

The contact surface of the biomass with metal ions in aqueous solution has a significant role in biosorption process due to the external mass transfer resistance. The effect of particle size (Dp) on heavy metal sorption was determined within the range of 0.112 mm to 0.850 mm and results are given in Fig. 3 using optimum pH values for each metal ion. Decreasing the particle size of the biosorbent increased the surface area available for metal ions and therefore increases the biosorption capacity. Hence, a particle size range between 0.112-0.224 mm were used at the rest of the study.
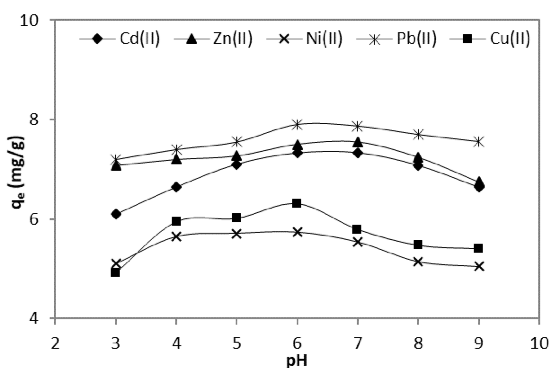
Figure 2. Effect of solution pH on heavy metal biosorption

Effect of biosorbent dosage

It is well known that the initial metal concentration and the available sorption sites on the sorbent provide the driving force to sorption according to the mass transfer
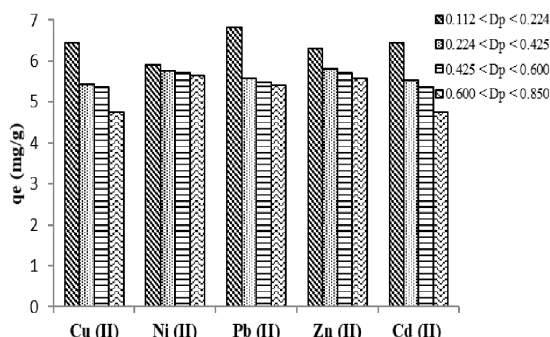
Figure 3. Effect of particle size on heavy metal biosorption (Dp, in mm)

phenomena. For biosorption to take place, mass transfer resistance between the solution and sorbate should be overcome. It is obvious that an increase in biomass dose generally increases the metal uptake because of the increases in active sites on the adsorbent surface. Whereas overlapping and partial aggregation of sorption sites may cause the decline in the amount of metal adsorbed. Such aggregation can cause to a decline in surface area of the biosorbent and increase in diffusional path. In order to investigate the effect of biomass dose for heavy metal removal, variable amounts of biosorbents (1-10 g/L) were added to solutions and the results are given in Fig.4. It is well understood that increasing the biosorbent dosage decreases the uptake amounts.

Effect of concentration, temperature and contact time

Biosorption capacities of all ions increased considerably by increasing the concentration from 10 to 50 mg/L. The explanation of this phenomenon is the driving force provided by metal ions that overcomes the mass transfer

Figure 4. Effect of biosorbent dosage on heavy metal biosorption

Table 3. Comparison of biosorption capacity (mg/g) on various sorbent materials

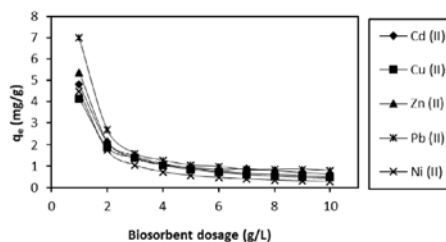| Biosorbent	Pb(II)	Zn(II)	Cu(II)	Cd(II)	Ni(II)	Reference
Wheat straw	-	-	11.4	14.5	-	[34]
Lichen (C. furcata)	12.3	-	-	-	7.9	[35]
Black carrot residues	-	-	8.8	-	5.7	[36]
Dye loaded groundnut shells	-	9.6	7.6	-	7.5	[37]
Tobacco dust	39.6	25.1	36.0	29.6	24.5	[38]
Grapefruit peel	-	-	-	42.1	46.1	[39]
Moringa pods	-	-	6.1	-	5.5	[40]
Corn cobs	8.3	-	7.6	-	13.5	[41]
Coconut dregs residue	9.7	-	2.8	-	5.9	[42]
E. rigida	18.5	14.2	12.1	11.9	10.9	Present work

resistance between the solution and solid surface. Thus quantity of metal ions adsorbed onto *E. rigida* enhanced the uptake amounts with increasing metal ion concentra-

Figure 5. Effect of contact time and temperature (Initial metal ion concentration= 50 mg/L)

tions. Fig. 5 shows the dependence of the q_t values versus contact time at different temperatures. Accordingly, q_t values increased rapidly at the initial stages with an increase in the contact time, then gradually increased and finally equilibrium was established for all metal ions. The contact time needed to reach equilibrium for all studied metal ions was found about 3 h. The obtained curves also confirm that biosorption occurred in two stages which were a very fast surface biosorption followed by a slower intracellular diffusion.

In general, there is no certain consensus about the temperature dependency of metal biosorption since surface interactions of each specific sorbate-sorbent pair effect nature of the process significantly. According to the results, biosorption capacities of *E. rigida* for all metal ions increased with an increase in the solution temperature. This indicates the endothermic nature of the biosorption. The affinities of metal ions onto *E. rigida* decreased as Pb(II) > Zn(II) > Cd(II) > Cu(II) > Ni(II) in single metal biosorption. In the applied experimental conditions, maximum capacities were determined as 18.5, 14.2, 12.1, 11.9 and 10.9 for Pb(II), Zn(II), Cu(II), Cd(II) and Ni(II) biosorption, respectively. The highest capacities obtained by using highest initial metal ion concentration (50 mg/L), temperature (40 °C) and contact time (24 h) as can be seen from Figure 5. Generally, biosorption behaviour biomass is attributed to the interactions of different functional groups found on the biosorbent surface with metal ions. And these interactions between biosorbent surface and ions and their complexation degrees are considered as the influential factors in biosorption process. Several authors concluded that soft ions (such as Pb(II)) can be adsorbed on biomass preferentially than the borderline (such as Ni(II)) and hard ions [32, 33]. This is due to the interactions of soft ions with the biomass ligands which are mainly by covalent bonding. On the other hand, hard ions interact biomass ligands exclusively by electrostatic attraction and borderline ions have intermediate properties between these two of them. Therefore, Pb(II) occupied the first position in the affinity ranking among the examined ions. Table 3 was given to make comparison between sorption capacity

Table 4. Isotherm constants for heavy metal biosorption onto *E. rigida* at 20 °C

Isotherm	Pb(II)	Zn(II)	Cu(II)	Cd(II)	Ni(II)
Langmuir					
q_m (mg/g)	21.5939	14.4927	7.3964	17.8514	16.6389
K_L (l/mg)	0.0136	0.0074	0.0662	0.0434	0.0228
R^2	0.9788	0.9780	0.9784	0.9123	0.9918
MAPE (%)	1.0937	2.8040	4.4897	5.2486	1.3809
RMSE	0.0327	0.1031	0.2120	0.1189	0.0564
Freundlich					
K_F ((mg/g) (L/mg)$^{1/n}$)	0.6282	0.9421	0.8698	1.0394	0.5538
n	1.1806	1.5790	1.9527	1.4355	1.3552
R^2	0.9990	0.9950	0.9973	0.9942	0.9975
MAPE (%)	0.9588	1.7732	1.3823	2.1129	1.6477
RMSE	0.0162	0.0303	0.0191	0.0373	0.0231
Dubinin–Radushkevich					
q_m (mg/g)	8.7758	7.1499	4.4549	7.3294	6.3041
β	7.00×10^{-6}	5.00×10^{-6}	4.00×10^{-6}	3.00×10^{-6}	8.00×10^{-6}
E	2.67×10^2	3.16×10^2	3.54×10^2	4.08×10^2	2.5×10^2
R^2	0.8816	0.8837	0.8612	0.8609	0.8857
MAPE (%)	9.0071	7.7715	11.1695	12.1275	8.0527
RMSE	0.1783	0.1508	0.1400	0.1912	0.1581
Temkin					
B	4.6449	3.0825	1.6546	3.3839	3.0366
K_T	0.2971	0.4222	0.6268	0.5990	0.2979
R^2	0.9639	0.9777	0.9777	0.9442	0.9788
MAPE (%)	9.9911	5.5342	4.7086	10.4158	6.8005
RMSE	0.5494	0.3136	0.1799	0.5757	0.2798

of *E. rigida* and similar biomass samples that were found in the literature. It can be said that the capacity of *E. rigida* was found to be compatible with the reported studies.

Equilibrium, kinetic and thermodynamic studies

Isotherm parameters obtained from the Langmuir, Freundlich, D-R and Temkin models and their respective results are given in Table 4. According to the results, heavy metal biosorption onto *E. rigida* adsorption fitted well to the Freundlich model that considers multilayer adsorption of ions. Higher values of correlation coefficients (R^2) obtained by Freundlich model also indicate the acceptability of the model of heterogeneous sorption phenomena for the system. The performance of the constructed isotherms were also statistically measured by the MAPE (Mean absolute percentage error) and RMSE (Root mean squared error) and the results were given in Table 4.

Kinetic parameters related to applied models are given in Table 5. The statistical coefficients were compared for determining the suitable kinetic models for the biosorption process. Accordingly, for all metal ions pseudo-second order kinetic model fit better with the experimental data than

other kinetic models according to the calculated correlation coefficients (R^2) MAPE (Mean absolute percentage error) and RMSE (Root mean squared error) values. The fitted pseudo-second order model is useful for predicting behaviour over the whole range of biosorption. The best fittings with this model indicate that the rate-determining step consists of chemical adsorption including valence forces through the sharing or exchange of electrons between the surface of *E. rigida* and metal ions. The intraparticle diffusion model also was plotted in order to determine the effect of mass transfer resistance on the binding of metal ions on *E. rigida*. During kinetic analysis with intraparticle diffusion model, plots of the model did not pass through the origin for all metal ions. This observations indicate that the intraparticle diffusion was not the rate-limiting step of the process due to existence of some degree of boundary layers.

In order to get a better insight into the mechanism and to ascertain the temperature dependency, spontaneity and feasibility of the biosorption process, thermodynamic parameters are calculated and the corresponding results are given in Table 6. The positive value of enthalpy change (ΔH°) revealed that biosorption of metal ions is in endothermic

Table 5. Kinetic parameters for heavy metal biosorption onto *E. rigida*

Kinetic Model	Pb(II)	Zn(II)	Cu(II)	Cd(II)	Ni(II)
Pseudo-first order					
k_1	0.0237	0.0672	0.0207	0.0089	0.0115
q_e	1.3829	6.7623	3.9591	6.0436	2.3157
R^2	0.7661	0.9737	0.9928	0.9676	0.7324
MAPE (%)	70.2501	45.7410	12.2379	3.7638	50.6705
RMSE	0.2266	0.1905	0.0304	0.0282	0.1208
Pseudo-second order					
k_2	0.0451	0.0151	0.0075	0.0068	0.0284
q_e	10.7296	9.0744	5.8548	8.1169	7.0872
R^2	0.9998	0.9972	0.9957	0.9917	0.9986
MAPE (%)	1.6060	2.0243	3.2017	2.0617	3.8259
RMSE	0.0584	0.1560	0.3025	0.2700	0.2084
Intraparticle diffusion					
k_p	0.2030	0.3723	0.3799	0.4786	0.2403
C	8.6032	4.8315	0.988	2.0886	4.4403
R^2	0.7031	0.8428	0.9558	0.9552	0.8362
MAPE (%)	3.4446	5.0141	6.7588	5.8711	4.1403
RMSE	0.3618	0.4409	0.2240	0.2841	0.2916
Elovich					
α	28282.67	13.5386	0.5830	1.2689	41.4593
β	1.4271	0.8232	0.8137	0.6654	1.2505
R^2	0.8255	0.8848	0.9864	0.9837	0.9131
MAPE (%)	2.5268	4.5257	3.4209	3.0967	4.0550
RMSE	0.2774	0.3775	0.1241	0.1713	0.2832

nature. Also, positive value of entropy change (ΔS°) showed the randomness at the biosorbent–liquid interface because of the release of water molecules, ion exchange and binding of the metal ions. Moreover, negative values of Gibbs free energy change (ΔG°) showed that biosorption was spontaneous and confirmed the affinities of the *E. rigida* towards metal ions.

Multi-metal biosorption

Biosorption in multi-component systems is accepted as a much more complex process than single component systems due to solute-solute competition and the solute-surface interactions. Therefore, binary biosorption [Ni(II)-Zn(II), Cu(II)-Pb(II), Pb(II)-Cd(II)] and ternary biosorption of Cd(II)-Pb(II)-Cu(II) experiments were performed to explain co-ion effect in the removal process.

Fig. 6 shows the binary and ternary biosorption results of heavy metals. Comparing binary biosorption results with the single metal systems showed that, uptake amounts of Ni(II) and Zn(II) ions were decreased in binary systems (Fig.6.a). In binary solutions uptake amounts were decreased due to the competition of ions for sticking on the biosorbent surface and also due to the co-ion effect. On the other

hand, the total heavy metal uptake on *E. rigida* is increased, because of the attraction of different metal ions on different surface sites. The obtained curves indicate that contact time presents a slightly increasing trend and 90 min contact time was found to be suitable for binary biosorption of Ni(II)-Zn(II). Besides, heavy metal removal was found as an endothermic process for binary biosorption as it was found for single metal systems. Analogue results were obtained for Cu(II)-Pb(II) binary system which are given in Fig. 6.b. Figure 6.c exhibits the results for Pb(II)-Cd(II) system. Likewise, the Ni(II)-Zn(II) and Cu(II)-Pb(II) binary systems, contact time increased the uptake amount to a certain value until equilibrium was established and 90 min was found to be the required time for the highest uptake amounts. Differently, Cd(II) uptake was not affected by adding Pb(II) ions into the solution. But, amount of Pb(II) biosorbed onto *E. rigida* decreased significantly in the presence of Cd(II) ion.

In order to investigate ternary metal ion biosorption, effects of initial heavy metal concentration, time and temperature were investigated. The biosorption of Cd(II)-Pb(II)-Cu(II) ions onto *E. rigida* as a function of metal ion concentrations were evaluated and uptake amounts were found lower than in the individual system, except Pb(II).

Table 6. Thermodynamic parameters calculated for heavy metal biosorption onto *E. rigida*

Metal ion	T (°C)	ΔG° (kJ/mol)	ΔH° (kJ/mol)	ΔS° (J/mol K)	R^2	MAPE (%)	RMSE
Pb(II)	20	-19.3604					
	30	-20.7203	20.17725	134.8863	0.9999	0.0256	0.0021
	40	-22.0576					
Zn(II)	20	-19.2236					
	30	-21.1083	38.7733	197.7568	0.9982	0.2697	0.0250
	40	-23.1828					
Cu(II)	20	-20.3364					
	30	-21.1669	8.3863	97.8252	0.9098	0.3144	0.0283
	40	-22.2994					
Cd(II)	20	-20.7013					
	30	-21.6591	15.9853	124.8357	0.9046	0.6034	0.0555
	40	-23.2110					
Ni(II)	20	-17.5471					
	30	-18.8666	14.6767	110.1605	0.9343	0.5285	0.0417
	40	-19.7405					

When the effect of contact time was analysed, the time to reach equilibrium for all metals was nearly same for single and binary systems as it is seen in Fig 6.d. For ternary metal biosorption, temperature showed a slightly increasing effect on the uptake amount of ions likewise single metal solutions. Consequently, competition among heavy metals affected uptake amounts of metals in binary and ternary metal systems significantly.

SEM-EDX Analysis

SEM-EDX is a beneficial method to determine the element existence by the help of characteristic X-ray energy. SEM–EDX analysis was performed on samples before and after biosorption to investigate textural properties and, thereafter, to understand binding of metal ions to the sorbent surface. Several sites on the *E. rigida* were analyzed after biosoption and their respective X-ray spectra are shown
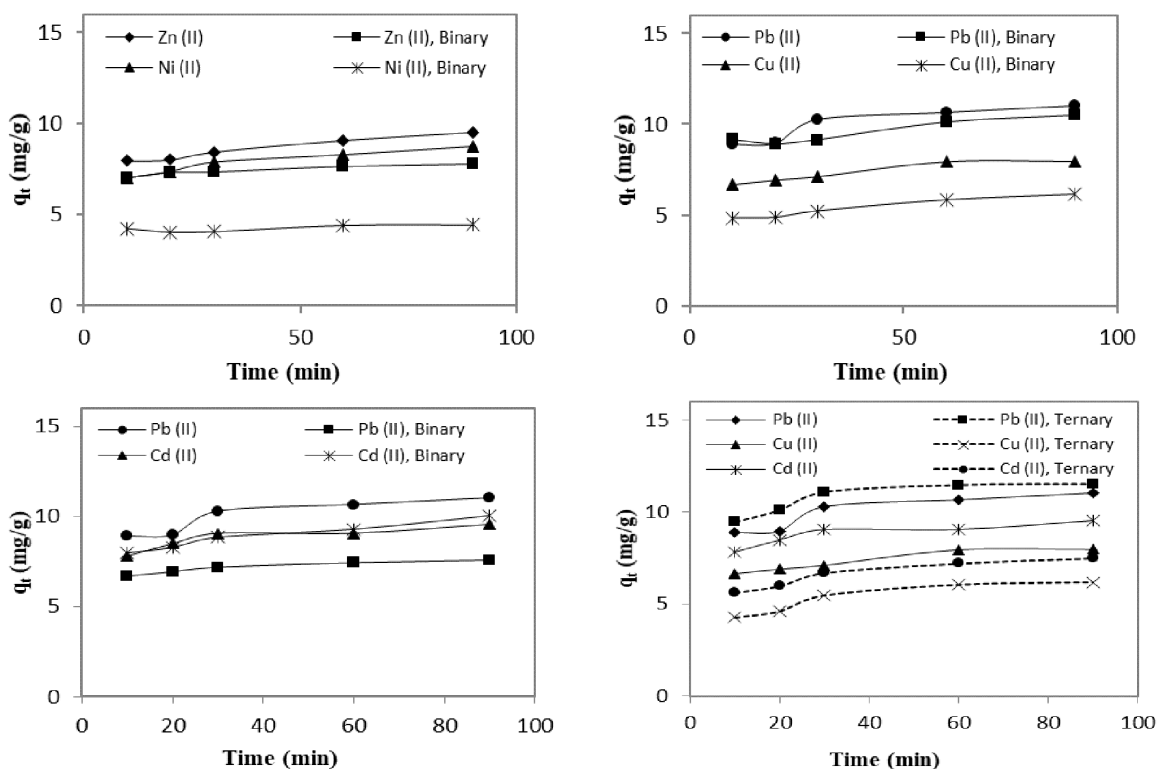

Figure 6. Effect of contact time for single, binary and ternary metal solutions (Initial metal ion concentration= 50 mg/L)

in Fig.7. From top to bottom, EDX spectra confirm that Cd(II), Cu(II), Ni(II), Pb(II) and Zn(II) ions stick on the surface and pores of *E.rigida* which can be understood from red dots seen in the micrographs. Furhermore, internal cavities after heterogeneous distribution of metal ions exist on the surface. These features were identical to the morphological descriptions of *E.rigida* regardless of the type of the ion.

CONCLUSIONS

This present study demonstrated the results of the biosorption process for the removal of Pb(II), Zn(II), Cu(II), Cd(II) and Ni(II) ions from aqueous solution using an arid land plant biomass. According to the uptake amounts, the affinities of the metal ions to adsorption sites decreased in the order of Pb(II) > Zn(II) > Cd(II) > Cu(II) > Ni(II) in single metal containing solutions. For the single metal containing systems, Freundlich isotherm gives the best correlation for heavy metal biosorption. Kinetic modelling showed that the data perfectly complied with pseudo-second order model. Thermodynamic analysis showed that process is endothermic and spontaneous. In multi-metal systems, the uptake amounts for both metals were significantly changed in the

presence of co-ions. But, presence of co-ions had no effect on equilibrium time and temperature dependency of the biosorption process. *E. rigida* proved itself as an alternative low cost biosorbent for removing heavy metals.Results suggested that non-edible biomass species can be incorporated in decentralized water treatment systems to offer a simple option for treating the low concentrations of heavy metals.

REFERENCES

[1] Runtti H, Tuomikoski S, Kangas T, Lassi U, Kuokkanen T, Rämö J. Chemically activated carbon residue from biomass gasification as a sorbent for iron(II), copper(II) and nickel(II) ions. Journal of Water Process Engineering 4 (2014) 12–24.

[2] Uzun I, Güzel F. Adsorption of some heavy metal ions from aqueous solution by activated carbon and comparison of percent adsorption results of activated carbon with those of some other adsorbents. Turkish Journal of Chemisty 24 (3) (2000) 291–298.

[3] Xing Y, Yang P, Yu J. Biosorption of Pb (II) by the shell of vivipaird snail: Implications for heavy metal bioremediation. Separation Science and Technology 51(17) (2016) 2756–2761.

[4] Al–Shannag M, Al–Qodah Z, Bani–Melhem K, Qtaishat MR, Alkasrawi M. Heavy metal ions removal from metal plating wastewater using electrocoagulation: Kinetic study and process performance. Chemical Engineering Journal 260 (2015) 749–756.

[5] Arpa Ç, Say R, Şatıroğlu N, Bektaş S, Yürüm Y, Genç Ö. Heavy metal removal from aquatic systems by northern Anatolian smectites. Turkish Journal of Chemisty 24 (2) (2000) 209–215.

[6] Hankins N, Hilal N, Ogunbiyi OO, Azzopardi B. Inverted polarity micellar enhanced ultrafiltration for the treatment of heavy metal polluted wastewater. Desalination 185 (1) (2005) 185–202.

[7] Demiral İ, Şamdan CA. Removal of Methylene Blue with Activated Carbon Obtained from Pumpkin Seed Shell. Journal of Turkish Chemical Society Section A: Chem. 2 (3) (2015) 25–28.

[8] Oladoja NA, Ahmad A. Gastropod shell as a precursor for the synthesis of binary alkali–earth and transition metal oxide for Cr(VI) abstraction from aqua system. Separation and Purification Technology 116 (2013) 230–239.

[9] Khan ASA. Evaluation of thermodynamic parameters of cadmium adsorption on sand from Temkin adsorption isotherm. Turkish Journal of Chemisty 36 (3) (2012) 437–443.

[10] Machado RM, Correia MJN, Carvalho JMR. Integrated process for biosorption of copper from liquid effluents using grape stalks. Separation Science and Technology 38 (10) (2003) 2237–2254.

[11] Reddy DHK, Lee SM, Seshaiah K. Biosorption of toxic heavy metal ions from water environment using honeycomb biomass–an industrial waste material. Water, Air, & Soil Pollution 223 (9) (2012) 5967–5982.

[12] Jacques RA, Lima EC, Dias SLP, Mazzocato AC, Pavan FA. Yellow passion–fruit shell as biosorbent to remove Cr(III) and Pb(II) from aqueous solution. Separation and Purification Technology 57(1) (2007) 193–198.

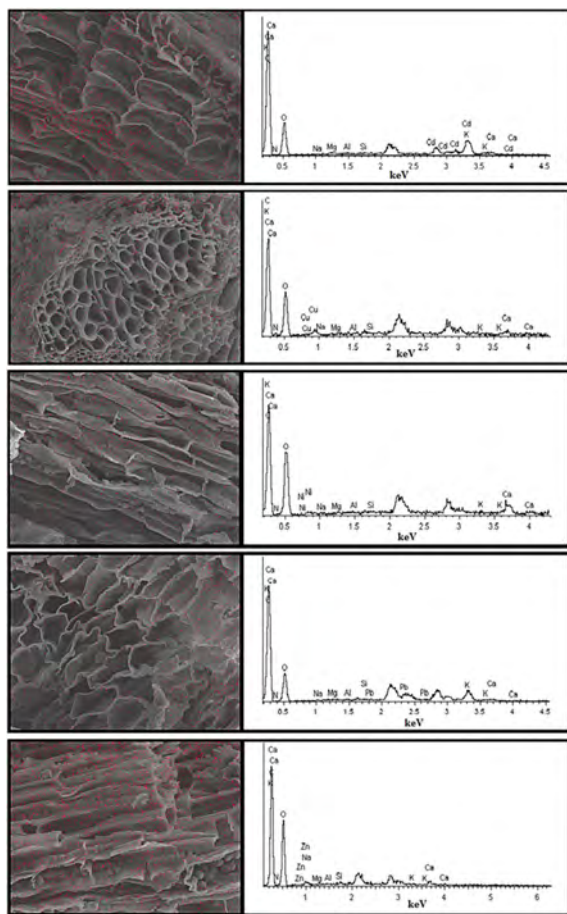[13] Semerjian L. Equilibrium and kinetics of cadmium adsorption

Figure 7. SEM micrographs and EDX spectra of *E. Rigida* after heavy metal biosorption

from aqueous solutions using untreated Pinus halepensis sawdust. Journal of Hard Materials 173 (2010) 236–242.

[14] Lee MG, Lim JH, Kam SK. Biosorption characteristics in the mixed heavy metal solution by biosorbents of marine brown algae. Korean Journal of Chemical Engineering 19 (2) (2002) 277–284.

[15] Velazquez–Jimenez LH, Pavlick A, Rangel–Mendez JR. Chemical characterization of raw and treated agave bagasse and its potential as adsorbent of metal cations from water. Industrial Crops and Products 43 (2013) 200–206.

[16] Ateş F, Pütün AE, Pütün E. Catalytic pyrolysis of perennial shrub, Euphorbia rigida in the water vapour atmosphere Journal of Analytical and Applied Pyrolysis 73 (2005) 299–304.

[17] Kılıç M, Apaydın–Varol E, Pütün AE, Preparation and surface characterization of activated carbons from Euphorbia rigida by chemical activation with ZnCl2, K2CO3, NaOH and H3PO4. Applied Surface Science 261 (2012) 247–254.

[18] Langmuir I. The constitution and fundamental properties of solids and liquids. Journal of the American Chemical Society 38 (1916) 2221–2295.

[19] Langmuir I. The adsorption of gases on plane surfaces of glass, mica and platinum. Journal of the American Chemical Society 40 (1918) 1361–1403.

[20] Topallar H. The Adsorption Isotherms of the Bleaching of Sun ower–Seed Oil. Turkish Journal of Chemistry 22 (2) (1998) 143–148.

[21] Freundlich HMF. Über die adsorption in lösungen. Zeitschrift für Physikalische Chemie. 57 (1906) 385–470.

[22] Dubinin MM, Radushkevich LV. Equation of the characteristic curve of activated charcoal. Proceedings of the USSR Academy of Sciences 55 (1947) 331.

[23] Temkin MJ, Phyzev V. Recent modifications to Langmuir Isotherms. Acta Physicochimica USSR 12 (1940) 217–222.

[24] Lagergren S. Zurtheorie der sogenannten adsorption gelosterstoffe. Kungliga Svenska Vetenskapsakademiens. Handlingar 24 (1898) 1-39.

[25] Ho YS, McKay G. Pseudo–second order model for sorption process. Process Biochemistry 34 (1999) 451–465.

[26] Weber WJ, Morriss JC. Kinetics of adsorption on carbon from solution. Journal of the Sanitary Engineering Division American Society of Civil Engineers 89 (1963) 31–60.

[27] Chen JP, Wu S, Chong KH. Surface modification of a granular activated carbon by citric acid for enhancement of copper adsorption. Carbon 41 (2003) 1979–1986.

[28] Elkady MF, Ibrahim AM, El–Latif MMA. Assessment of the adsorption kinetics, equilibrium and thermodynamic for the potential removal of reactive red dye using eggshell biocomposite beads. Desalination 278 (2011) 412–423.

[29] Elovich SY, Larionov OG. Theory of adsorption from solutions of non–electrolytes on solid (I) equation adsorption from solutions and the analysis of its simplest form, (II) verification of the equation of adsorption isotherm from solutions. Russian Chemical Bulletin 2 (1962) 209.

[30] Can C, Jianlong W. Correlating metal ionic characteristics with biosorption capacity using QSAR model. Chemosphere 69 (2007) 1610–1616.

[31] Escudero C, Poch J, Villaescusa I. Modelling of breakthrough curves of single and binary mixtures of Cu(II), Cd(II), Ni(II) and Pb(II) sorption onto grape stalks waste. Chemical Engineering Journal 217 (2013) 129–138.

[32] Dang VBH, Doan HD, Dang–Vu T, Lohi A. Equilibrium and kinetics of biosorption of cadmium (II) and copper (II) ions by wheat straw. Bioresource Technology 100 (2009) 211–219.

[33] Sarı A, Tuzen M, Uluözlü ÖD, Soylak M. Biosorption of Pb(II) and Ni(II) from aqueous solution by lichen (Cladonia furcata) biomass. Biochemical Engineering Journal 37 (2007) 151–158.

[34] Güzel F, Yakut H, Topal G. Determination of kinetic and equilibrium parameters of the batch adsorption of Mn(II), Co(II), Ni(II) and Cu(II) from aqueous solution by black carrot (Daucus carota L.) residues. Journal of Hazardous Materials 153 (2008) 1275–1287.

[35] Shukla SR, Pai RS. Adsorption of Cu(II), Ni(II) and Zn(II) on dye loaded groundnut shells and sawdust. Separation and Purification Technology 43 (2005) 1–8.

[36] Qi BC, Aldrich C. Biosorption of heavy metals from aqueous solutions with tobacco dust. Bioresource Technology 99 (2008) 5595–5601.

[37] Torab–Mostaedi M, Asadollahzadeh M, Hemmati A, Khosravi A. Equilibrium, kinetic, and thermodynamic studies for biosorption of cadmium and nickel on grapefruit peel. Journal of the Taiwan Institute of Chemical Engineers 44 (2) (2013) 295–302.

[38] Matouq M, Jildeh N, Qtaishat M, Hindeyeh M, Al Syouf MQ. The adsorption kinetics and modeling for heavy metals removal from wastewater by Moringa pods. Journal of Environmental Chemical Engineering 3(2) (2015) 775–784.

[39] Vaughan T, Seo CW, Marshall WE. Removal of selected metal ions from aqueous solution using modified corncobs. Bioresource Technology 78 (2001) 133–139.

[40] Kamari A, Yusoff SNM, Abdullah F, Putra WP. Biosorptive removal of Cu(II), Ni(II) and Pb(II) ions from aqueous solutions using coconut dregs residue: Adsorption and characterisation studies. Journal of Environmental Chemical Engineering 2 (4) (2014) 1912–1919.

Optical sensing of mercury using fluorescent silver and gold nanoclusters

Mehmet Gökhan Çağlayan (ID)
Ankara University, Faculty of Pharmacy, Department of Analytical Chemistry, Ankara, TURKEY

ABSTRACT

In this study, gold and silver nanoclusters were employed for optical sensing of mercury. Nanoclusters used in this research had different chemical properties and showed different interactions with mercury producing specific optical responses including UV-Vis absorbance and fluorescence. These responses were quantitatively studied in the solution phase. The sensitive methods developed in this study were tested using mercury standards and accurate and precise results were obtained. Optical responses could also be monitored by naked eye. Finally, portable and simple glass fiber pads were developed for mercury sensing.

Keywords:
Mercury sensing, optical sensors, gold nanoclusters, silver nanoclusters, fluorescence, colorimetry, portable optical devices

INTRODUCTION

Mercury has neurotoxic, teratogenic, nephrotoxic and immunotoxic effects on human health [1-3]. Humans are exposed to mercury from different sources such as release from dental amalgams, gold mining activities, application of thiomersal-containing vaccines and industrial discharge to the environment [4]. Although mercury pollution is rare compared to other types of pollutions, it is strictly followed in environmental samples such as seawater and drinking water and is restricted by national and international regulations due to its hazardous effects on the ecosystem and human health. According to the Ministry of Health of Turkey, the concentration of mercury in drinking water must not exceed 1 μg/L (~5 nM) and the limit defined by the United States Environmental Protection Agency is 2 μg/L (~10 nM). Such a low amount of mercury can generally be analyzed only by highly sensitive analytical techniques such as inductively coupled plasma, mass spectrometry [5-6] fluorescence sensing [7-8], high performance liquid chromatography, cold vapor atomic fluorescence spectroscopy [9], and resonance Rayleigh scattering aptasensors [10].

Although developing a method for any forms of mercury is worthwhile, all Hg forms produce Hg^{2+} and most studies have focused on the development of mercury sensors through Hg^{2+} sensing [4,11-13].

Recently, a considerable number of nanoparticle-based sensors for ultra-sensitive analysis have been developed due to the lower cost and versatile and modifiable features of these materials and the simplicity of their synthesis and analysis [12-13]. There are different mechanisms for Hg nanosensing and the easiest is the aggregation of nanoparticles in the presence of Hg^{2+} [14]. Silver nanoparticles result in the reduction of Hg^{2+} and an Hg-Ag amalgam can be formed on the surface of nanoparticles when the size of the silver nanoparticles are below 32 nm [15]. When this occurs, optical responses such as shifting surface plasmon resonance (SPR) bands and fluorescence quenching can be observed. Another strategy is based on the affinity of thymine to Hg^{2+} ions [16], in which the thymine-thymine mismatched base pair is stabilized by Hg^{2+} with a size that perfectly fits the double stranded DNA without the steric disturbance of the helical structure. Other mechanisms in fluorescence nanosensing include energy transfer and electron transfer between analytes and sensors.

There are various types of luminescent nanomaterials that can be used in optical sensing of analytes and they introduce different mechanisms in sensing methods. The most employed luminescent particles in nanosensing are quantum dots [7,17]. Recently, as an alternative to quantum dots, nanoclusters of noble metals have been employed in this area [18].

Gold nanoclusters (AuNC) and silver nanoclusters (AgNC) are preferred particularly due to their easy synthesis, biocompatibility, and photostability.

In this study, AgNC and AuNC were used for Hg^{2+} sensing. Their fluorescence and absorbance signals were monitored after the addition of Hg^{2+}. Finally, the method was transferred to glass fiber pads for a simple and on-site analysis of Hg^{2+}.

METHOD
Materials and instrumentation
NaOH, $HAuCl_4$, $Hg(NO_3)_2$, $NaBH_4$, KNO_3, $NaNO_3$, $Ca(NO_3)_2$, $Fe(NO_3)_2$, $Mg(NO_3)_2$, $Ba(NO_3)_2$, $Pb(NO_3)_2$, α-Lipoic acid, L-glutathione, and Whatman No 1 Chr chromatography paper were purchased from Sigma-Aldrich (Mannheim, Germany). Mercury reference standard was purchased from Ultra Scientific Analytical Solutions (Rhode Island, USA). Glass fibers conjugate pad sheets and absorbent pads were obtained from Merck Millipore (Darmstadt, Germany).

Fluorescence spectra were measured with an Agilent Cary Eclipse Fluorescence Spectrophotometer and absorption spectra were recorded using an Agilent Cary 60 UV-Vis spectrophotometer (Agilent Technologies, California, USA). The temperatures of spectroscopic measurements were maintained at 25 °C with an Agilent Peltier temperature controller accessory. A Desaga Uvis lamp was used for the UV light (366 nm) for the photographs (Jahnsdorf, Germany).

Synthesis of gold nanoclusters
Gold nanoclusters were synthesized using the method proposed by Zhang et al. [19] which utilizes glutathione for stabilization. Briefly, 10 mL of 10 mM $HAuCl_4$ and 10 mL 15 mM glutathione were mixed vigorously for 2 min. Then, 2 mL of 1 M NaOH was added to the mixture. Finally, the solution was stirred at 200 rpm at 37 °C for 24 h. The yellow solution of gold nanoclusters was washed to remove the excess glutathione followed by the addition of 80 mL of methanol. Then, the mixture was centrifuged at 9000 rpm for 20 min. The precipitates were dispersed in 20 mL of ultrapure water and kept under dark room conditions.

Synthesis of silver nanoclasters
The method described by Patrick et al. [20] was used for the synthesis of AgNC. 19 mg α-lipoic acid was added to 14 mL of ultrapure water followed by the addition of 7 mg $NaBH_4$ while stirring. After 30 min of stirring, a clear solution was obtained. Then, first 700 μL of 25 mM $AgNO_3$, then 2 mL of 0.13 M $NaBH_4$ were added. The flask was covered with an aluminum foil to keep it away from

light. After stirring for 5 h, orange AuNCs were formed which were then stored at dark.

Hg^{2+} sensing in the solution phase
AgNCs were first diluted 1:4 with distilled water and AuNCs were directly used since their fluorescence signals were not intense. Analytes were prepared in water and were directly added to the clusters. All the fluorescence measurements were recorded at 25 °C by controlling the temperature using a Peltier accessory. Preliminary tests were performed by adding possible interferences to the nanoclusters and photographs were taken. by placing the analytes under white light and UV-light for colorimetric and fluorimetric responses. All titrations were performed using a stock solution of 10 μM $Hg(NO_3)_2$. Certified mercury standards were used as real samples.

Hg^{2+} sensing on glass fiber pads
Glass fiber pads were cut in the dimensions of 2 mm 8 mm. Time for immersion of pads in AgNC was optimized by measuring the fluorescence intensities at different times (5 s, 8 s, 10 s, 12 s, and 15 s). The pads were immersed in the AgNC solution for 8 s and left to dry at room temperature. Once the pads were dry, 12 μL of the blank solution and samples (1 nM, 10 nM, 100 nM, and 1000 nM Hg^{2+}) were pipetted onto pads and left to dry again. Then, photographs of the pads were taken under white and UV lights (366 nm).

RESULTS AND DISCUSSION
The reference methods report that AgNC (ϕ= ~5.0%) have higher quantum yield than AuNC (ϕ= ~1.5%). [19-20] This can clearly be observed in photographs taken under UV light (Figures 1a and 2a). Nevertheless, the effect of Hg^{2+} on fluorescence intensity can be easily observed for both nanoclusters even by naked eye. However, the colorimetric responses and UV-Vis absorption titrations reveal that the mechanism of Hg^{2+} sensing is different in these nanoclusters. While Hg^{2+} produces a colorimetric response in AgNC, which is indicated by the disappearance of yellow (Figure 1a), no colorimetric response is observed when Hg^{2+} is introduced to AuNC (Figure 2a). The colorimetric response obtained by AgNC can be quantified using the UV-Vis absorption spectra (Figure 1b). Fluorescence signals show similar responses to colorimetry in AgNC. When Hg^{2+} is introduced, the aggregation of AgNC can be observed by the disappearance of color and fluorescence quenching. The mechanism in Hg^{2+} sensing by AgNC can be the reduction of Hg^{2+} followed by the formation of Ag-Hg amalgam formation. In this study, these colorimetric and fluorimetric responses were monitored by time in the kinetic mode of a fluorescence spectrophotometer and it was found that the reaction occurred immediately
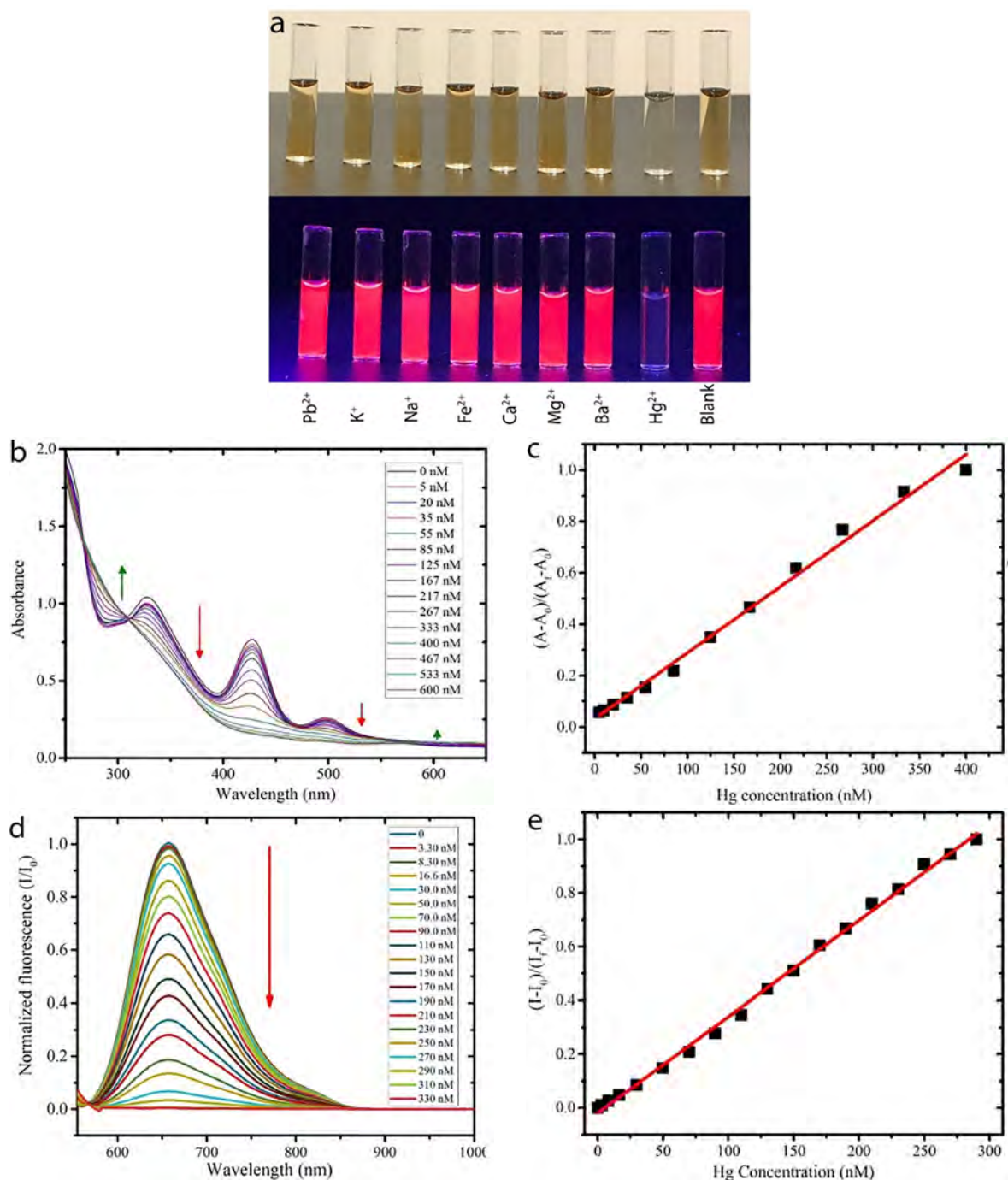
Figure 1. a) Naked eye detection of Hg^{2+} among some other cations using AgNC b) UV-Vis absorption titration spectra of Hg^{2+} and AgNC, c) Calibration curve for Hg^{2+} and AgNC UV-Vis titration, d) Fluorescence titration spectra of Hg^{2+} and AgNC e) Calibration curve for Hg^{2+} and AgNC fluorescence titration.

after the addition of Hg^{2+}.

Besides, the responses were concentration-dependent; thus, can be used in quantitative analysis. On the other hand, AuNC responded to the addition of Hg^{2+} in a different way. Although the absorbance spectrum of AuNC was not affected by Hg^{2+}, the fluorescence was quenched. In this case, the suggested mechanism was not the aggregation of AuNC,

but it was probably the formation of a complex between Hg^{2+} and the carboxyl group of glutathione on the surface of AuNC. Then a photo-induced electron transfer from AuNC to Hg^{2+} complex might occur. This phenomenon can also be observed in some quantum dot-based sensing. [21]

In brief, colorimetric and fluorimetric responses were obtained from AgNC while only fluorimetric response was
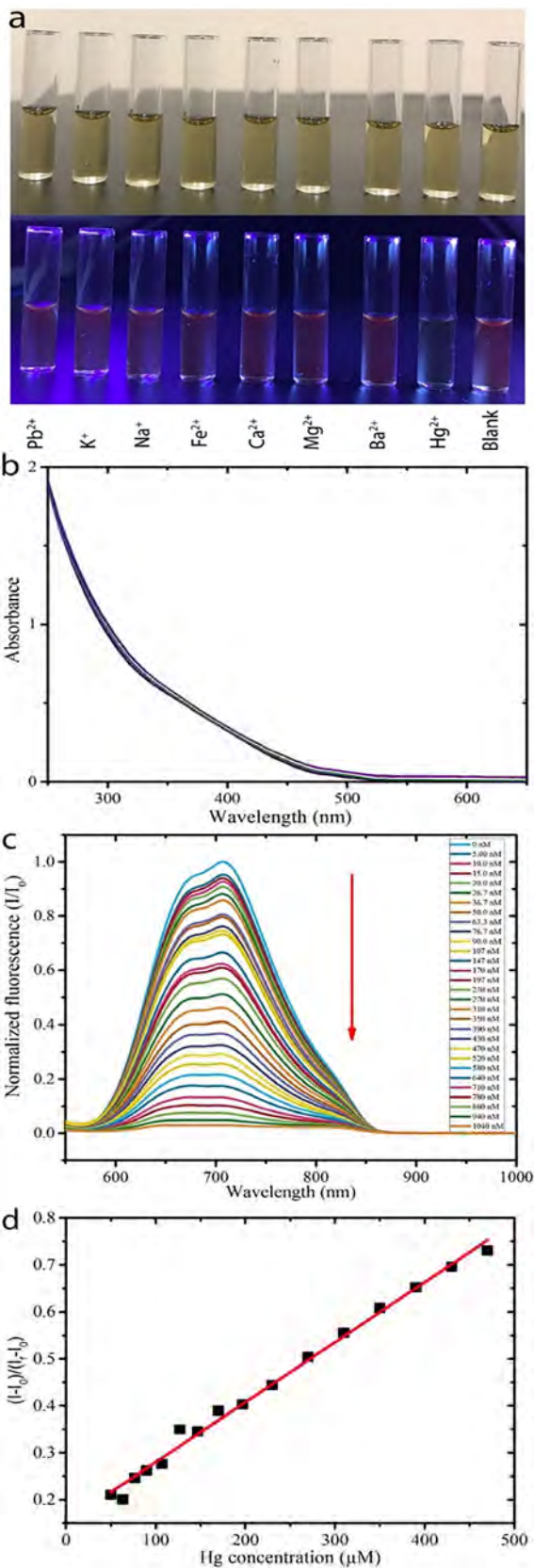
Figure 2. a) Naked eye detection of Hg²⁺ among some other cations using AuNC, b) UV-Vis absorption titration spectra of Hg²⁺ and AuNC, c) Fluorescence titration spectra of Hg²⁺ and AuNC d) Calibration curve for Hg²⁺ and AuNC fluorescence titration.

observed for AuNC. This creates a specific response pattern (Figure 3) for Hg^{2+} cation. The obtained response pattern increases the selectivity of Hg^{2+} sensing and is especially important in this type of sensor, which does not employ any analyte-specific agents. There is usually a contradiction between the selectivity and simplicity/cost-effectiveness of analytical methods. When an analytical method concentrates on high selectivity, its generally complexity and cost increase or vice versa. Thus, using two or more less selective sensors rather than expensive and highly selective analyte-specific agents (antibody, aptamer, etc) allows obtaining required information to analyze a sample. Here, only two simple nanoclusters were employed for Hg^{2+} sensing and they interacted with the analyte using different mechanisms; thus, selective sensing of Hg^{2+} was achieved following a very simple and cost-effective synthesis method. The effects of some selected metals were also followed under white light and UV-light and no interference was observed (Figures 1a and 2a).

Firstly, UV-Vis titrations were performed for both nanoclusters (Figures 1b and 2b). The responses from the AgNC-Hg^{2+} UV-Vis titration were used for quantitative determination (Figure 1c). Then, isosbestic points (312 nm and 539 nm) were determined from the UV-Vis spectra for the determination of the excitation wavelength in the fluorescence titration of AgNC and Hg^{2+}. Although the highest emission for AgNC was observed when it was excited at 432 nm, titrations were realized at an excitation wavelength of 539 nm since emission is independent from absorbance changes at isosbestic points, thus resulting in better correlation factors between Hg^{2+} and fluorescence quenching. Fluorescence of AgNC started to quench at around 1 nM Hg^{2+} and total quenching was achieved upon the addition of 330 nM Hg^{2+} to AgNC (Figure 1d). A linear correlation was observed between AgNC and Hg^{2+} (Figure 1e). On the other hand, fluorescence titration of AuNC and Hg^{2+} indicated a non-linear relationship in a wide range (Figure 2c). For this reason, the range of titration between 50-470 nM Hg^{2+} that showed a linear relationship was used for the calibration (Figure 2d). Both titrations were carried out in water at 25 °C. Some of the validation parameters

Table 1. Some method validation parameters for Hg^{2+} sensing

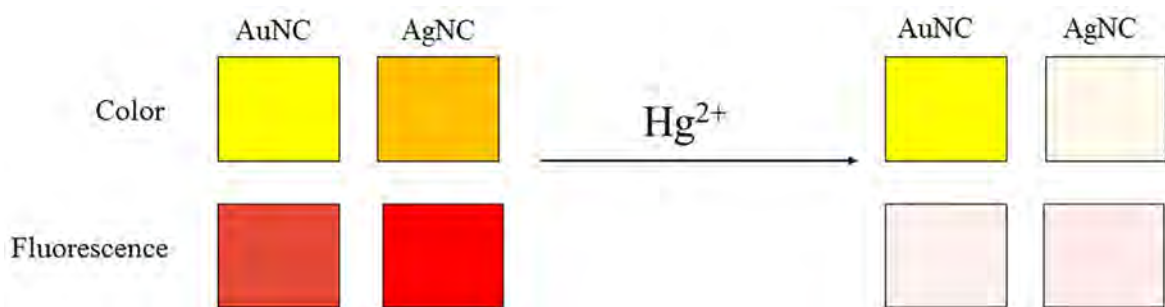|	Silver nanoclusters		Gold nanoclusters
	Fluorescence	UV-Vis	Fluorescence
Linear range (nM)	3.3-290	5-400	50-470
Detection limit (nM)	1.04	1.65	1.84
Quantitation limit (nM)	3.16	5.00	5.59
Slope	0.003586	0.002571	0.001277
Intercept	-0.01913	0.03248	0.1520
Coefficient of determination	0.9974	0.9928	0.9922

Figure 3. Optical response pattern obtained from nanoclusters

such as linear range, detection and quantification limits, and the coefficient of determination for both nanoclusters are given in Table 1. Finally, the certified mercury standard solutions were analyzed to test the accuracy and precision of the method. The results demonstrate high accuracy and precision at low levels of concentration (Table 2).

After analyzing the nanocluster-mercury interaction in the solution phase, the method was transferred to glass fiber pads which are commonly used in lateral flow immunoassay applications as sampling or conjugation pads. Here, the aim was to develop simple, user-friendly, cheap and disposable devices applicable to the on-site analysis of mercury. For this purpose, different types of paper such as chromatography paper, nitrocellulose absorbent pads and glass fiber pads were tested. As expected, the sensitivity of all materials was found to be lower compared to the solution-based method. Among these materials, the best performance in terms of sensitivity was obtained from glass fibers. This may be attributed to their higher sample absorption capacity and lower material density.

Small strips of glass fiber pads were immersed in AgNC to absorb the nanoclusters. The time taken for the pads for complete absorption were determined by studying the fluorescence of pads after keeping them in AgNC at different time intervals (5 s, 8 s, 10 s, 12 s, and 15 s). The results showed that pads were saturated with AgNC in 8 s and this condition was used in further experiments.

After solvent evaporation at room temperature, the fluorescence of AgNC in glass fiber pads under UV-light could be observed even by naked eye. Then, Hg^{2+} samples were applied to pads at different concentrations and the photographs of pads were taken using a mobile phone under sunlight and UV-light (Figure 4a). Although naked-eye detection of color change was difficult at lower concentrations (1 nM and 10 nM), the change was clearly seen at higher concentrations (100 nM and 1000 nM). On the other hand, it was easier to detect the change in fluorescence even at low concentrations. This is mostly because the red fluorescence of AgNC was not interfered with other lights. If the nanosensors had blue fluorescence, it would be difficult to apply this method since strong scattering of paper materials can suppress the blue fluorescence of sensor. Thus, another advantage of nanoparticles is that their optical properties can be easily modified to meet the requirements of sensing. For better quantification, the blue channel of the photo was removed and fluorescence intensities were measured using the Image J software. Considering the simplicity of the experimental setup and application, it can be concluded that the fluorescence intensity and Hg^{2+} concentration was correlated (Figure 4b) and this method can be used in the quantitative determination of Hg^{2+} in drinking water.

Table 2. Accuracy and precision of the Hg^{2+} sensing

| Concentration of certified reference	Found	Relative standard deviation (%)	Relative error (%)
		Silver nanoclusters fluorescence measurements	
5.0 nM	4.8 nM	2.54%	-3.38%
50.0 nM	49.0 nM	3.98%	-2.07%
100.0 nM	101.5 nM	1.71%	1.53%
		Silver nanoclusters UV-Vis measurements	
10.0 nM	10.6 nM	2.72%	6.21%
100.0 nM	101.5 nM	1.63%	1.49%
200.0 nM	202.9 nM	2.72%	1.46%
		Gold nanoclusters fluorescence measurements	
60.0 nM	61.7 nM	2.87%	2.78%
120.0 nM	122.4 nM	0.12%	2.03%
240.0 nM	236.7 nM	2.05%	-1.38%
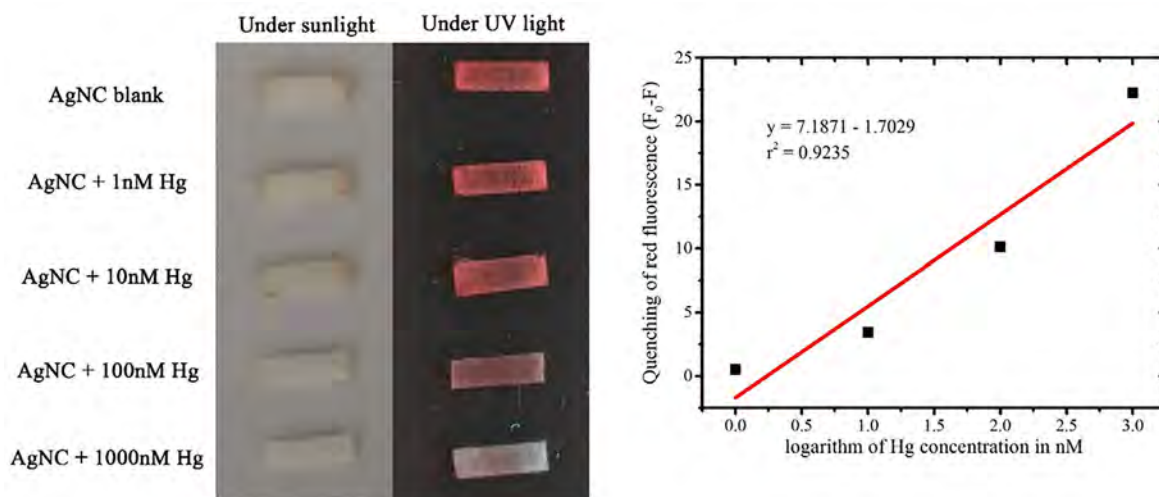
Figure 4. Photo of glass fiber pads under sunlight and under UV light (left) and the curve showing correlation between logarithm of Hg^{2+} concentration and fluorescence quenching.

CONCLUSION

In this study, sensitive and easy-to-use assays were developed for the determination of Hg^{2+} cation in water. Optical responses obtained after interactions between nanoclusters and Hg^{2+} were used in the analysis. Colorimetric and fluorimetric responses created a response pattern for the Hg^{2+} cation, which increases the selectivity of this simple method. The sensitive method was successfully applied to certified mercury standards. Finally, the proposed method based on AgNC was implemented in glass fiber pads to develop disposable, cheap, simple, portable, and sensitive devices. However, the fluorescence of AuNC was not sufficient for Hg^{2+} sensing by this simple setup since the quantum yield of AuNC was low. Therefore, further studies are needed to increase the quantum yield through the modification of AuNC.

REFERENCES

1. Counter SA, Buchanan LH, Ortega F, Laurell G. Elevated blood mercury and neuro-otological observations in children of the Ecuadorian gold mines. Journal of Toxicology and Environmental Health-Part A65 (2002) 149–163.

2. Ratcliffe HE, Swanson GM, Fischer LJ. Human exposure to mercury: A critical assessment of the evidence of adverse health effects. Journal of Toxicology and Environmental Health 49 (1996) 221–270.

3. Sweet LI, Zelikoff JT. Toxicology and immunotoxicology of mercury: A comparative review in fish and humans. Journal of Toxicology and Environmental Health-Part B-Critical Reviews 4 (2001) 161–205.

4. Branco V, Caito S, Farina M, Teixeira da Rocha J, Aschner M, Carvalho C. Biomarkers of mercury toxicity: Past, present, and future trends. Journal of Toxicology and Environmental Health – Part B: Critical Reviews (2017) 1–36.

5. de Souza SS, Campiglia AD, Barbosa Jr F. A simple method for methylmercury, inorganic mercury and ethylmercury determination in plasma samples by high performance liquid chromatography-cold-vapor-inductively coupled plasma mass spectrometry. Analytica Chimica Acta 761 (2013)11–17.

6. Fu L, Shi S-Y, Chen X-Q. Multi-element analysis of water decoction of medicine food homology plants using inductively coupled plasma-tandem mass spectrometry. Spectrochimica Acta Part B: Atomic Spectroscopy 133 (2017) 34–39.

7. Gu W, Pei X, Cheng Y, Zhang C, Zhang J, Yan Y, et al. Black Phosphorus Quantum Dots as the Ratiometric Fluorescence Probe for Trace Mercury Ion Detection Based on Inner Filter Effect. ACS Sensors 2 (2017) 576–582.

8. Zhang JR, Huang WT, Zeng AL, Luo HQ, Li NB. Ethynyl and ℗-stacked thymine-Hg^{2+}-thymine base pairs enhanced fluorescence quenching via photoinduced electron transfer and simple and sensitive mercury ion sensing. Biosensors and Bioelectronics 64 (2015) 597–604.

9. Liu Y-M, Zhang F-P, Jiao B-Y, Rao J-Y, Leng G. Automated dispersive liquid-liquid microextraction coupled to high performance liquid chromatography – cold vapour atomic fluorescence spectroscopy for the determination of mercury species in natural water samples. Journal of Chromatography A 1493 (2017) 1–9.

10. Ren W, Zhang Y, Chen HG, Gao ZF, Li NB, Luo HQ. Ultrasensitive Label-Free Resonance Rayleigh Scattering Aptasensor for Hg^{2+} Using Hg^{2+}-Triggered Exonuclease III-Assisted Target Recycling and Growth of G-Wires for Signal Amplification. Analytical Chemistry 88 (2016) 1385–1390.

11. Botasini S, Heijo G, Méndez E. Toward decentralized analysis of mercury (II) in real samples. A critical review on nanotechnology-based methodologies. Analytica Chimica Acta 800 (2013) 1–11.

12. Ding Y, Wang S, Li J, Chen L. Nanomaterial-based optical sensors for mercury ions. TrAC Trends in Analytical Chemistry 82 (2016) 175–190.

13. Xu X, Li Y-F, Zhao J, Li Y, Lin J, Li B, et al. Nanomaterial-based approaches for the detection and speciation of mercury. Analyst 140 (2015) 7841–7853.

14. Farhadi K, Forough M, Molaei R, Hajizadeh S, Rafipour A. Highly selective Hg2+ colorimetric sensor using green synthesized and unmodified silver nanoparticles. Sensors and Actuators B: Chemical 161 (2012) 880–885.

15. Katok KV, Whitby RLD, Fukuda T, Maekawa T, Bezverkhyy I, Mikhalovsky SV, et al. Hyperstoichiometric Interaction Between Silver and Mercury at the Nanoscale. Angewandte Chemie International Edition 51 (2012) 2632–2635.

16. Ono A, Togashi H. Highly Selective Oligonucleotide–Based Sensor for Mercury(II) in Aqueous Solutions. Angewandte Chemie International Edition 43 (2004) 4300–4302.

17. Li H, Zhang Y, Wang X, Gao Z. A luminescent nanosensor for Hg(II) based on functionalized CdSe/ZnS quantum dots. Microchimica Acta 160 (2008) 119–123.

18. Diez I, Ras RHA. Fluorescent silver nanoclusters. Nanoscale 3 (2011)1963–1970.

19. Zhang H, Liu Q, Wang T, Yun Z, Li G, Liu J, et al. Facile preparation of glutathione–stabilized gold nanoclusters for selective determination of chromium (III) and chromium (VI) in environmental water samples. Analytica Chimica Acta 770 (2013) 140–146.

20. Chin PTK, van der Linden M, van Harten EJ, Barendregt A, Rood MTM, Koster AJ, et al. Enhanced luminescence of Ag nanoclusters via surface modification. Nanotechnology 24 (2013) 075703/1–/7, 7 pp.

21. Shang ZB, Wang Y, Jin WJ. Triethanolamine–capped CdSe quantum dots as fluorescent sensors for reciprocal recognition of mercury (II) and iodide in aqueous solution. Talanta 78 (2009) 364–369.

Transformation Induced Plasticity (TRIP) of SAE 52100 Steel during Martensitic and Bainitic Transformations

Caner Şimşir [iD]
Atilim University, Department of Manufacturing Engineering, Ankara, TURKEY

ABSTRACT

Transformation induced plasticity (TRIP) of SAE 52100 steel during quenching is investigated both experimentally and theoretically. TRIP parameter (K) is determined experimentally for both martensitic and bainitic transformations by using the stressed dilatometry technique. A new method for extraction of for an incomplete transformation is suggested for the martensitic transformation. Theoretical calculations using well-established models for the TRIP effect and the results from the literature are used for the justification of the results of this work. The results for bainitic transformation is found to be in good agreement with both the literature and theoretical calculations using Leblond`s model. On the other hand, experimentally determined value is found to be significantly different from the literature. Nevertheless, it is still in reasonable agreement with the calculations using Leblond`s model.

INTRODUCTION

Transformation Plasticity (TP) or Transformation Induced Plasticity (TRIP) is a significantly increased plasticity during a phase change [1]. TRIP is currently explained by the competition of Greenwood and Johnson [2] and Magee [3] mechanisms depending on thermo-mechanical loading conditions. The extensive review of the TRIP effect can be found elsewhere [4].

Transformation plasticity is an important phenomenon which usually has a strong impact on the predicted distortion and residual stresses by heat treatment simulations. For low quench intensities (small components, low heat extraction rates), TRIP is the sole mechanism leading to distortion of the components [5]. For example, in the work of Acht et al. [6], it is clearly demonstrated that TRIP is the major cause of change in the angle of conicity of gas-nozzle field quenched conical bearing rings made from DIN 100Cr6 steel. Moreover, in many cases, TRIP is also reported to be a good stress relaxation mechanism [7, 8].

Neglecting the TRIP effect might lead to significant errors in heat treatment simulations; in some cases,

even the sign of the stress (tension or compression) cannot be predicted correctly [7]. Moreover, the suggestion of Bhadeshia et al. [8] to design and produce low martensitic transformation temperature steels to reduce welding residual stresses; can be regarded as an efficient way of exploiting the importance of the stress relaxation effect of the TRIP phenomenon.

Owing to its importance in the prediction of heat treatment and welding distortion as well as residual stresses, there exist many models for modeling of the thermomechanical behavior of steels undergoing phase transformations including TRIP effect. Earlier material models in the field [9-12] date back to 1980`s. Although most of these models suggested until now today are usually capable of predicting the TRIP strain accurate enough, the determination of those TRIP model`s parameters is still a challenge [13]. Experimental determination of TRIP model parameters requires stressed dilatometers or physical simulators, which are not widely available. Even in the presence of high-quality equipment, the determination of TRIP model parameters is still a challenging task. The inelastic deformation is quite small and its accurate measurement requires both

careful experimentation and high precision equipment.

In this study, the TRIP constant was determined by using a deformation dilatometer. The results were justified by comparing them with the literature and with the theoretical calculations. The difference between the results of this experimental study and the here presented theoretical calculation is negligible. On the other hand, the differences are considerable when the here presented results are compared to the results of Dalgic et. al. [14] which used a different testing equipment.

THEORY

The Effect of Stress on Phase Transformations

The effect of stress on phase transformation can be summarized in two main parts: first, it changes transformation kinetics and second it causes generation of irreversible permanent strain, namely, transformation plasticity. This second effect can be active even when the material is exposed to stresses that are smaller than the yield strength of the parent phase at a given temperature [15-18].

During thermal treatments, the material is subjected to fluctuating thermal and transformation stresses due to the temperature gradient and phase transformations. These fluctuating stresses can change critical transformation temperatures or phase transformation kinetics. In other words, they may accelerate or retard the transformation of austenite into the product phases.

The effect of stress on transformation kinetics of martensite has been extensively investigated [8, 18-22]. The critical temperature for martensitic transformation, Ms, may vary with the type of stress applied to the material.

Stress state applied on the material can be decomposed into two parts as deviatoric stress and hydrostatic pressure. It is known that positive hydrostatic pressure may lower the Ms, whereas uniaxial stresses increase Ms. Hydrostatic pressure confronts to the transformation dilation of martensite, so Ms is expected to be lowered. On the other hand, an increase of Ms by deviatoric stresses can be explained by the interaction of shear components of global stress state with displacive transformation strains [18, 19, 23, 24].

In the case of diffusional transformations, hydrostatic pressure also retards the transformation by confronting the associated volumetric expansion. On the contrary, transfor-

mation rate is accelerated by uniaxial stresses, which increase the number of nucleation sites by increasing the fraction of internal defects and the free volume needed for diffusional transformations [18, 21, 25, 26].

Transformation Induced Plasticity

Transformation (induced) plasticity (TRIP) is a deformation mechanism that is known to cause a permanent irreversible deformation during a phase transformation. Greenwood and Johnson [2], Magee [3] and later Leblond [11] have developed models for TRIP. In uniaxial loading, the evolution of TRIP strain ($\varepsilon^{tp}(P)$) is often described by the Equation (1):

$$\varepsilon^{tp}(P) = K \cdot \sigma \cdot f(P) \tag{1}$$

Where K is the transformation plasticity parameter, σ is the applied stress, and f(P) is known as the progress of transformation plasticity or scaling function which expresses the dependency of transformation plasticity strain on the fraction transformed (P). Progress of transformation plasticity f(P) must satisfy f(0) = 0 and f(1) = 1. The transformation plasticity strain at the completion of the transformation (P = 1) is referred as the extent of transformation plasticity (ε^{tp}).

Experimental determination of K and f(P) requires stressed dilatometry tests conducted at different stress levels. Independent of f(P), K parameter can be determined by conducting constructing a plot of the extent of TRIP (ε^{tp}) vs. applied stress (σ). The slope of the regression line with a constant intercept of 0 yields the TRIP parameter K. After determination of K, f(P) can be determined from the same experiments by calculating the evolution of TRIP strain according to Equation 2 and determining a phenomenological function that fits all tests reasonably.

$$\varepsilon^{tp}(P) = \varepsilon(\sigma, P) - \varepsilon(\sigma = 0, P) \tag{2}$$

Both K and f(P) can also be treated theoretically according to the theory of micromechanics and phase transformation kinetics. There are different suggestions for f(p), which are reviewed in Fischer et al. [4].

There are several models published in the literature about the calculation of transformation plasticity parameter (K) which can be generalized in the form of Equation (2) [2, 11, 27, 28]:

$$K = C\left(\frac{\Delta V}{V}\right)\left(\frac{1}{\sigma_y^a}\right) \tag{3}$$

Table 1. The chemical composition of SAE 52100 steel used in this study.

	C	Cr	Si	Mn	Al	Cu	Mo	Ni	O	P
wt. (%)	0.99	1.43	0.24	0.36	0.017	0.1	0.02	0.06	5e-5	0.016

Figure 1. Temperature program for the tests for bainitic transformation.
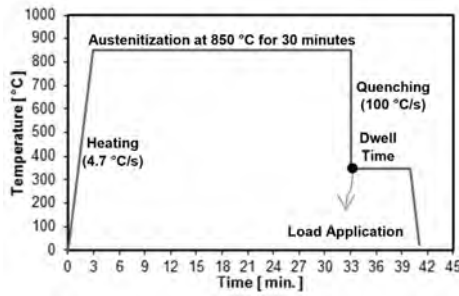

Figure 2. Temperature program for the test for martensitic transformation.

Where, C is a geometrical constant whereas; $\Delta V/V$ and σ_y^a are the dilatation due to phase transformation and the yield strength of the parent phase, respectively. Different models can be obtained by changing multiplier C between 0.66 and 0.83, given in Equation (3).

In order to calculate K with these models, volume change and yield strength of austenite must be known a priori as a function of temperature. Equation (4), which was determined experimentally in a former study [29], is used for the calculation of yield strength of austenite (in MPa).

$$\sigma_y^a(T) = -0.3211T + 294.44; \quad 25^\circ C \leq T \leq 850^\circ C \quad (4)$$

The material is assumed to experience isotropic volume changes during phase transformations and the relative change in volume ($\Delta V/V$) was calculated from the relative length ($\Delta L/L$) change in the dilatometry tests according to Equation 5.

$$\left(\frac{\Delta V}{V}\right) = 3\left(\frac{\Delta L}{L}\right) \qquad (5)$$

EXPERIMENTAL PROCEDURE

The material used in this study was SAE 52100 (DIN/EN 100Cr6, JIS-SUJ2) bearing steel and the chemical composition of this steel is given in Table 1.

The tests are conducted on a thermo-mechanical testing unit (DIL-805 A/D/T, Baehr-Thermoanalysis GmbH) which was used as a stressed dilatometer. The system employs inductive heating, He/N$_2$ gas quenching and it is also capable of applying simultaneously a uniaxial compressive force up to 20 kN. Both thermal and mechanical systems are controlled through a closed-loop control system. The experiments were performed under a vacuum of 5×10^{-4} mbar to prevent oxidation and the specimen is quenched with He gas.

Specimens with lengths of 10 mm and diameters of 5 mm were extracted from 6000 mm long as-cast and rolled 100Cr6 steel rods with a diameter of 37 mm. SAE 52100 steel rods were sliced down to 10 mm long slices. Then, each sli-
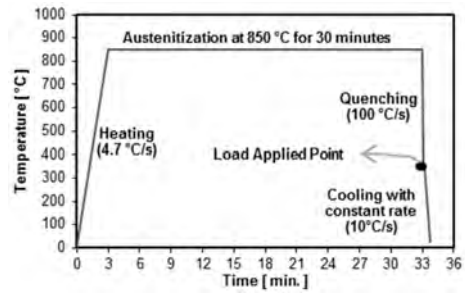
ce was spheroidized in an atmosphere controlled furnace at 790 °C for 14 hours to obtain a homogenous microstructure. After this, specimens are extracted by electrical discharge machining (EDM) from the half radius in order to eliminate the effect of core segregation.

A representative temperature program for the bainitic transformation is presented in Figure 1. First, the specimen is austenitized at 850 °C for 30 minutes and subsequently cooled down from 850 °C to 350 °C at 100 °C/s. Then, a short dwell of 1.5 is imposed for the stabilization of temperature. After this, the specimen was loaded immediately with various compressive stresses (0, 5, 20, 40 and 50 MPa). The stress on specimen was held constant until the end of isothermal dwell until the completion of transformation. It should be noted that the stresses imposed to the specimens were always below the yield strength of austenite at a temperature of 350 °C, which is 178 MPa. Each test is repeated at least 2 times to ensure the reproducibility of the results.

A representative temperature program for TRIP test of martensitic phase transformation is shown in Figure 2. The first step in the temperature program is identical to the TRIP tests of bainitic phase transformation: First, the specimen is austenitized and then cooled down to 350 °C at 100 °C/s at which various compressive stresses are applied. In the next step, the specimen is cooled down to the room temperature (25 °C) at 10 °C/s, while the load on the specimen is held constant during cooling. The stresses imposed on the specimens were always below the yield strength of austenite at temperature of 350 °C. Various compressive loads applied on specimens as 0, 5, 50 and 100 MPa.

In order to investigate the effect of stress on bainitic phase transformation, applied stress and temperature were held constant during the test until phase transformation was completed. Therefore, K can be simply determined independent of the choice of f(P) as f(P) must be 1 at the end of the transformation. On the other hand, the treatment of tests for martensite requires a more complicated treatment: The stressed-dilatometer used in this study cannot be used in subzero temperatures, but the martensitic transformation is not completed at room temperature for this steel as
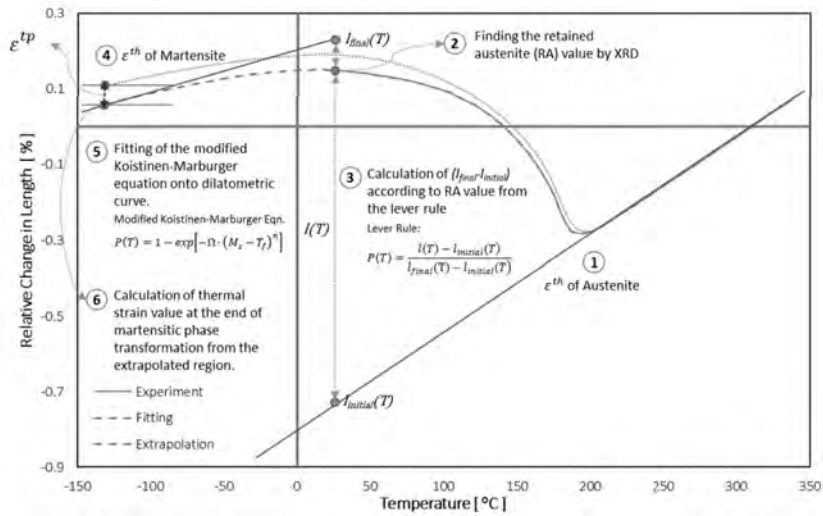
Figure 3. Temperature program for the test for martensitic transformation

its M_f determined as -94 °C in a former study [30]. Hence, the extent of TRIP (ε^{tp}) cannot be directly determined from room temperature tests. Therefore, it is not possible to determine TRIP parameter (K) by from ε^{tp} vs. σ plots.

In this study, a new method is developed to calculate the extent of plasticity from incomplete transformation curves of stressed dilatometer experiments. The method involves the fitting of a kinetic equation for martensitic function to available data and extrapolating the thermal strain of martensite until the completion of transformation. Extrapolated thermal strain for martensite is then used to calculate ε^{tp}. The procedure is summarized in Figure 3.

Modified Koistinen-Marburger equation was selected as the kinetic function

$$P(T) = 1 - \exp\left[-\Omega\left(M_s - T\right)^n\right] \qquad (6)$$

Where P(T) is the proportion of martensite transformed at a given temperature, M_s is the martensite start temperature, Ω is transformation rate constant, n is the under-

cooling exponent. The values for transformation rate constant, Ω, and exponent n are obtained from the former study [30], and M_s is determined as a function of stress. In order to fit the modified equation onto the dilatometric curve, phase fraction of martensite must be known. It can be calculated by applying lever rule on the dilatometric curve, which is given in Equation 7.

$$P(T) = \frac{L(T) - L_{initial}\left(T\right)}{L_{final}\left(T\right) - L_{initial}\left(T\right)} \qquad (7)$$

where, l(T), $l_{initial}$(T) and l_{final}(T) are the thermal strains of austenite-martensite mixture, austenite and martensite, respectively.

Thermal strain of austenite was calculated by fitting line onto austenite region of the dilatation curve. On the other hand, thermal strain for martensite was formerly determined in [30] by subzero quenching experiments and XRD retained austenite measurements.

Finally, modified Koistinen-Marburger equation was fitted onto the dilatometric curve, which had been converted into values of fraction of martensite by the lever rule.
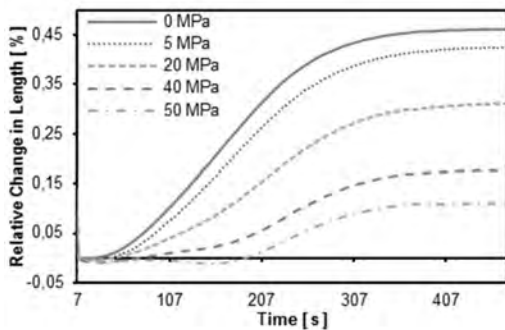
Figure 4. Relative length change vs. Time plot for the tests conducted at different stress levels for the bainitic transformation. Curves clearly indicate the presence of TRIP together with some changes in the transformation kinetics.
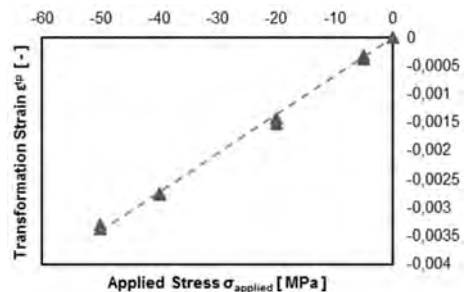

Figure 5. The extent of plasticity (ε^{tp}) vs. applied stress (σ) curve for bainitic transformation at 350°C. Kbainite is determined as 6.82·10-5 MPa-1 from the slope of the regression line.
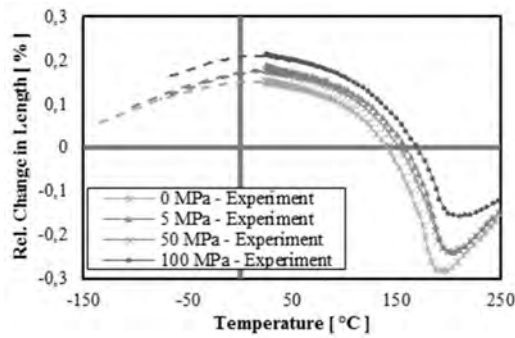
Figure 6. Relative length change vs. Temperature plots and fits Modified Koistinen-Marburger model for the tests conducted at different stress levels for the martensitic transformation. Aside from TRIP, an increase in Ms and Mf temperatures is observed with increasing stress.

Then, martensitic phase transformations were extrapolated up to $P(M_f)=1$ to calculate thermal strain of martensite at the end of transformation, which is the extent of plasticity (ε^{tp}). Calculated ε^{tp} values are used similar to experimentally determined ones to construct a plot to determine the TRIP parameter.

RESULTS AND DISCUSSION

The dilatation curves for the tests conducted for bainitic transformation at 350°C under different compressive stresses are presented in Figure 2. The results show a decrease in the axial strain as the imposed stress increases. As the applied stress is lower than the yield strength of the soft phase, this additional plastic deformation is related to TRIP. The tests also indicate some changes in transformation kinetics but the focus of this study is TRIP and those effects are left out of the scope for the sake of brevity.

The extent of TRIP for bainitic transformation is straightforwardly calculated according to Equation 2 at the end of transformation and plotted against the applied stress in Figure 5. A regression line is fitted to the data and K for bainitic transformation is determined from the slope of the regression line as $6.82 \cdot 10^{-5}$ MPa^{-1}. The result is quite close to the result [28] in the literature for the same steel at the same temperature, which reports K = $7.24 \cdot 10^{-5}$ MPa^{-1}. Theoretical calculation of K according to Leblond model (C=2/3 in Equation 3) yields K = $5.08 \cdot 10^{-5}$ MPa^{-1} which is also reasonably close to experimentally determined value. Thus, it can be concluded that the result lies in line with both the literature and the theory.

The dilatation curves for the tests conducted for martensitic under different compressive stresses are presented in Figure 6. The figure also shows the fitted modified K-M fittings to the experimental data and the extrapolated dilatation curves to the completion of transformation. Similar to results of the bainitic transformation, the presence of TRIP is evident as the dilatation curves shift up as the mag-
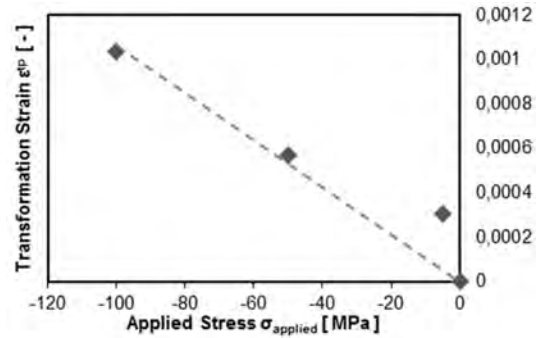

Figure 7. The extent of plasticity (εtp) vs. applied stress (σ) curve for bainitic transformation at 350°C. Kbainite is determined as $6.82 \cdot 10^{-5}$ MPa-1 from the slope of the regression line..

nitude of the applied stress increases, which result in a net difference in length at the end of quenching. Besides TRIP effect, the results also show an increase in M_s temperature as the stress increases, which is also expected according to the theory. Extrapolated curves also indicate the same behavior in M_f again as expected. However, those effects are left out of the scope of this article for the sake of brevity.

Figure 7 presents ε^{tp} vs. σ plot constructed using the ε^{tp} value from the extrapolated curves in Figure 6. The TRIP parameter is determined as $1.06 \cdot 10^{-5}$ MPa^{-1} from the slope, which is considerably smaller than K = $5.42 \cdot 10^{-5}$ MPa^{-1} reported in the literature [28]. On the other hand, a theoretical calculation based on Leblond model yields an average value of K = $1.18 \cdot 10^{-5}$ MPa^{-1} in the transformation range. Despite the large difference with the literature, the experimentally determined value is quite close to the value estimated by Leblond model.

CONCLUSION

In this study, TRIP constant (K) was calculated for bainite and martensite phases of SAE 52100 steel by stressed dilatometry experiments. A new method is suggested for determination of K for martensitic transformation for steel steels having subzero M_f temperature. The results are justified with the literature and the theoretical model of Leblond.

Both experimental and theoretical calculations for bainitic transformation are in good agreement with the literature. On the other hand, for the martensitic transformation, the result is close to the theoretical calculations using the Leblond model but interestingly, it is significantly different from the results from the literature. This might be due to the difference in experimental conditions such as chemical composition of steel used in experiments, austenitization conditions, loading conditions and instruments used or due to the difference in the method used for the numerical analysis of experiment results.

ACKNOWLEDGMENTS

REFERENCES

[1] Fischer, F.D. and S.M. Schlogl, The Influence of Material Anisotropy on Transformation–Induced Plasticity in Steel Subject to Martensitic–Transformation. Mechanics of Materials 21 (1995) 1–23.

[2] Greenwood, G.W. and R.H. Johnson, The deformation of metals under small stresses during phase transformations. Proc. Roy. Soc. 283 (1965) 403–422.

[3] Magee, C.L., Transformation kinetics, micro–plasticity and ageing of martensite in Fe–31Ni, PhD Thesis, Carnegie Inst. of Technology (1966)

[4] Fischer, F.D., Q.P. Sun, and K. Tanaka, Transformation–induced plasticity (TRIP). Applied Mechanics Reviews 49 (1996) 317–364.

[5] Simsir, C., Modeling and Simulation of Steel Heat Treatment: Prediction of Microstructure, Distortion, Residual Stresses and Cracking, in: Dossett JL and Totten GE (Eds.). ASM Metals Handbook Volume 4B – Steel Heat Treating Technologies, ASM International, Materials Park, Ohio–Illinois, pp. 409–466, 2014.

[6] Acht, C., et al., Determination of the material properties for the simulation of through hardening of components made from SAE 52100. – Part 2. Journal of Heat Treatment and Materials (HTM) 64 (2008) 362–371.

[7] Denis, S., Considering stress–phase transformation interactions in the calculation of heat treatment residual stresses. J. Phys. IV France 6 (1996) 159–174.

[8] Bhadeshia, H. and J.W. Christian, Bainite in steels. Metallurgical Transactions A 21, (1990) 767–797.

[9] Sjostrom, S., Interactions and constitutive models for calculating quench stresses in steel. Materials Science and Technology 1 (1984) 823–829.

[10] Leblond, J.B., Mathematical modelling of transformation plasticity in steels II: Coupling with strain hardening phenomena. International Journal of Plasticity 5 (1989) 573–591.

[11] Leblond, J.B., J. Devaux, and J.C. Devaux, Mathematical modelling of transformation plasticity in steels I: Case of ideal–plastic phases. International Journal of Plasticity 5 551–572.

[12] Denis, S., A. Simon, and G. Beck, Modellization of thermomechanical behavior and stress–phase transformation interactions during martensitic tempering of steel and calculation of internal stresses. Memoires et Etudes Scientifiques de la Revue de Metallurgie 81 (1984) 445–445.

[13] Prinz, C., et al., Metallurgical influence on distortion of the case hardening steel 20MnCr5. Materialwissenschaft und Werkstofftechnik 37 (2006) 29–33.

[14] Wolff, M., et al., Some recent developments in modelling of heat–treatment phenomena in steel within the collaborative research centre SFB 570 "Distortion Engineering".

Materialwissenschaft und Werkstofftechnik 43 (2012) 136–142.

[15] Geijselaers, H.J.M., Numerical Simulation of Stresses due to Solid State Transformations. PhD Thesis, University of Twente: Twente (2008)

[16] Denis, S., et al., Stress–Phase transformation interactions – Basic principles ,modeling and calculation of internal stresses. Materials Science and Technology 1 (1984) 805–814.

[17] Denis, S., et al., Influence of stresses on the kinetics of pearlitic transformation during continuous cooling. Acta Metallurgica 35 (1987) 1621–1632.

[18] Aeby Gautier, E., Transformations perlitique et martensitique sous contrainte de traction dans les aciers. PhD Thesis, Ecole des Mines de Nancy (1985)

[19] Patel, J.R. and M. Cohen, Criterion for the action of applied stress in the martensitic transformation. Acta Metallurgica 5 (1953) 531–538.

[20] Videau, J.–C., G. Cailletaud, and A. Pineau, Experimental study of the transformation–induced plasticity in a Cr–Ni–Mo–Al–Ti steel. Le Journal de Physique IV 6 (1996) 465–474.

[21] Simon, A., S. Denis, and E. Gautier, Effet des sollicitations thermomécaniques sur les transformations de phases dans l'état solide. Aspects métallurgique et mécanique. Le Journal de Physique IV 4 (1994) 199–213.

[22] Liu, C.C., K.F. Yao, and Z. Liu, Quantitative research on effects of stresses and strains on bainitic transformation kinetics and transformation plasticity. Materials Science and Technology 16 (2000) 643–647.

[23] Horstemeyer, M.F., Integrated Computational Materials Engineering (ICME) for Metals: Using Multiscale Modeling to Invigorate Engineering Design with Science. 2012: Wiley. 472.

[24] Jacques, P., et al., Multiscale mechanics of TRIP–assisted multiphase steels: I. Characterization and mechanical testing. Acta Materialia 55 (2007) 3681–3693.

[25] Bhattacharyya, S., G. Kehl, and J. Brett, Isothermal transformation of austenite to ferrite and pearlite under externally applied tensile stress. 1955, DTIC Document.

[26] Veaux, M., et al., Bainitic transformation under stress in medium alloyed steels. Journal De Physique IV 11 (2001) 181–188.

[27] Abrassart, F., Influence des transformations martensitiques sur les propriétés mécaniques des alliages du système Fe–Ni–Cr–C. PhD Thesis, Ecole des Mines de Nancy (1972).

[28] Dalgic, M., et al., Transformation plasticity at different phase transformation of a through hardening bearing steel. International Journal of Materials and Properties 3 (2008) 49–64.

[29] Mustak, O., et al. Determination of Flow Curves of Metastable Austenite. in IMMC. 2014. stanbul, Turkey.

[30] Mustak, O., Characterization of SAE 52100 Bearing Steel for Finite Element Simulation of Through–Hardening Process, MSc Thesis, Metallurgical and Materials Engineering Department of, Middle East Technical University (2014).[15] Kulys J, Vidziunaite R. Amperometric biosensors based on recombinant laccases for phenols determination. Biosensors and Bioelectronics 18 (2003) 319–325

Experimental Investigation of Cooling Performance a Heat Pump for Near Azeotropic Refrigerant R404A

Hayati Töre[1] and Ali Kilicarslan[2] (ID)
[1] Municipality of Merzifon, Department of Mechanical Engineer, Amasya, Turkey
[2] Hitit University, Department of Mechanical Engineering, Çorum, Turkey

ABSTRACT

In this study, in order to investigate the effect of outdoor air temperatures on the performance of an air source heat pump, operated in cooling mode, using R404A refrigerant, the heat pump was tested at the outdoor air temperatures ranging from 25 °C to 30 °C and a computer code was also developed by using Engineering Equation Solver (EES). Experimental measurements have been carried out at the outdoor air temperatures ranging from 25 °C to 29 °C and they are repeated three times for better accuracy. The temperatures, the pressures, and the electric energy consumed by the compressor and the fans are measured by means of the K type thermocouple, bourdon type manometer and energy analyzer, respectively. Furthermore, an electric heater was installed in the room where the indoor unit was located and a humidifier is activated to provide the humidity conditions required for the room. The compressor pressure ratio, the power driven by the compressor, the heat rejection capacity of the outdoor unit, the cooling capacity of the indoor unit, the coefficient of performance of the heat pump (COP) were investigated according to different outdoor air temperatures. It was observed that as the outdoor air temperature increased, the indoor unit capacity and COP of the heat pump system decreased while the energy consumed by the compressor increased.

Keywords:
Heat pump, Cooling, Coefficient of performance, R404A

INTRODUCTION

Halogenated refrigerants, which cause the ozone layer to be depleted and affect the global warming, have been used in the vapor compression refrigeration systems for many years. Due to these harmful effects to the environment, some national and international agreements have restricted the use of CFC (chlorofluorocarbons) and HFCF (hydrochlorofluorocarbons), and the protocol to replace these refrigerants with alternative refrigerants is underway.

There are three types of refrigerants that can be used as refrigerant instead of CFC and HCFC class refrigerants. These are called azeotropic, near azeotropic and zeotropic refrigerants [1]. Azeotropic refrigerants act as a single refrigerant at the same temperature and pressure, although these refrigerants are formed by combining two or more refrigerants. In these refrigerants, the compositions of liquid and vapor phases in thermodynamic equilibrium are identical. This means that there is no temperature change during the phase changes under constant pressure, ie during evaporation or condensation phases. Near azeotropic refrigerants are formed by the combination of two or more refrigerants with different boiling points. These refrigerants, which have the same compositions in the liquid and vapor phases, evaporate or condense at different temperatures during the process. Despite the fact that these refrigerants have a higher potential to be developed than the azeotropic refrigerants, the leaks that may be present in the system can cause the composition and properties of the refrigerant to change.

Studies on azeotropic and near azeotropic refrigerants are generally based on energy analysis. The refrigerants are compared in terms of performance in the refrigeration cycle. Studies on exergy analysis are also found in the literature.

Refrigerants R404A and R507A which are alternative to R502 were compared by means a mathematical model developed for vapor compression refrigeration systems using evaporator and condenser temperatures of -50 °C / 0 °C and 40 °C /55 °C, respectively. It has been shown that R507A refrigerant gives better results than R404A refrigerant in systems as the the system performance (COP), exergy destruction and efficiency are taken into consideration[2].

The HFC-161 mixture, similar in physical properties to R502 but environmentally friendly, which could be used as an alternative to the R502 refrigerant, was used as refrigerant in the vapor compression refrigeration system designed for R404A, and as a result of its operation, the pressure ratio of this new refrigerant is about the same as R404A and R502, its COP is higher than R404A at higher evaporator temperatures [3].

The general characteristics and system performances of refrigerants R402A, R402B, R403B, R408A, R404A, R407A and FX40, which may be used as an alternative to R502, have been experimentally investigated and it has been stated that the performances of all the refrigerants except R403B in the refrigeration cycle are very close to R502 [4]. In the another study, the performance of the R22 / R11 mixture with pure refrigerants and the refrigerant mixtures used from the blends of these refrigerants in the vapor compression refrigeration system has been examined [5].

The system parameters were calculated by applying numerical modeling techniques for the ground source heat pump. The computer codes of the equations obtained from the developed model for city of Bolu, Turkey were developed in Matlab program. In order to obtain the properties

of R134A, R404A and R410A, the curve fitting method was used. As a result, it was found that the COP value of R134A was 3.33 in the Matlab program and 3.28 in the Solvent Refrigerant Software program [6]. R449A and R404A were compared to each other in some ways including the compressor discharge temperature, cooling capacity and GWP (Global Warming Potential). It was observed that the refrigeration system using R449A as refrigerant has advantage on the refrigeration system using R404A as GWP and energy are taken into consideration [7].

The performance of air-source heat pump (ASHP) using R404A as refrigerant was investigated both theoretically and experimentally in heating mode at the outdoor temperatures ranging 0 °C and –26 °C. Furthermore, the effect of outdoor air temperature on the compressor capacity, heating capacity and discharge temperature was also investigated. It was observed that the performance of the ASHP with internal heat exchanger (IHX) was better than that of the ASHP without IHX [8].

It is seen from the literature survey that the studies related to the utilization of R404A in heat pump systems are generally based on the investigation of the effect of evaporator or condenser temperature on the performance, pressure ratio or GWP. There is only one study, similar to this study, mentioned above aiming to investigate the effect of outdoor air temperature on the compressor capacity, COP, heating capacity, discharge temperature, but the heat pump is operated in heating mode, not cooling mode.

In this study, the effect of outdoor air temperatures ranging from 25 °C to 30 °C on the performance of single stage vapor compression refrigeration system using R404A refrigerant is investigated both theoretically and experimentally. The experimental results obtained are inserted in the computer code developed by using EES software [9]. As a result, the power consumed by the compressor, the refrigeration capacity of the indoor unit, the heat rejection capacity of the outdoor unit, the coefficient of performance (COP) of the vapor compression refrigeration system are observed with respect to the outdoor air temperature. In addition, some important parameters including the pressure ratio, indoor air temperature in the system are also observed according to the outdoor air temperature.

MATERIAL AND METHOD

The vapor compression refrigeration system used in the experiments consists of compressor, outdoor unit, capillary tube type expansion element, indoor unit, four-way valve, low and high pressure control switch and filter drier. In addition to these, an energy analyzer measuring the amount of energy driven by the compressor and fans, four pressure gauges measuring capillary tube inlet - outlet
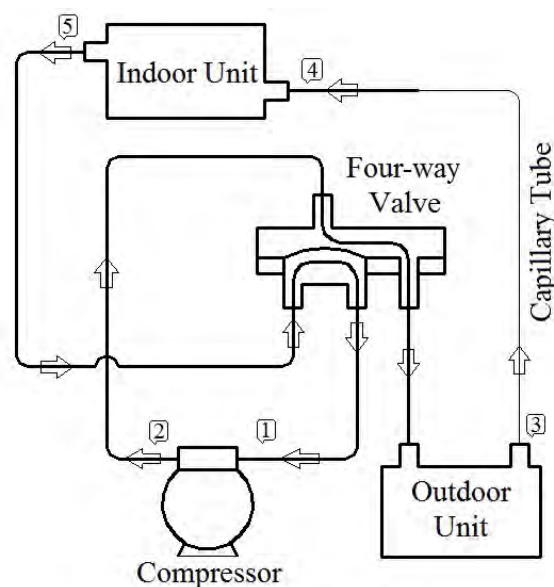
Figure 1. Heat pump cycle in cooling mode

pressures and compressor inlet - outlet pressures, CO-MET MS6D data recorder to record temperature values measured by thermo-couples, electric heater and humidifier, and a humidity meter to measure the humidity in the room are used . The experiments were repeated out three times on August 15-18, 2014 to investigate the effect of outdoor air temperatures ranging from 25 °C to 30 °C on the performance of single stage vapor compression refrigeration system using R404A refrigerant. The heat pump cycle operated in the cooling mode is schematically shown in Fig.1.

The indoor unit, energy analyzer, control panel, humidity meter and data logger are shown in Fig.2.

Figure 2. Indoor unit of the heat pump

The semi-hermetic type compressor, outdoor unit, four-way valve, low and high pressure control switch (presostat) used in the heat pump system are shown in Fig.3.

For the open system, the first law of thermodynamics is expressed as [10],

$$\frac{dE_{c.v.}}{dt} = \sum_i \dot{m}h - \sum_e \dot{m}h + \dot{Q}_{c.v.} - \dot{W}_{c.v.} \qquad (1)$$

In this study, some assumptions were made in thermodynamic analysis;

• The pressure losses in the pipeline between the indoor unit, the outdoor unit and the elements in the refrigeration system have been neglected.

• It is assumed that the heat pump operating in the refrigeration mode and steady-state and steady flow conditions.

• It is also assumed that the electrical power taken by the compressor is converted into the mechanical power.

• Changes in kinetic and potential energies in the heat pump cycle are neglected.

Taking the above considerations into account;
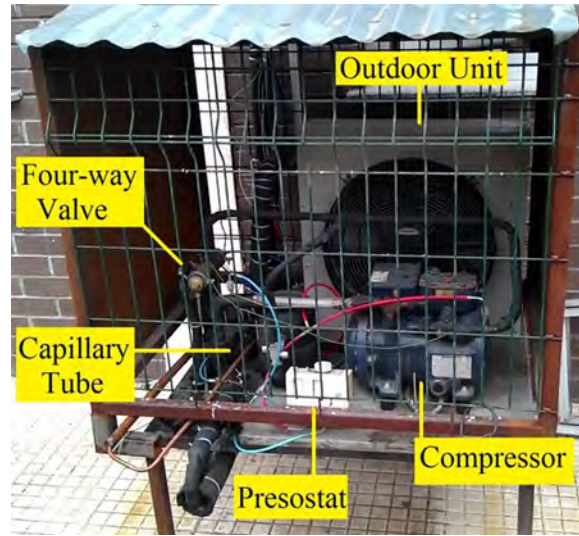
Figure 3. Outdoor unit of the heat pump

Applying the energy equation for steady-state steady flow process (SSSF) to the elements of the heat pump, the following equations are derived for the elements of the heat pump system.

Compressor;

$$\dot{W} = \dot{m}(h_1 - h_2) \qquad (2)$$

Outdoor unit;

$$\dot{Q}_{ou} = \dot{m}(h_4 - h_2) \qquad (3)$$

Indoor unit;

$$\dot{Q}_{iu} = \dot{m}(h_5 - h_4) \qquad (4)$$

Capillary tube;

$$h_3 = h_4 \qquad (5)$$

The coefficient of performance (COP) of the heat pump can be expressed as:

$$COP = \frac{\dot{Q}_{iu}}{\dot{w}_{comp} + \dot{w}_{iu} + \dot{w}_{ou}} \qquad (6)$$

$\dot{W}_{iu}$ and $\dot{W}_{ou}$ are measured by means of energy analyser for constant fan speeds as 0.88 kW.

Uncertainty Analysis of the Experimental Results

The uncertainties of the measurements that are used to calculate the uncertainties associated with $\dot{m}$, $\dot{Q}_{iu}$, $\dot{Q}_{ou}$, $\dot{W}_{comp}$, and COP are ±0.5% for power analyzer, ±1.5 for K type thermocuple and ±3% for manometer. The total uncertainties related to $\dot{m}$, $\dot{Q}_{iu}$, $\dot{Q}_{ou}$, $\dot{W}_{comp}$, and COP are estimated to be 2.03%, 3.03%, 1.74%, 0.45% and 2.99 respectively.

RESULTS AND DISCUSSION

The effect of outdoor air temperature on the performance of vapor compression refrigeration system was experimentally investigated in a heat pump system operated in cooling mode. A computer code was developed for this purpose. In the following section, the results are presented in the figures and discussed in detail.

Figure 4 shows the change of the pressure ratio of the compressor with respect to the outdoor air temperature. Theoretically, when the outdoor air temperature increases, this causes to the indoor air temperature to increase. In this case, more heat will be transferred to the indoor unit and consequently the compressor inlet pressure corresponding to the saturation temperature of the refrigerant in the indoor unit will increase. In addition, as the outdoor air tem-
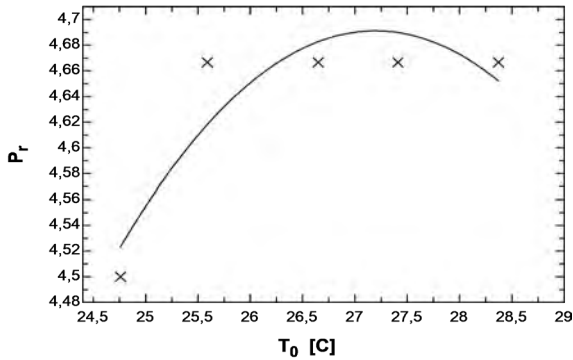
Figure 4. Variation of pressure ratio as a function of outdoor air temperature

perature increases, the temperature difference between the outdoor unit and the surroundings decreases, resulting in a reduction in the amount of heat rejected to the surroundings and in this case the compressor outlet pressure corresponding the saturation temperature of the refrigerant in the outdoor unit will increase. As shown in Fig. 4, the pressure ratio increases due to the relative increase in the outlet pressure to the inlet pressure. At the outdoor temperatures ranging from 24.5 °C to 28.5 °C, the pressure ratio ranges from 4.5 to 4.67. One can conclude from Figure 4 that the pressure ratio has approximately the same value as 4.67 for all the of the outdoor temperatures except the outdoor temperature of 24.75 °C

Figure 5 shows the power consumption of the compressor with respect to the outdoor air temperature. As the outdoor air temperature increases, the pressure ratio of the compressor increases. This increase in pressure ratio of the compressor results in an increase in the power consumed by the compressor. As the outdoor temperatures increases from 24.5 °C to 28.5 °C, the power required by the compressor increases 1.56 kW to 1.63 kW. The maximum compressor power of 1.63 kW is reached as the outdoor temperature is also maximum, namely 28.5 °C
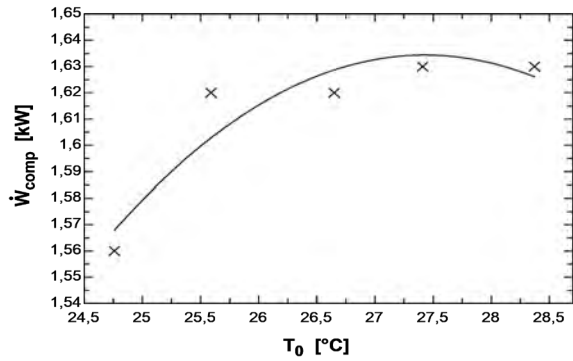
Figure 5. Variation of compressor power consumption as a function of outdoor air temperature

While the average outdoor air temperature for R404A increases by 14.58%, the increase in the pressure ratio is 3.71% while the energy consumption of the compressor is 3.85%.

Figure 6 shows the variation of outdoor unit capacity with respect to outdoor air temperature. As can be seen from Fig. 6, as the outdoor air temperature increases, the heat rejection capacity of the outdoor unit decreases. As the outdoor air temperature increases, the temperature difference between the outdoor unit and the outdoor air decreases, and this cause to the capacity of outdoor unit to decrease. At the outdoor temperatures ranging from 24.5 °C to 28.5 °C, the outdoor unit capacity of heat pump decreased
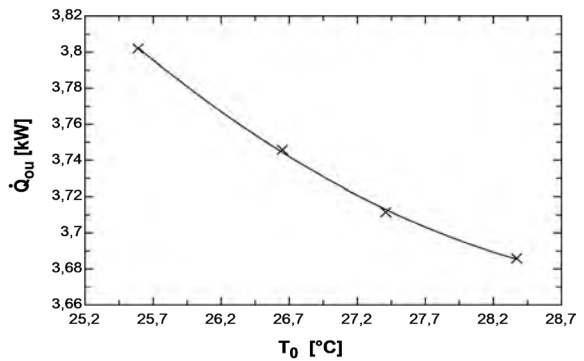
Figure 6. Change of outdoor unit capacity as a function of outdoor air temperature

from 3.80 kW 3.68 kW. It has been found that the outdoor air temperature increases by 10.78% for the R404A refrigerant while the outdoor unit capacity decreases by 5.77% on average.

Figure 7 shows the variation of indoor unit capacity with respect to outdoor air temperature. As the outdoor air temperature increases, the capacity of the indoor unit decreases for R404A refrigerant as shown in Fig.7. At the minimum outdoor temperature of 24.6°C, the indoor unit capacity is 2.14 kW and then it increases sharply to a capacity of

Figure 7. Change of indoor unit capacity as a function of outdoor air temperature

Figure 9. Change of indoor air temperature as a function of outdoor air temperature

2.18 kW, later it decreases smoothly and finally it reaches a minimum capacity of 2.05 kW at a temperature of 28.3 °C When the outdoor air temperature increases, the indoor temperature for R404A increases by 0.26 °C. As a result, there has not been a significant change in indoor unit capacity since there is not much increase in indoor temperature.

Figure 8 shows the change in the coefficient of performance (COP) of the heat pump with respect to the outdoor air temperature. As a measure of performance, the COP is a function of the amount of heat absorbed by the indoor unit and the power drawn by the compressor. In this experimental study, the energy consumed by indoor and outdoor unit fans was taken into account in the determination of COP. The decrease in the indoor unit capacity (Fig.7) and increase in the power drawn by the compressor (Fig.5) caused

Figure 8. Change of refrigeration coefficient as a function of outdoor air temperature

COP to decrease as the outdoor air temperature increased as shown in Figure 8. The COP of the heat pump decreases from 1.23 to 1.13 at the outdoor temperatures between 24.5 °C to 28.5 °C. When Figure 8 is analyzed, the COP of the heat pump using R404A as refrigerant decreases by 1.138 at the outdoor temperatures ranging from 24.5 °C to 28.5 °C.

Figure 9 shows the change of the indoor air temperature with respect to the outdoor air temperature. As the outdoor air temperature increases, more heat will be transferred to the indoor environment, this cause to the indoor air tem-

perature to increase as shown in Fig.9. As the outdoor air temperature increases, the indoor air temperature slightly increases in the heat pump system operated in the cooling mode for refrigerant R404A. As the outdoor air temperature increases by 16.6% on average, the indoor temperature increases by 13.4% on average as it is shown in Figure 9.

CONCLUSION

The effect of outdoor air temperatures ranging from 24.5 °C to 28.5 °C on the performance of heat pump system operated in the cooling code using R404A refrigerant was experimentally performed by using a computer code developed .

The important results obtained from this experimental work can be summarized as follows,

• As the outdoor air temperature increases, there is not much change in the compressor inlet and outlet pressure, but there is a slight increase in the compressor pressure ratio. The pressure ratio of the heat pump system is around 4.5. Along with the increase in the outdoor air temperature, the increase in the pressure ratio of the compressor has been observed to increase. The power required by the compressor increases 1.56 kW to 1.63 kW. The energy consumption of the compressor is 3.85%.

• It was determined that the temperature difference between the outdoor unit and the surroundings decreases and the outdoor unit capacity decreases as the outdoor air temperatur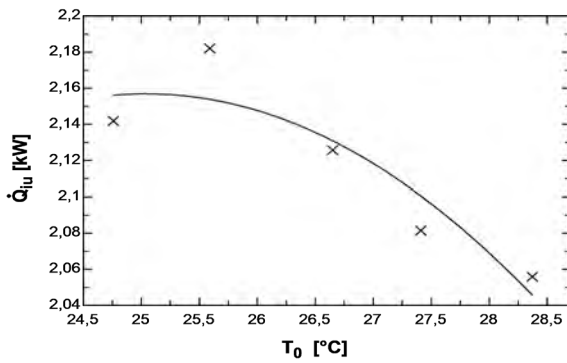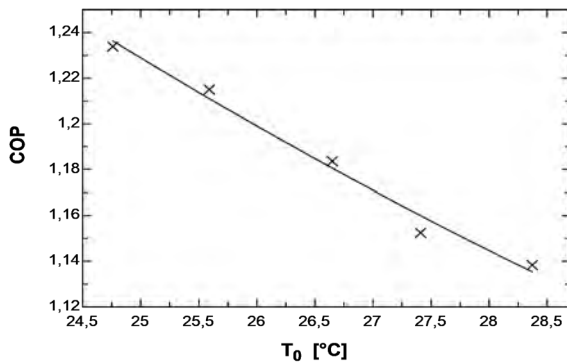e increases. The outdoor unit capacity of heat pump decreases from 3.80 kW 3.68 kW and this corresponds to 5.77% decrease on average in the outdoor unit capacity.

• As the outdoor air temperature increases, the indoor air temperature increases slightly as 0.26°C, this results in a slight increase in the indoor unit capacity. As a result, there is no significant increase in indoor air temperature.

• It was also observed that as the outdoor air tempera-

ture increases, the indoor unit capacity decreases while the energy consumed by the compressor increases, and thereby decreasing the COP of the heat pump system. The COP of the heat pump decreases from 1.23 to 1.13 at the outdoor temperatures between 24.5 °C to 28.5 °C.

• As the outdoor air temperature increases, the increase in the indoor air temperature can be almost neglected.

ACKNOWLEDGMENT

REFERENCES

1. Didion D. A., Bivens D. B., 1990. Role of Refrigerant Mixtures as Alternatives to CFCs, International Journal of Refrigeration, 13(3), 163–175.

2. Arora A., Kaushik S.C., 2008. Theoretical Analysis of a Vapour Compression Refrigeration System with R502, R404A and R507A, International Journal of Refrigeration, 31(6), 998–1005.

3. Xuan Y., Chen G., 2005. Experimental study on HFC–161 mixture as an alternative refrigerant to R502, International Journal of Refrigeration , 28(3), 436–441.

4. Aprea C., Mastrullo R., Rossi F., 1996. Behaviour and Performances of R502 Alternative Working Refrigerants in Refrigerating Plants, International Journal of Refrigeration, 19(4), 257–263..

5. McLinden M.O., Radermacher R., 1987. Methods for Comparing Performance of Pure and Mixed Refrigerants in the Vapour Compression Cycle, International Journal of Refrigeration, 10(6), 318–325.

6. Camdali, U., Bulut, M., Sozbir, N., 2015. Numerical modeling of a ground source heat pump: The Bolu case. Renewable Energy, 83, 352–361.

7. Makhnatch, P., Babiloni, A.M., Rogstam, J., Khodabandeh, R., 2017. Retrofit of lower GWP alternative R449A into an existing R404A indirect supermarket refrigeration system, International Journal of Refrigeration, 76, 184-192.

8. Jin, L., Cao, F., Yang, D., Wang, X., 2016. Performance investigations of an R404A air–source heat pump with an internal heat exchanger for residential heating in northern China, International Journal of Refrigeration, 69, 239-248.

9. Klein, S.A., 2010, Engineering Equation Solver (EES), Professional version V9.723–3D, F–Chart Software.

10. Borgnakke, C., Sonntag, R.E., 2009. Fundamentals of Thermodynamics, Seventh Ed., John Wiley & Sons, Inc.

Synthesis of Chitosan-Based Hydrogels as a Novel Drug Release Device for Wound Healing

Emel Tamahkar[1] ID **and Bengi Özkahraman[2]** ID
[1] Hitit University, Department of Chemical Engineering, Çorum, Turkey
[2] Hitit University, Department of Polymer Engineering, Çorum, Turkey

ABSTRACT

The development of the porous, biocompatible and biodegradable hydrogels has been gaining much attention for wound dressing applications. The hydrogels prepared using freeze-thawing method present important properties of high biocompatibility and non-toxicity. The hydrogels that are able to release drugs for prolonged time are widely used biomaterials for wound healing. In this study chitosan (CS)-based poly-ε-caprolactone (PCL) hydrogels were prepared using poly vinyl alcohol (PVA), poly ethylene glycol (PEG) and poly vinyl pyrrolidone (PVP). PVA-CS-PCL hydrogels only could remain stable at room temperature after synthesis. The properties of the hydrogels were determined with SEM, FTIR, swelling tests and degradation tests. The drugs of ceftazidime (CZ) as an antibiotic and ketoprofen (KP) as an analgesic were loaded onto the hydrogels and the loaded hydrogels were used for the drug release studies at pH 5.5 and pH 7.4. All these results suggest that the developed PVA-CS-PCL hydrogels offer significant potential as a wound dressing material.

Keywords:
Chitosan-based hydrogel, Wound dressing, Drug release, Ceftazidime, Ketoprofen.

INTRODUCTION

The ideal wound dressing material should provide a moist healing environment, a physical and chemical barrier to infection, a painless and effective healing process and a comfortable appliance [1, 2]. Also the wound dressings should prevent dehydration of the wound region and be biocompatible and biodegradable [3]. There has been significant increase in the development of wound dressing materials that deliver drugs to the wound site in a controlled manner [4]. The most important advantage of the sustained release of the drugs to the wound is that it prevents the toxic effects of the therapeutic agents, which is a significant problem of the topical treatment [5, 6]. Recently, there has been reported many research articles about the development of the wound dressings that elute drugs [7-9].

In the last decade, the hydrogels prepared via freeze-thawing method have attracted much interest for their use in biomedical applications such as scaffolds [10], drug delivery [11] and wound dressing material [12, 13]. The major advantages of the freeze-thawing method are the absence of the need of any chemical agent for cross-linking and the initiation of the synthesis. Therefore the hydrogels prepared via freeze-thawing have drawn great attention due to their characteristics of high biocompatibility and non-toxicity [14, 15]. Chitosan (CS) is a cationic natural polymer, which is a derivative of chitin has been extensively utilized with its unique properties since it possesses high biocompatibility, biodegradability, non-toxicity and significant antimicrobial activity [16]. Poly-ε-caprolactone (PCL) has important properties such as non-toxic degradation products, good mechanical stability and cost efficiency [17]. Poly vinyl alcohol (PVA) is one of the widely used polymers due to its excellent biocompatibility, non-toxicity and high biodegradability [18]. Poly ethylene glycol (PEG) and poly vinyl pyrrolidone (PVP) that are highly hydrophilic and biocompatible are the important polymers commonly utilized in various biomedical applications [19, 20]. Polymer blending is an attractive approach that is composed of two or more polymers to provide the development of the novel materials with the desired properties [21, 22].

In this study, for the first time to our knowledge, a novel, environmentally-friendly, biocompatible and biodegradable hydrogel via freeze-thawing was developed containing ceftazidime as an antibiotic and ketoprofen as an analgesic drug. Ketoprofen is a routinely used non-steroidal, anti-inflammatory drug having analgesic function and ceftazidime is an antibiotic drug with

broad spectrum. The chitosan-based hydrogels were prepared with/without the presence of PEG, PVP and PVA. The prepared PVA-CS-PCL hydrogels were chabroad spectrum. The chitosan-based hydrogels were prepared with/without the presence of PEG, PVP and PVA. The prepared PVA-CS-PCL hydrogels were characterized with SEM, FTIR, swelling tests and degradation tests. After drug loading onto the hydrogels, they were applied for drug release studies.

MATERIALS AND METHODS

Materials

Chitosan (CS), poly-ε-caprolactone (PCL), poly vinyl alcohol (PVA), poly ethylene glycol (PEG) and poly vinyl pyrrolidone (PVP) were purchased from Sigma Aldrich. Ceftazidime (CZ) and ketoprofen (KP) were purchased from Sigma–Aldrich with 99.99% purity. All chemicals and reagents were used as received without any further purification. These chemicals and the other reagents were chemically pure grade and the water used in all experiments was Millipore Milli-Q grade. Phosphate and acetate buffers (pH 7.4, pH 5.5) were prepared according to standard methods.

Preparation of PVA-CS-PCL hydrogels

PVA-CS-PCL hydrogels were prepared by freeze-thawing method according to a procedure described elsewhere [23]. Firstly, a polymer mixture was prepared, which consisted of CS (2 g, 2% in 0.2 M acetic acid solution), PVA (0.5 g, 1% aqueous solution), PCL (0.5 g, 1% solution dissolved in dichloromethane) and TWEEN-80 (500 µL) was charged in a 250 mL four-neck round-bottom flask equipped with a mechanical stirrer for about 45 min. The mixture was placed on the petri dish. The blend solution was directly kept frozen at -16 °C for 16 hours. Afterwards, the frozen hydrogels were thawed at room temperature for 8 hours. This process of freezing/thawing was repeated for 8 times. The hydrogels were washed with distilled water to remove the unreacted component, and then air-dried at room temperature.

Swelling and degradation tests

To determine the swelling properties, the dried samples were soaked in pH 5.5 and pH 7.4 buffer solutions at 37°C for 24 h. Then, the excess water was removed and dried to a constant weight. The swelling degree was calculated using the following formula:

$$\text{Swelling degree} = \frac{M_s - M_d}{M_d} \qquad (1)$$

Where M_d and M_s are the masses of dry and swelled samples, respectively.

To evaluate the degradation amounts of the hydrogels, they were placed at pH 5.5 and pH 7.4 buffer solutions for 2 days at 37°C. Then the samples having weight as W_d were removed from the medium, dried and then weighed (W_f). The weight loss was calculated gravimetrically with the following equation:

$$\text{Degradation \%} = \frac{W_d - W_f}{W_d} \times 100 \qquad (2)$$

Characterization of the PVA-CS-PCL hydrogels

The synthesized hydrogels were characterized by FTIR recorded on Thermo Scientific / Nicolet IS10, within the range of 400–4000 cm^{-1}. To study the morphology of the hydrogels, the scanning electron micrographs were recorded by QUANTA FEG 450 scanning electron microscope.

Adsorption studies

CZ and KP were used as antibiotic and analgesic drugs for investigation for drug release of PVA-CS-PCL hydrogels. Dry hydrogels were loaded with one of drug prepared for 48 hours at 50 rpm with a different dose (250-1000 ppm). The loading capacity (mg/g) was calculated using the following equation:

$$\text{Loading capacity} = \frac{C_i - C_e}{W} \times V \qquad (3)$$

Where V is the solution volume (L), W is the mass of sample (g), and C_i and C_e are the initial and equilibrium drug concentrations (mg/L) respectively. The drug concentration was determined using UV/VIS spectrometer (Genesys 10S, ThermoFisher Scientific, USA) at λ_{max} of 258 and 255 nm for CZ and KP, respectively.

In-vitro drug release studies

The in-vitro drug release studies, which were immersed in 10 mL of the drug release medium were performed at pH 7.4 and pH 5.5 at 37°C under magnetic stirring at 50 rpm. At appropriate time intervals, 1 mL of the release medium was collected and subsequently same amount of fresh buffer solution was replaced. The drug concentration was determined using UV/VIS spectrometer (Genesys 10S, ThermoFisher Scientific, USA) at λ_{max} of 258 and 255 nm for CZ and KP, respectively.

Table 1. The stability of the polymers at room temperature prepared via freeze-thawing method

Polymer name	Polymer ratio	Result
PVA-CS-PCL	1:3:1	Stable gels
PVA-CS-PCL	2:3:1	Stable gels
PVA-CS-PCL	3:3:1	Stable gels
CS-PCL	3:1	Unstable gels
PEG-CS-PCL	1:3:1	Unstable gels
PVP-CS-PCL	1:3:1	Unstable gels
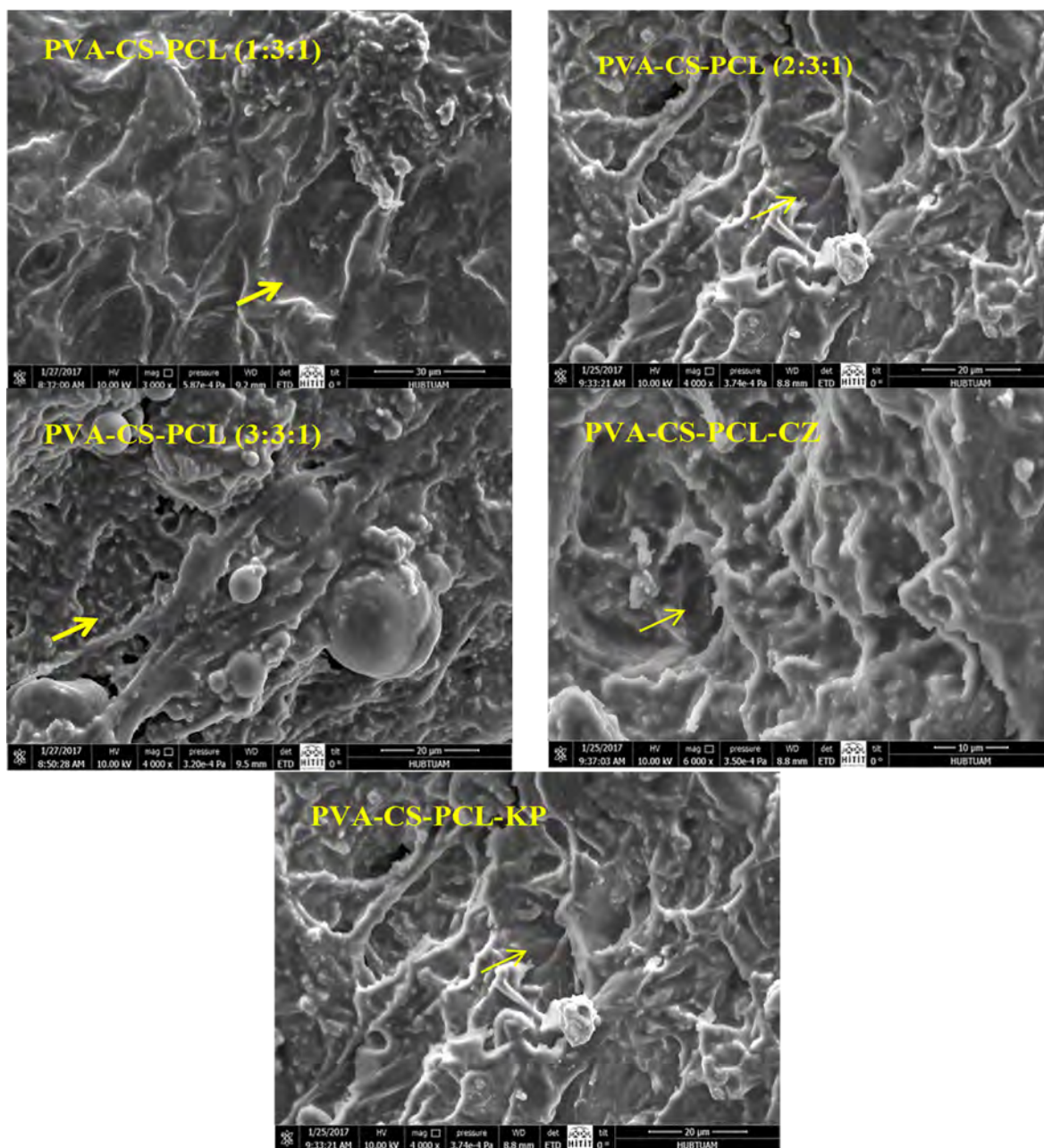
Figure 1. SEM photographs of the PVA-CS-PCL hydrogels with different amounts of PVA, and drug loaded hydrogels.

In-vitro fibroblast response of the hydrogels

MTT assay was performed using L-929 (mouse fibroblast cell line) by direct contact methods as TS-EN 180 10993-5/September 2010 guideline. Briefly, the cells were cultured on 6-well plate at 37°C, 5% CO_2 for 24 h to allow for cell attachment. After incubation, the cultured cells examined by microscopic. The hydrogels were immersed into PBS solution for 48 h according to TS EN ISO 10993-12/April 2013 and the leaching solution was diluted to 0.125 mg/mL. Then, the cells were seeded on 96-well plate at 1×10^4 cells/well and incubated into the leaching solutions for 24 h. Finally, The absorbance was determined using UV spectrophotometer at 570 nm. The cell viability was calculated as the ratio of the mean absorbance of the sample and the mean absorbance of control.

RESULTS AND DISCUSSION

Characterization studies

As can be seen from Table 1, the hydrogels with different compositions were prepared using the same procedure that was explained in detail above. It was observed that CS-PCL, PEG-CS-PCL and PVP-CS-PCL hydrogels were physically unstable gels. However with the incorporation

Table 2. The swelling degree of the polymers, PVA-CS-PCL, PVA-CS-PCL-CZ and PVA-CS-PCL-KP

pH/Polymer	PVA-CS-PCL	PVA-CS-PCL-CZ	PVA-CS-PCL-KP
5.5	7.10	6.05	6.58
7.4	10.04	8.12	8.90

Figure 2. FTIR spectra of PVA-CS-PCL, PVA-CS-PCL-CZ and PVA-CS-PCL-KP hydrogels.

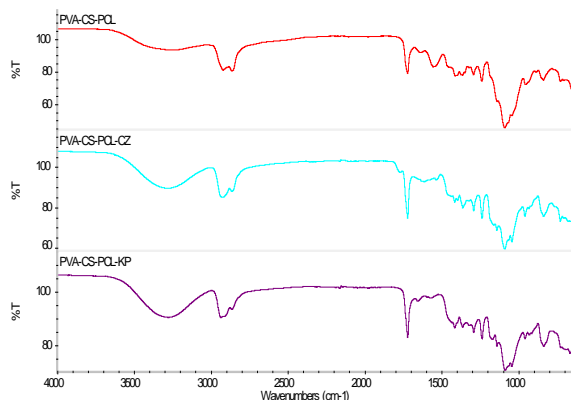of PVA into the structure of CS-PCL hydrogel, the fabrication of the physically stable gels were achieved. All the hydrogels with the composition of PVA-CS-PCL with different PVA ratio were determined to remain stable at room temperature after synthesis. Therefore the stable gels were selected for further characterization studies.

The physically cross-linked hydrogels prepared with freeze/thawing process exhibit highly porous morphological structure with large interconnected pores [14]. This unique characteristic presents important potential especially for drug delivery applications enabling the diffusion of drug molecules through the vehicle material. The morphology of the prepared PVA-CS-PCL hydrogels having different amounts of PVA was demonstrated in Figure 1. The polymers used in this study of PCL, chitosan and PVA were promoted to form a gel via cross-linking during the subsequent freeze/thawing processes. According to SEM micrographs, all the hydrogels showed 3-D network structure and the pores of the hydrogels were shown with arrows indicating high porosity of the hydrogels. Also the dimensions of the macropores of the hydrogels were calculated using ImageJ Software using at least 20 individual pores and obtained as 13.5±3 µm on an average for all hydrogels since the dimensions were evaluated for PVA-CS-PCL (1:3:1), PVA-CS-PCL (2:3:1), PVA-CS-PCL (3:3:1), PVA-CS-PCL-CZ and PVA-CS-PCL-KP as 14.8±7 µm, 16.6±4 µm, 10.8±3 µm, 9.5±2 µm and 15.5±4 µm respectively. It was clearly determined that PVA-CS-PCL (2:3:1) hydrogel exhibited more regular morphology than that of the other hydrogels. However, PVA-CS-PCL (1:3:1) and PVA-CS-PCL (3:3:1) hydrogels involve spherical particles distributed through matrix resulting a heterogeneous nature. The determined amount of PVA in-

corporated into the blend hydrogel improves the dispersion of the PCL and CS phases. Also Figure 1 shows the SEM image of PVA-CS-PCL hydrogel with the drugs loaded into the hydrogel namely PVA-CS-PCL-CZ and PVA-CS-PCL-KP. It was determined that no drug crystals were observed onto the hydrogel structure at the SEM images indicating the compatibility of the drug-polymer-solvent system [24].

The FTIR spectrum analysis was obtained to verify the drug loading throughout the PVA-CS-PCL hydrogels. The FTIR spectra of PVA-CS-PCL hydrogels and drug loaded hydrogels namely; PVA-CS-PCL-CZ and PVA-CS-PCL-KP were demonstrated in Figure 2. It was clearly seen that in the spectrum of drug loaded hydrogels, the new peaks were existed and some of the bands were overlapped when compared with those of the non-medicated hydrogels. The significant increase at characteristic band of O-H stretching absorption of the hydroxyl group (3278 cm-1) was observed indicating the physical interactions between the drug molecules and the hydrogel matrix. PVA-CS-PCL hydrogels bear high content of hydroxyl groups that are accessible to form hydrogen bonds with ceftazidime and ketoprofen molecules. The results confirmed the successful incorporation of the drug molecules in the hydrogel structure [25].

The FTIR spectrum analysis was obtained to verify the drug loading throughout the PVA-CS-PCL hydrogels. The FTIR spectra of PVA-CS-PCL hydrogels and drug loaded hydrogels namely; PVA-CS-PCL-CZ and PVA-CS-PCL-KP were demonstrated in Figure 2. It was clearly seen that in the spectrum of drug loaded hydrogels, the new peaks were existed and some of the bands were overlapped when compared with those of the non-medicated hydrogels. The significant increase at characteristic band of O-H stretching absorption of the hydroxyl group (3278 cm^{-1}) was observed indicating the physical interactions between the drug molecules and the hydrogel matrix. PVA-CS-PCL hydrogels bear high content of hydroxyl groups that are accessible to form hydrogen bonds with ceftazidime and ketoprofen molecules.

Table 3. Hydrolytic degradation of the polymers PVA-CS-PCL, PVA-CS-PCL-CZ and PVA-CS-PCL-KP at different pH values.

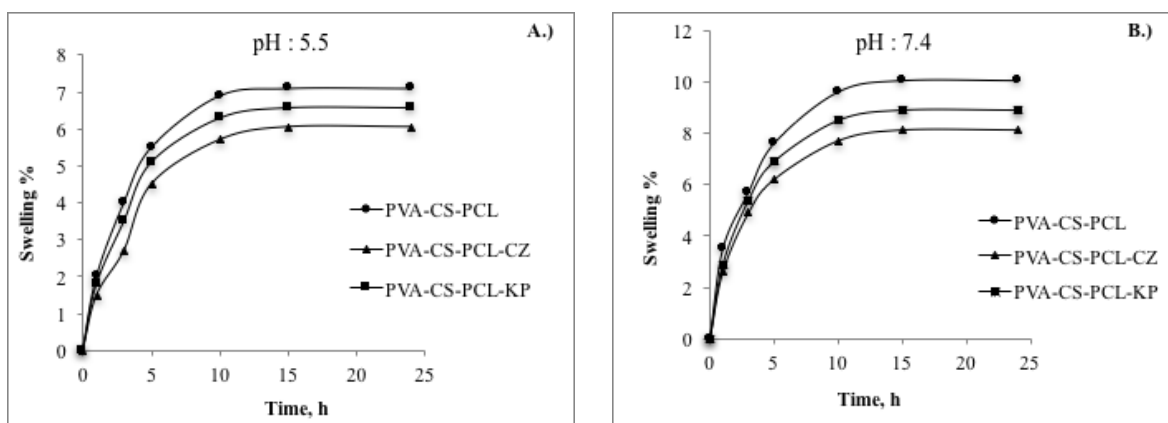| pH 5.5			
	Initial weight, g	Highest weight, g	Weight loss, %
PVA-CS-PCL	0.14	0.50	15.36
PVA-CS-PCL-CZ	0.15	0.39	3.07
PVA-CS-PCL-KP	0.15	0.40	4.27
pH 7.4			
	Initial weight, g	Highest weight, g	Weight loss, %
PVA-CS-PCL	0.15	0.46	13.77
PVA-CS-PCL-CZ	0.16	0.39	2.11
PVA-CS-PCL-KP	0.17	0.38	2.80

Figure 3. The swelling behavior of PVA-CS-PCL, PVA-CS-PCL-CZ and PVA-CS-PCL-KP hydrogels for A.) pH : 5.5 and B.) pH : 7.4.

The results confirmed the successful incorporation of the drug molecules in the hydrogel structure [25].

The swelling degree of the blank and drug-loaded hydrogels was evaluated at different pH values such as pH 5.5 and pH 7.4 and the results were listed in Table 2. The swelling degree of all the hydrogels at pH 7.4 were obtained higher than that of the swelling degree obtained at pH 5.5. It was also determined that the swelling capacity of the drug-loaded hydrogels was lower than that of the blank hydrogel at both pH values due to the interaction of the drug molecules with the polymer chains, which limits the swelling of the hydrogel matrix [26]. It was also found that the swelling capacity of ceftazidime-loaded hydrogels was less than that of ketoprofen-loaded hydrogels, which indicates the more specific interactions of ceftazidime molecules with the polymeric structure could be formed than that of the ketoprofen

In order to evaluate the swelling behavior of the hydrogels better, the swelling degrees were also calculated with respect to time. Figure 3 shows the swelling kinetics of the hydrogels at pH: 5.5 and at pH: 7.4. It was observed that all the hydrogels had similar swelling tendency and swelled rapidly reaching an equilibrium swelling degree within about 10 h for both pH values.

The hydrolytic degradation properties of the blank and drug-loaded hydrogels at different pH values were examined and given in Table 3. Due to the values of the weight loss, the degradation amount of the blank hydrogels was higher than that of the drug-loaded hydrogels at both pH values indicating the presence of the incorporation of the drug molecules into the polymeric matrix [27]. It was determined that the stability of PVA-CS-PCL-CZ hydrogels were higher than that of PVA-CS-PCL-KP hydrogels according to the presence of stronger bonds between ceftazidime molecules and polymer chains than that of ketoprofen molecules and polymeric structure.

Drug loading

Figure 4 demonstrates the loading capacity of the drugs, ceftazidime (CZ) and ketoprofen (KP), onto the PVA-CS-PCL hydrogels. The drug concentration of the loading medium was utilized in the range of 250-1000 ppm. It was determined that the loading capacity of the hydrogels was increased with increasing drug concentration from 250 ppm to 750 ppm. It was obviously defined that the loading capacity was reached a saturation value after 750 ppm. Therefore, this drug concentration was selected to use for the further drug release studies.

Drug release studies

Figure 5 demonstrates the drug release profiles of ceftazidime-loaded and ketoprofen-loaded PVA-CS-PCL hydrogels at pH 5.5 and pH 7.4 simulating the pH value of the dermis and the blood respectively. It was determined that the cumulative release amount of ceftazidime from PVA-CS-PCL-CZ hydrogels at pH 5.5 (90.9 %) was higher than the release amount of the drug at pH 7.4 (67.8 %) since the dissolution amount of the ceftazidime-loaded hydrogels at pH 5.5 was higher than that of at pH 7.4 (Figure 5.A). Figure 5.B shows the cumulative release profiles of the ketoprofen release from PVA-CS-PCL-KP at pH 5.5 and pH 7.4. The cumulative ketoprofen release from PVA-CS-PCL-KP
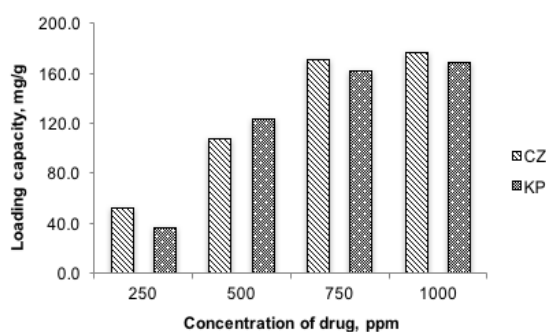

Figure 4. The loading capacity of the drugs, ceftazidime (CZ) and ketoprofen (KP) onto the PVA-CS-PCL hydrogels.

hyrodgels were determined almost same for pH 5.5 and pH 7.4. The in-vitro release of ceftazidime from PVA-CS-PCL-CZ hydrogels presented burst release after 6 h of 63 % and 48 % at pH 5.5 and pH 7.4 respectively. The in-vitro release of ketoprofen from PVA-CS-PCL-KP hydrogels showed burst release of after 6 h of 84 % and 72 % at pH 5.5 and pH 7.4 respectively. The initial burst releases from the drug-loaded hydrogels for the first 6 h may be because of the fast release of the drug molecules that were bound onto the hydrogel matrix by weak interactions [28]. It was also defined that the release profiles of ceftazidime and ketoprofen from drug-loaded hydrogels reached a plateau value after 2 days period. The ceftazidime release properties from PVA-CS-PCL-CZ hydrogels compromise with the degradation chracteristics of the hydrogels since the degradation percentage of these hydrogels was higher at pH 5.5 than that of at pH 7.4. Thus these results indicate that the release of ceftazidime from PVA-CS-PCL-CZ hydrogel matrix was controlled dominantly by the dissolution of the polymeric structure and diffusion of the drug molecules [29, 30]. Shafaghi et al. prepared poly(vinyl acetate-co-maleic anhydride) hydrogels modified with melamine as a drug delivery system using ceftazidime as a model drug. The in-vitro drug release studies showed that after approximately 24 h, the release profile established an equilibrium at pH 3 and 6 with cumulateive release amount of 75% and 80% respectively. It was determined that at pH 8, after 10 h 90% of the drug was delivered indicating a significant burst release [31]. Shefy-Peleg et al. developed gelatin-alginate hydrogels for wound healing with ceftazidime eluting. The cumulative drug release percent form the prepared hydrogels was determined as 50% after 24 h release period indicating a partial release from the matrix [32]. Josef et al. synthesized a novel gelatin hydrogel for ketoprofen delivery. The complete delivery of the drug was occured within 24 h with a cumulative release of 80% [33]. Huang et al. prepared pH-sensitive cationic guar gum/poly acrylic acid hydrogels with different acrylic acid content. The equilibrium release amount of ketoprofen was obtained with the hydrogels having the highest release amount as 99.8% after 10 h [34]. It was clearly seen that the percentage of cumulative release and release time obtained

in this study are comparable with the results reported in the literature. The results also show that prolonged release of the drugs could be achieved using the resultant hydrogels since they serve as an appropriate carrier indicating their stable interactions with drug molecules for wound healing.

In-vitro fibroblast response of PVA-CS-PCL and drug loaded PVA-CS-PCL hydrogels

In order to demonstrate the cytotoxicity of PVA-CS-PCL and drug loaded PVA-CS-PCL hydrogels, L-929 mouse fibroblast cells were utilized to evaluate the biocompatibility of the hydrogels via the incubation of the cells with the leaching solutions extracted from the hydrogels for 24 h. When compared to the control group, the cell viability values of the PVA-CS-PCL and drug loaded PVA-CS-PCL hydrogels were found as 83.1 and 71.0 respectively. The viability value of 70 % is determined as threshold between cytotoxicity and non-cytotoxicity [35]. It was shown that the plain hydrogel namely PVA-CS-PCL has no cytotoxic effects. However the drug loaded PVA-CS-PCL hydrogel that was prepared via the loading of ketoprofen and ceftazidime to the hydrogel matrix has low toxicity to L-929 cells. This may be caused because of presence of the antibiotic drug since it was reported that human fibroblasts were more susceptible to ceftazidime [36]. Due to the results, it was determined that the loading amount of the drugs should be defined to provide safety margin for efficient utilization of the wound dressings.

CONCLUSION

The novel biocompatible and biodegradable hydrogels with high porosity were developed for wound dressing material. PVA-CS-PCL hydrogels could successfully prepared via freeze-thawing method without using any toxic chemical agent and applied for the first time as a drug release system for wound healing. The hydrogels were characterized with FTIR, SEM, swelling and degradation tests. Ceftazidime as an antibiotic and ketoprofen as an analgesic was selected to enhance the wound healing process for controlled drug release from the hydrogel
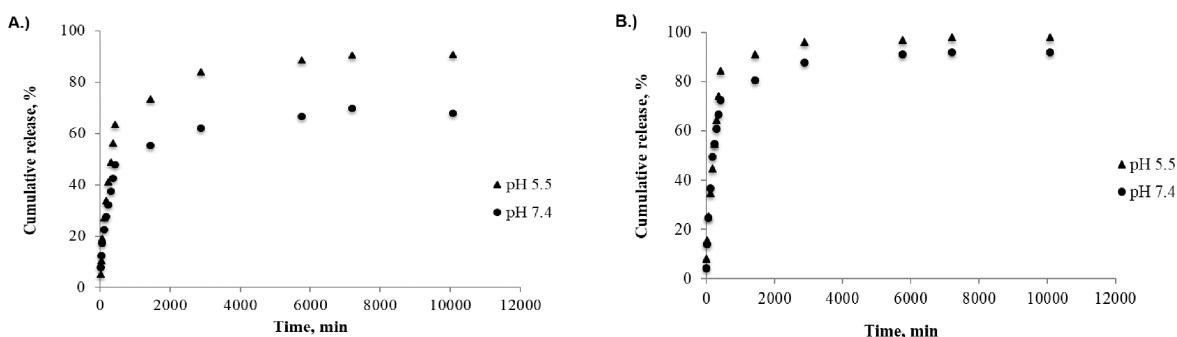
Figure 5. Cumulative release profiles of A.) Ceftazidime, B.) Ketoprofen from the drug-loaded hydrogel matrix.

wound dressing. The in-vitro release of the drugs was exhibited prolonged release for 2 days period. All the results suggest that the prepared drug-loaded PVA-CS-PCL hydrogels present a significant potential as a wound dressing material.

ACKNOWLEDGMENT

REFERENCES

[1] Gupta, B, Agarwal, R, Sarwar Alam, M. Antimicrobial and release study of drug loaded PVA/PEO/CMC wound dressings. Journal of Materials Science: Materials in Medicine 25 (2014) 1613–1622.

[2] Maver, T, Maver, U, Mostegel, F, Griesser, T, Spirk, S, Smrke, DM, Stana–Kleinschek, K. Cellulose based thin films as a platform for drug release studies to mimick wound dressing materials. Cellulose 22 (2015) 749–761.

[3] Zahedi, P, Rezaeian, I, Ranaei–Siadat, S–O, Jafari, S–H, Supaphol, P. A review on wound dressings with an emphasis on electrospun nanofibrous polymeric bandages. Polymers for Advanced Technologies 21 (2010) 77–95.

[4] Kevadiya, BD, Rajkumar, S, Bajaj, HC, Chettiar, SS, Gosai, K, Brahmbhatt, H, Bhatt, AS, Barvaliya, YK, Dave, GS, Kothari, RK. Biodegradable gelatin-ciprofloxacin-montmorillonite composite hydrogels for controlled drug release and wound dressing application. Colloids and Surfaces B: Biointerfaces 122 (2014) 175–183.

[5] Thakur, RA, Florek, CA, Kohn, J, Michniak, BB. Electrospun nanofibrous polymeric scaffold with targeted drug release profiles for potential application as wound dressing. International Journal of Pharmaceutics 364 (2008) 87–93.

[6] Zilberman, M, Egozi, D, Shemesh, M, Keren, A, Mazor, E, Baranes–Zeevi, M, Goldstein, N, Berdicevsky, I, Gilhar, A, Ullmann, Y. Hybrid wound dressings with controlled release of antibiotics: Structure–release profile effects and in vivo study in a guinea pig burn model. Acta Biomaterialia 22 (2015) 155–163.

[7] Boateng, JS, Pawar, HV, Tetteh, J. Polyox and carrageenan based composite film dressing containing anti–microbial and anti–inflammatory drugs for effective wound healing. International Journal of Pharmaceutics 441 (2013) 181–191.

[8] Safdari, M, Shakiba, E, Kiaie, SH, Fattahi, A. Preparation and characterization of ceftazidime loaded electrospun silk fibroin/gelatin mat for wound dressing. Fibers and Polymers 17 (2016) 744–750.

[9] Yu, H, Xiao, C. Synthesis and properties of novel hydrogels from oxidized konjac glucomannan crosslinked gelatin for in vitro drug delivery. Carbohydrate Polymers 72 (2008) 479–489.

[10] Guan, Y, Bian, J, Peng, F, Zhang, X–M, Sun, R–C. High strength of hemicelluloses based hydrogels by freeze/thaw technique. Carbohydrate Polymers 101 (2014) 272–280.

[11] Behnoodfar, D, Dadbin, S, Frounchi, M. PLA microspheres–embedded PVA hydrogels prepared by gamma–irradiation and freeze–thaw methods as drug release carriers. International Journal of Polymeric Materials and Polymeric Biomaterials 62 (2013) 28–33.

[12] Gonzalez, JS, Ludueña, LN, Ponce, A, Alvarez, VA. Poly(vinyl alcohol)/cellulose nanowhiskers nanocomposite hydrogels for potential wound dressings. Materials Science and Engineering: C 34 (2014) 54–61.

[13] Kamoun, EA, Kenawy, E–RS, Tamer, TM, El–Meligy, MA, Mohy Eldin, MS. Poly (vinyl alcohol)–alginate physically crosslinked hydrogel membranes for wound dressing applications: Characterization and bio–evaluation. Arabian Journal of Chemistry 8 (2015) 38–47.

[14] Tamahkar, E, Özkahraman, B. Potential evaluation of PVA–based hydrogels for biomedical applications. Hittite Journal of Science and Engineering 2 (2015) 165–171.

[15] Hassan, CM, Peppas, NA, Secondary Structure and applications of poly(vinyl alcohol) hydrogels produced by conventional crosslinking or by freezing/thawing methods. In Biopolymers · PVA hydrogels, anionic polymerisation nanocomposites, Springer Berlin Heidelberg, Berlin, Heidelberg, 2000.

[16] Dai, T, Tanaka, M, Huang, Y–Y, Hamblin, MR. Chitosan preparations for wounds and burns: Antimicrobial and wound–healing effects. Expert review of anti–infective therapy 9 (2011) 857–879.

[17] Thomas, R, Soumya, KR, Mathew, J, Radhakrishnan, EK. Electrospun polycaprolactone membrane incorporated with biosynthesized silver nanoparticles as effective wound dressing material. Applied Biochemistry and Biotechnology 176 (2015) 2213–2224.

[18] Kamoun, EA, Kenawy, E–RS, Chen, X. A review on polymeric hydrogel membranes for wound dressing applications: PVA–based hydrogel dressings. Journal of Advanced Research 8 (2017) 217–233.

[19] Ahmed, AS, Mandal, UK, Taher, M, Susanti, D, Jaffri, JM. PVA–PEG physically cross–linked hydrogel film as a wound dressing: Experimental design and optimization. Pharmaceutical Development and Technology (2017) 1–25.

[20] Dai, X–Y, Nie, W, Wang, Y–C, Shen, Y, Li, Y, Gan, S–J. Electrospun emodin polyvinylpyrrolidone blended nanofibrous membrane: A novel medicated biomaterial for drug delivery and accelerated wound healing. Journal of Materials Science: Materials in Medicine 23 (2012) 2709–2716.

[21] Doulabi, HA, Mequanint, K, Mohammadi, H. Blends and nanocomposite biomaterials for articular cartilage tissue engineering. Materials 7 (2014)

[22] Islam, A, Yasin, T, Gull, N, Khan, SM, Munawar, MA, Shafiq, M, Sabir, A, Jamil, T. Evaluation of selected properties of biocompatible chitosan/poly(vinyl alcohol) blends. International Journal of Biological Macromolecules 82 (2016) 551–556.

[23] Afshari, MJ, Sheikh, N, Afarideh, H. PVA/CM–chitosan/honey hydrogels prepared by using the combined technique of irradiation followed by freeze–thawing. Radiation Physics and Chemistry 113 (2015) 28–35.

[24] Jannesari, M, Varshosaz, J, Morshed, M, Zamani, M. Composite poly (vinyl alcohol)/poly (vinyl acetate) electrospun nanofibrous mats as a novel wound dressing matrix for controlled release of drugs. Int J Nanomedicine 6 (2011) 993–1003.

[25] Hsu, Y–H, Lin, C–T, Yu, Y–H, Chou, Y–C, Liu, S–J, Chan, E–C. Dual delivery of active antibactericidal agents and bone

morphogenetic protein at sustainable high concentrations using biodegradable sheath-core-structured drug-eluting nanofibers. International Journal of Nanomedicine 11 (2016) 3927–3937.

[26] Kataria, K, Gupta, A, Rath, G, Mathur, RB, Dhakate, SR. In vivo wound healing performance of drug loaded electrospun composite nanofibers transdermal patch. International Journal of Pharmaceutics 469 (2014) 102–110.

[27] Atzet, S, Curtin, S, Trinh, P, Bryant, S, Ratner, B. Degradable poly(2-hydroxyethyl methacrylate)-co-polycaprolactone hydrogels for tissue engineering scaffolds. Biomacromolecules 9 (2008) 3370–3377.

[28] Jeong, B, Bae, YH, Kim, SW. Drug release from biodegradable injectable thermosensitive hydrogel of PEG-PLGA-PEG triblock copolymers. Journal of Controlled Release 63 (2000) 155–163.

[29] Freiberg, S, Zhu, XX. Polymer microspheres for controlled drug release. International Journal of Pharmaceutics 282 (2004) 1–18.

[30] Kamaly, N, Yameen, B, Wu, J, Farokhzad, OC. Degradable controlled-release polymers and polymeric nanoparticles: Mechanisms of controlling drug release. Chemical Reviews 116 (2016) 2602–2663.

[31] Shafaghi, S, Moghadam, PN, Fareghi, AR, Baradarani, MM. Synthesis and characterization of a drug-delivery system based on melamine-modified poly(vinyl acetate-co-maleic anhydride) hydrogel. Journal of Applied Polymer Science 131 (2014).

[32] Shefy-Peleg, A, Foox, M, Cohen, B, Zilberman, M. Novel antibiotic-eluting gelatin-alginate soft tissue adhesives for various wound closing applications. International Journal of Polymeric Materials and Polymeric Biomaterials 63 (2014) 699–707.

[33] Josef, E, Zilberman, M, Bianco-Peled, H. Composite alginate hydrogels: An innovative approach for the controlled release of hydrophobic drugs. Acta Biomaterialia 6 (2010) 4642–4649.

[34] Huang, Y, Yu, H, Xiao, C. Ph-sensitive cationic guar gum/ poly (acrylic acid) polyelectrolyte hydrogels: Swelling and in vitro drug release. Carbohydrate Polymers 69 (2007) 774–783.

[35] Hiep, NT, Khon, HC, Niem, VVT, Toi, VV, Ngoc Quyen, T, Hai, ND, Ngoc Tuan Anh, M. Microwave-assisted synthesis of chitosan/polyvinyl alcohol silver nanoparticles gel for wound dressing applications. International Journal of Polymer Science 2016 (2016) 11.

[36] Elsner, JJ, Berdicevsky, I, Zilberman, M. In vitro microbial inhibition and cellular response to novel biodegradable composite wound dressings with controlled release of antibiotics. Acta Biomaterialia 7 (2011) 325–336.

Analysis of Scoring Resistance on Coated Spur Gears by Considering Surface Roughness

Mert Safak Tunalioglu[1] and **Nihat Gemalmayan[2]**

[1] Hitit University, Department of Mechanical Engineering, Çorum, Turkey
[2] Gazi University, Department of Mechanical Engineering, Ankara, Turkey

ABSTRACT

With the rise of velocity and momentum in machines as a result of technological developments, on gears, alongside refraction from the bottom of the gears and pitting formation, and scoring formation has showed up. In the scoring formation phase because of the fact that many parameters are influential, resistance calculations could not be stated precisely. In experiments made for this purpose, 20MnCr5 steel gears were coated using various coating materials (chrome, nickel and manganese), thus usage of coating material on gear mechanisms in terms of scoring was analyzed. In the experiments, gears were rotated with a speed of 3000 rpm and the oil temperature constant at 323±2 °K. Gears were exposed to loading at 15.2 Nm and continued by increasing 20 % until scoring formation was observed. It is seen in the experiments that coated gears have more scoring resistance than uncoated ones. It is also observed that coating materials increases the scoring strength of gears. According to the experiments, when gears run at the same conditions (speed, torque and lubrication), chrome coated gears are 10 times longer, nickel coated gears are 5 times and manganese coated gears are 1.5 times longer resisted when compared with uncoated gears. After the scoring formation, experiments continued for determining how the scoring formation developed. It is seen in the experiments that when scoring occurs the wear increases rapidly on the tooth of gears.

Keywords:
Scoring, Spur gear, Surface roughness, Coating material, Pitting.

INTRODUCTION

Gears are often used as power and motion transmission elements in the automotive industry. The ability of the gears to operate comfortably at high power and speed depends on determining the factors causing the wear and obtaining the appropriate conditions. Scoring is a case of rapid separation of little particles which are adhered to each other by metallic contact from gear surface in gear systems that work simultaneously [1]. There are many ways to prevent scoring (profile correction, use of coating materials, lubrication, etc.). Coating materials are made for increasing the wear resistance of the material, preventing the discontinuity on metals (scratches, pores) and gaining functional quality [2]. The facing of gears by coating materials is a usual improvement of strength method

Theoretical and experimental studies have been carried out to observe the formation of scoring on the gears. In theoretical studies some methods have been presented by Authors for the calculating of scoring. These methods are based on pressure or surface temperature on tooth profile when the gears are in action [3-14]. In experimental works, the closed circuit power circulating gear wear test mechanism (FZG) is used to investigate the strength of gears as a result of rapid wear [2,15-24]. Work to prevent scoring formation is generally in the form of profile modification [15-19] and coating the tooth surfaces with the coating materials [20-24]. The studies that profile modification on gears are indicates that; (+) profile modification is higher scoring resistance than (-) profile modification. Also the bigger profile modification ratio is the more wear it causes. The studies that using coating materials on gears are indicates that; coating materials increase the wear resistance and strength by decreasing surface toughness. All

Table 1. The Properties of Test Gears

Quantity	Symbol	Unit	Value
Number of teeth	z_1 z_2	- -	17 41
Module	m	mm	3
Tooth width	b	mm	20
Pressure angle	a_o	°	20
Pitch diameter	d_{o1} d_{o2}	mm mm	51 123
Addendum diameter	d_{b1} d_{b2}	mm mm	57 129
Dedendum diameter	d_{t1} d_{t2}	mm mm	43,8 115,8
Distance between the axis	a	mm	87
Contact ratio	e	-	1,86
Hardness	HB	-	170-220

Table 2. Abbreviated for test gears

Uncoated	K
Manganese	M
Nickel	N
Chrome	C

Table 3. The physical properties of the lubricant

SAE Number	80W/90
Density g/ml (15 °C)	0,906
Viscosity (40 °C)	200
Viscosity (100 °C)	17,5-18,5
Viscosity Index	95
Flaming Point °C	220
Flash Point °C	-27

works based on to find critical scoring load and to prevent scoring. The Authors didn't give any information what happens after scoring formation.

In order to determine scoring formation: (1) being appropriate to DIN 51354 [25], weight lost as a result of sudden wear in gears, (2) to observe pinion surface in coupling was 20% of the scoring amount in active profile were the methods used.

The aim of this study is to find the critical scoring load by using a new method, sudden change in surface roughness on gear surfaces. Another aim is examining what kind of development happens after scoring formation.

Experimental Study
Test Gears
Gears used in the experiments are 20MnCr5 steel and their hardnesses are between 170-220 HB. Data about gears are given in the table below. In Table 1 subscript 1
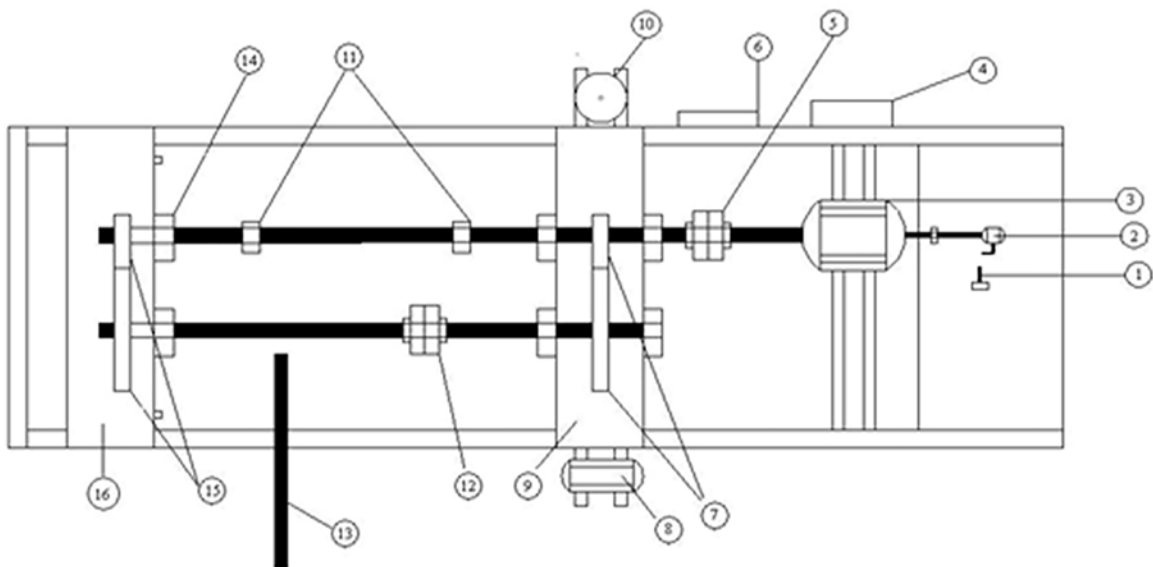
1. Counter 2. Reductor 3. D.C. motor 4. Power control unit 5. Coupling 6. Heating-cooling system control unit 7. Power transmission gears 8. Water transmission D.C. motor 9. Power transmission gearbox 10. Water can 11. Plain bearings 12. Torque coupling 13. Loading bar 14. Plain bearing 15. Test gears 16. Test gearbox

Figure 1. The power circulating gear wear test rig

Table 4. Loading steps of experiments done for finding scoring load

Test Number	Force (N)	Torsion M_i (Nm)
1	15,2	15,2
2	18,8	18,8
3	21,9	21,9
4	26,3	26,3
5	31,6	31,6
6	37,7	37,7
7	45,5	45,5
8	54,6	54,6
9	65,5	65,5
10	78,6	78,6
11	94,3	94,3
12	113,1	113,1
13	135,8	135,8
14	162,9	162,9
15	195,5	195,5
16	234,6	234,6
17	281,6	281,6
18	337,9	337,9

shows the pinion and subscript 2 shows the gear.

In the experiments gears were coated by chrome, nickel and manganese. For practical use, coated gears are abbreviated in Table 2.

An immersion type lubrication system was used. The physical properties of the lubricant which is used in the experiments are given in Table 3.

Experimental Conditions

FZG (Forschungsstelle für Zahrender und Getriebebau) system, which was developed in Germany in which wear and fatigue experiments made has been used in the experiments. [1,2,17]. Closed circuit power circulating gear wear test mechanism is used to investigate the scoring strength of the gears as result of rapid wear (Figure 1).

In the experiments, gears were rotated with a speed of 3000 rpm and the oil temperature constant at 323±2 °K as appropriate to the literature [3,4,7]. Gears were exposed to loading at 15.2 Nm and continued by increasing 20 % until scoring formation was observed. Before the experiments hardness, surface roughness and weight of the gears were measured. Between every stage of the experiment, surface roughness and weight measurements were repeated. When values of weight showed a sudden increase, the scoring formation was examined by controlling the surface of the tooth [2,3]. In case there was not a sudden change in weighing, adding weight was continued. The experiment setup was a type that enables loading when motionless. Loading to the spindle that has torque coupling and connected to the testing gears was done by hanging weight with the help of moment handle. As a result of tightening cap screws on the torque coupling, closed circuit was completed. Loading steps of the experiments done for determining critical scoring load are given in Table 4.

In the experiment of weight loses method was used for determination of the scoring load, gears were burdened gradually and were run for 20 minutes. In between every stage, pinion and gear were weighted. The stage that wear increased suddenly gave critical scoring load [3,4,25]. For measuring weight loss, a sensitivity scale at sensitiveness of 0.1 mgr was used. For proof of the accuracy of experiments, it was examined if pinion surface in coupling was 20% of the scoring amount in active profile [3,4].

In the method of measurement of surface roughness, after completing coating of the gears, surface roughness was examined till scoring formation. Surface roughness was measured with the Taylor Hubson 3+ Surface Roughness Measurement Apparatus. In the measurements, mean surface roughness (Ra) and maximum point in the profile (Ry) were tried to be determined.

Experimental Results
Relation Between Weight Lost in Gears and Scoring

Being appropriate to DIN 51354, gears were burdened gradually, after every stage the pinion and gear were weighted. The stage that wear increased suddenly was defined as the critical scoring load. It is enough to take measurements from the pinion to observe the formation of the scoring. Since the system has a rate of 2.41, the pinion enters about 2.5 times more than the large gear
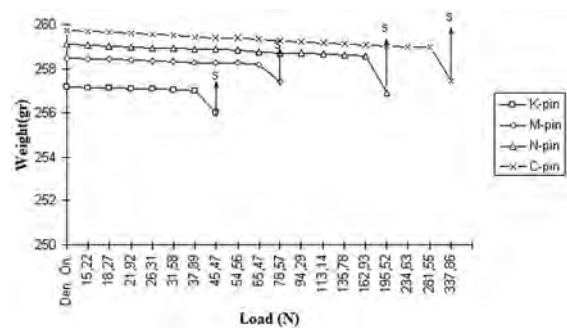

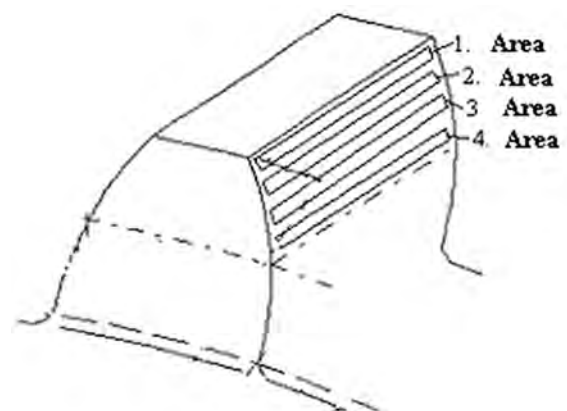**Figure 2.** The changing of weight in the pinion to determine the critical scoring load

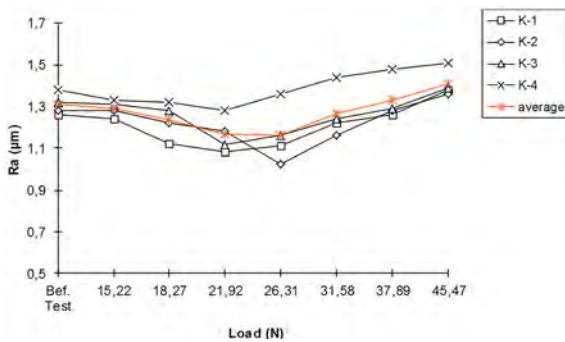**Figure 3.** Areas that roughness measured

147

Figure 4. The average of mean surface roughness on uncoated pinion gear.
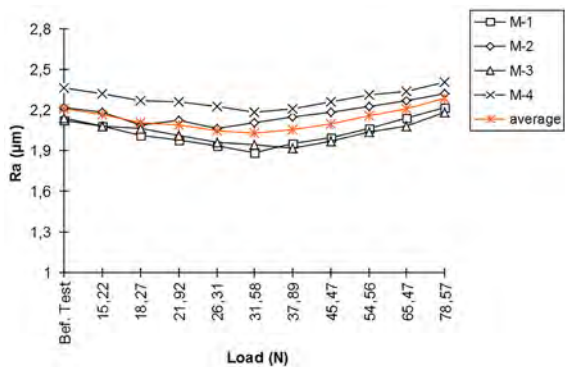

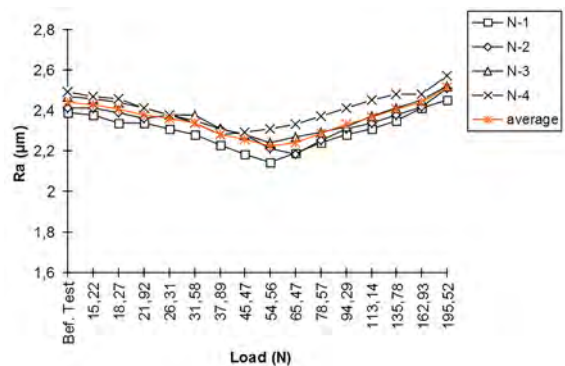**Figure 5.** The average of mean surface roughness on manganese coated pinion gear.

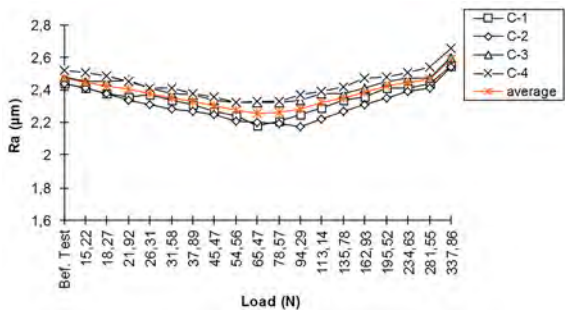**Figure 6.** The average of mean surface roughness on nickel coated pinion gear.

Figure 7. The average of mean surface roughness on chrome coated pinion gear.

ratio. Hence, wear is observed earlier in the pinion gear [1-3].

Results emerged after experiments were treated for every gear one by one. Weight graphic that occurred as a result of sudden increase of corrosion was given in Figure 2.

According to Figure 2, corrosion is seen in K, M, N and C, respectively. In the Figure, 's' shows the moment that scoring started. To Figure 2, while 7th stage of the experiment scoring on uncoated gear is observed, in manganese coated gear in 10th stage, in nickel coated gear in 15th stage and in chrome coated gear in 18th stage of the experiment sudden increase falling occurs. If a comparison is made after the experiments, usage of chrome-coated gear is more advantageous.

Effect of Surface Roughness to Scoring

For determining surface roughness, 4 different points were measured and then their averages were given in graphics. Because the fact that, during the same study, pinion coupling much more than gear, measuring only pinion is adequate. And the reason that surface was taken from rolling round to head of tooth is scoring was initially determined in these parts [1,2].

When surface roughness on uncoated gear was examined, it was observed that roughness decreased till 3rd load stage, then increased in certain proportion and in 7th stage got scoring by suddenly increasing.

According to Figure 4, the average of mean surface roughness of 4 areas is between other surface roughness values.

If the average surface roughness of the gears is examined (Figure 4-7); it is seen that in the course of production and because of the coatings resulted from coating materials at the load of starting to run roughness on surfaces of gears decreased to certain stage, until scoring formation it increased with a certain speed and at scoring formation roughness on their surfaces suddenly increased.

When the values of the maximum point in gears profile were examined, results parallel to the average surface roughness come into the picture. In Figure 8-11 if a comparison is made after the experiments, usage of chrome-coated gear is more advantageous.

Development of Scoring

After determination of scoring load experiments, experiments were continued on the gears that scoring occurred and following results were obtained. Gears were exposed to loading at 300Nm, were rotated with speed of 3000
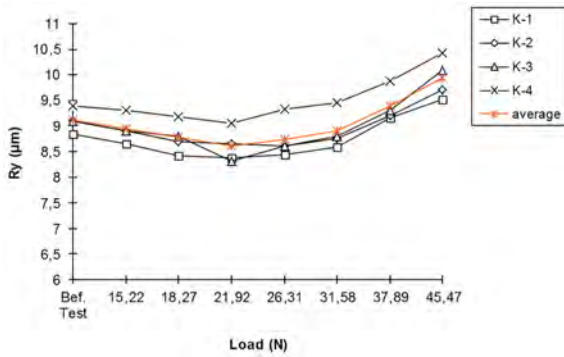
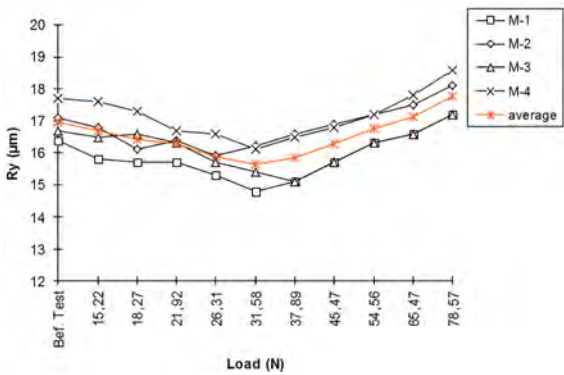**Figure 8.** The average of maximum point in the profile on uncoated pinion gear.

Figure 9. The average of maximum point in the profile on manganese coated pinion gear.
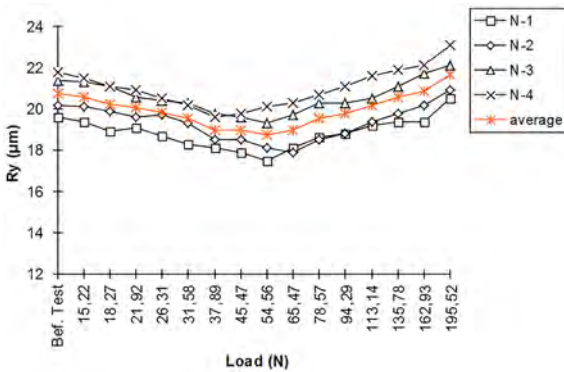
Figure 10. The average of maximum point in the profile on nickel coated pinion gear.
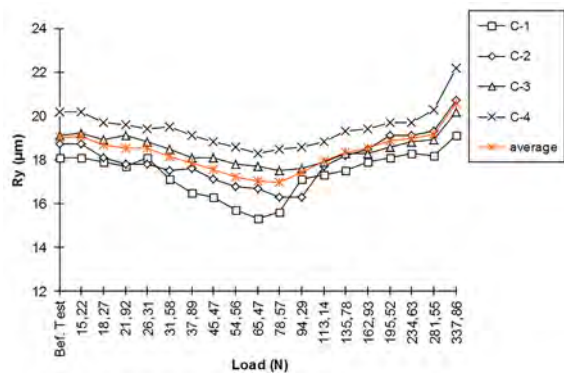
Figure 11. The average of maximum point in the profile on chrome coated pinion gear.
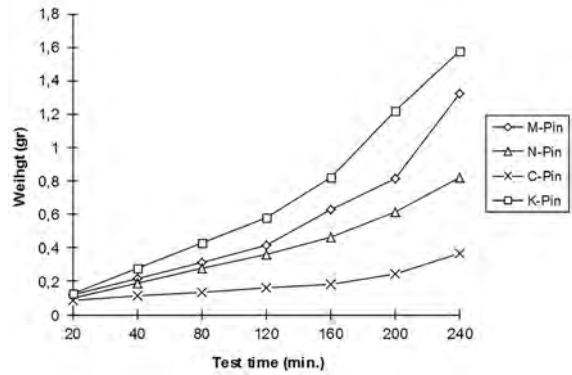
Figure 12. The changing of weight on pinion after scoring occurs

rpm. The temperature was constant at 323±2 °K.

As it is seen in the Figure 12, wear and thus scoring showed quick increase on pinion that load was excessive.

Results and Conclusion

In this study, scoring load that occurs as a result of rapid wear on gears coated with different coating materials was determined by considering surface roughness.

After the experiments for determination of critical scoring load on gears, at the same heat, speed and lubrication conditions, critical scoring load emerged in every gear was found as 45,47 N in uncoated gear, 78,57 N in manganese coated gear, 195,52 N in the nickel coated gear and 337,86 N in the chrome coated gear. According to these values, use of coating material on gears is advantageous in terms of scoring formation. The chrome coated gear run at 11 different loading stage 220 minutes more than uncoated gear. If the chrome coated gear run at 45,47 N, critical scoring load of uncoated gear, it could resist scoring much longer. Critical load that the chrome coated gear received scoring is 337.86 N, meanly, it received scoring as a result of running under 10 times the excessive load.

According to the experiments, compared to the uncoated gear chrome coated gear resisted approximately 10 times longer, nickel coated gear 5 times longer and manganese coated gear 1,5 times longer.

Besides after the experiments it was seen that after scoring started to occur, it continued rapidly. And this shows the effect of scoring formation on gears is a quite lot.

It was observed in the scoring load experiments that coating materials increased the scoring resistance of gears. Also coating materials prevent the discontinuities such as scratches and pores in the structure. The only disadvantage of coating material is accumulated corroded particles cause abrasive wear. In order to prevent abrasive wear, it is necessary to filter the lubricating oil well.

REFERENCES

1. Tunalioglu M S, Tuc B. Theoretical and experimental investigation of wear in internal gears. Wear 309(1–2) (2014) 208–215.

2. Tunalioglu M S. Experimental investigation of scoring formation in spur gears. Graduate Thesis, Gazi University Institute of Science and Technology (2004).

3. Tevruz T. Experiments of scoring and the calculation of scoring on gears by heat method. Wear 206 (1997) 204–2013.

4. Tevruz T. Experimental investigations on scoring of gears and calculation by temperature method. Wear 217 (1998) 81–94.

5. Wilfried J B. Lubrication of gearing. MEP Export Verlag ISBN 085298–831–1 (1993).

6. Naruse C. Haizuka S. Nemoto R. Kurukawa K. Studies on frictional loss, temperature rise and limiting load for scoring of spur gear. Bulletion of JSME 29 (248) (1986) 600–609.

7. Blok H. Theoretical study of temperature rise at surface of actual contactunder oiliness lubricating conditions. Ins. Mech. Eng. (1937) 222–235.

8. Lechner G. Die Fress–Grenzlast bei Stirnradern aus Stahl, PhD Thesis. Technischen Hochschule (1966).

9. Niemann G. Lechner G. Die Fress–Grenzlast bei Stirnradern aus Stahl, Erdöl und Kohle. Petrochemie. 20 (1967) 96-106.

10. Niemann G. Grekoussis R. Vergleichende Untersuchungen zur Fresstragfahigkeit von Hypoid–und Stirnradern. 112 (1970) 397-402.

11. Grekoussis R. Vergleichende Untersuchungen zur Fresstragfahigkeit von Hypoid–und Stirnradern, PhD Thesis Technischen Hochschule (1969).

12. Niemann G. Seitzinger K. Die Erwarmung einsatzgeharteter Zahnarader als Kennwert für ihre Fresstragfahigkeit. VDI–Z 113 (1971) 97-105.

13. Seitzinger K. Die Erwarmung Einsatzgeharteter Zahnrader als Kennwert für ihre Fresstragfahigkeit. PhD Thesis Technischen Universitat (1971).

14. Lechner G. Berechnung der Fresstragfahigkeit von Stirn– und Kegelradern. Zahnradfabrik Friedrichshafen 1st edn. (1973).

15. Yokoyama M. Ishikawa J. Hayashi K. Effect of tooth profile modification on the scoring resistance of heavy duty spur gears. Wear 19 (1972) 131–141.

16. Matsimaga T. Influence of profile modification and lubricant viscosity on scoring of helical gears. Trans. ASME Journal of Engineering for Industry (1974) 71–77.

17. Terauchi Y. Nadano H. Effect of tooth profile modification on the scoring resistance of spur gears. Wear 80 (1982) 27–41.

18. Imrek H. Unuvar A. An investigation of the effect of profile modification on the scoring in a spur gear. S. Ü. Faculty of Engineering and Architecture 13(1) (1998). 27–42.

19. Imrek H. Unuvar A. Investigation of influence of load and velocity on scoring of addendum modified gear tooth profiles. Wear 44(5) (2009) 938–948.

20. Terauchi Y. Kohno M. Nadano H. Nakamoto Y. Scoring resistance of spur gear with various coating. 1st report, scoring tests under forced lubrication. Bulletion of JSME 29(247) (1986) 235–241.

21. Terauchi Y. Nadano H. Kohno M. Scoring resistance of spur gear with various coating. 2nd report, scoring tests under dry friction. Bulletion of JSME 29(249) (1986) 999–1004.

22. Terauchi Y. Nadano H. Kohno M. Nakamoto Y. Scoring resistance of TiC–and TiN–coated gears. Tribology International 20(5) (1987) 248–254.

23. Calik A. Simsek M. Karakasa M S. Ucar N. Effect of boronizing on the microhardness and wear resistance of steel AISI 1050 steel and chilled cast iron. Metal Science and Heat Treatment 56(1–2) (2014) 89–92.

24. Duzcukoglu H. Calik A. Imrek H. Karakas M S. Examining of pitting and wear borided carburized and borocarburized AISI 8620 gears. Trib. Trans. 53 (2010) 485–490.

25. DIN 51354, Prüfung von Schmierölen Mechanische prüfung von Getriebeölen, in einer Zanrad–Verspannungs–Prüfmaschine nachdem FZG–Verfahren, Mai, (1964) 373-377.

Thermal Efficiency Optimization for A Natural-Gas Power Plant

Şaziye Balku[1] ID

[1] Atılım University, Energy Systems Engineering Department, Ankara, Turkey

ABSTRACT

Energy production from fossil fuels has been regarded as the main source of the climate change. The reason for that is the oxidation of carbon in fossil fuels to carbon dioxide during combustion and the highest percentage of greenhouse gases in atmosphere belongs to carbon dioxide. Amongst the fossil fuels natural gas is preferred due to its low emission of greenhouse gases and having no particulate matter after combustion. While the other fossil fuels emit mainly carbon dioxide during the combustion process; natural gas emits mostly water together with carbon dioxide. Around 22 % of the world's electricity is produced by natural gas and this share is expected to increase in near future. The power plants operating with natural gas as a gas cycle consisting of a compressor, a combustion chamber and gas turbine are combined with a vapor cycle in order to increase the efficiency. A heat recovery steam generator is used to reach this aim in recent years in generating steam by the heat received from the combustion gases leaving the gas turbine. It is very important to design and operate such energy conversion systems fired by natural gas in optimal conditions. If the efficiency can be increased, it can be said that the energetic, economic, and environmental aspects also improve. The modeling and optimization studies for a combined gas-vapor power plant are studied and the most important parameters which influence the efficiency are determined. The results indicate that the most effective parameters from the viewpoint of efficiency are air/fuel ratio, gas/steam ratio and the pressure ratios of the compressor and, thus, the gas turbine. The thermal efficiency increases by 18.25 % and, in the meantime, the exergy destroyed decreases by 9.84 % using optimum design parameters determined by the optimization algorithm proposed.

Keywords:
Optimization, Combined gas-steam, Thermal efficiency

INTRODUCTION

As the term implies, natural gas is a gas mixture naturally occurred and consists mainly of methane (CH_4) between the limits 87-97 mole %. The worldwide natural gas consumption for electricity generation will be growing by an average of 2.7 % per year since 2012 to the last estimation year of 2040. The natural gas share was 22 % of the total world electricity production in 2012 and it is expected to reach 28 % in 2040. The usage of natural gas in electricity generation is encouraged in USA from the viewpoint of low prices and low greenhouse gas emission [1]. During combustion, carbon oxidize to carbon dioxide and natural gas emits carbon dioxide like all the other fossil fuels, however considerably in fewer amounts and the main product of the combustion is water and has no harm to the environment. Furthermore, in electricity generation, the technology for natural gas is more efficient than coal. So, CO_2

reduction required by Kyoto Protocol can be met for many countries simply by using natural gas instead of coal. In order to meet the world's increasing energy demand, natural gas will continue to be used in the future depending on global expectations. For this reason, it is very important to design and operate such systems in optimal conditions. The most crucial factor for the evaluation of a power plant is thermal efficiency. Every increase in the percentage of thermal efficiency means an increase in the amount of power production and a decrease in the cost of production. Due to this reason, the present study is on the optimization of the efficiency of the power plants operated by natural gas. The most efficient power plants operate on gas-vapor cycles, where combustion gases are used in gas turbines and steam is used in steam turbines to produce additional power. The expanded gas leaving the gas turbine is used to provide steam in

a heat exchanger called heat recovery steam generator. So, the energy of the combustion gases leaving the gas turbine is utilized as the energy source of the steam turbine.

Recent studies on the performance of the combined gas steam power plants published in the literature depend on energy and exergy-based analysis and then optimization algorithms. The available part of energy which can be converted to work, or in other words, the maximum energy that can be obtained from a system is defined as "exergy". In order to determine the irreversibilities, entropy generation and the effective use of an energy source, the best way is exergy-based analysis. Exergy-based analyses are very convenient methods for assessing the performance of energy conversion systems. One of these studies presented a method for simulation of a model developed in Modelica and based on ThermoPower [2]. Kaviri et.al. [3] estimated the heat exchange between steam and gas side in a HRSG (heat recovery steam generator) configuration using a genetic algorithm technique. They concluded that the exergy destruction for HP-EVP (high pressure turbine-evaporator) was the highest amongst the other components, and, that increasing the inlet temperature of the steam generator more than 650⁰C had no better effect on both the thermal and exergy efficiencies of the vapor cycle. Ahmedi and Dinçer [4] chose an objective function related to cost including fuel, exergy destruction and purchase, and in order to minimize the objective function they used a genetic algorithm embedded in MATLAB. In their study on multi- objective optimization, Kaviri, Jaafar and Lazim [5] utilized two objective functions, the first one related with the costs consisting of component costs, the fuel cost, the duct burner cost and the exergy destruction cost. The second one was related with the exergy efficiency. In order to solve this multi-objective optimization problem a genetic algorithm approach was used. The temperature of the gas turbine, the pressure ratio of the compressor and the pinch point temperatures were determined as the most important parameters which affected the objective functions. It meant that small changes in these variables could cause large changes in the objective functions. In another study, Kaviri, Jaafar and Hosseini worked on an optimization algorithm having multi objective functions to find the most effective variables in a combined gas steam power plant [6]. Nadir and Ghenaiet [7] used a particle swarm algorithm as an optimization method and considered different configurations for heat recovery steam generator. A combined cycle with triple pressure and reheat was considered in a study by Bakhshmand et. al. [8] and an exergy and economic analysis were performed. The objective function was a cost function consisting of fuel, investment and destroyed exergy. A genetic algorithm was used as an optimization method developed in MATLAB. The authors concluded that the energy and exergy efficiencies were increased by 3 % using optimal variables, and the total cost was decreased

by 9 %. Furthermore, using optimal values for the decision variables brought a 0.58 €/h specific cost decrease when it was compared to the base values. The results of a case study performed in Montazar Ghaem power plant, Iran showed that using a cooling system for compressor inlet air caused a 3.2 % temperature drop which led 1.136 % increase in both thermal efficiency and a net output power in the warmest month. The exergy destroyed in the combustion chamber was decreased in considerable amount when the cooling system is operated [9].

Energy generation from fossil fuels has been regarded as the main source of CO_2 emission and has a significant effect on a global warming. As a result, natural gas can be considered as the best fossil fuel when compared to coal and petroleum oil from the environmental viewpoint since its hydrogen content is greater than the others. There are also some simulations and optimization studies related with environmental concerns, such as CO_2 capture which is a very important point. A natural gas fired power plant and a post combustion CO_2 capture unit were simulated in Aspen Plus V8.4 by Rezazadeh et. al. [10]. Simulations were performed at full and 90, 80, 70 and 60% part loads. They considered two processes one with CO_2 capture and the other was without CO_2 capture and the results confirmed performance viability. On the other hand, Pan et. al. [11] proposed some strategies to minimize the detrimental effects of carbon capture such as applying better heat transfer techniques, extracting some amount of steam from the HRSG and exhaust gas circulation,. Açıkkalp et.al. (2014) determined the exergy efficiency of a natural gas power plant in Eskişehir, Turkey to be 40.2 %, pointing out that the most important components for improving the system were the gas turbine and the combustion unit based on the real data [12]. A complex model including 1300 variables was developed and tested using a sequential quadratic programming for a cogeneration plant in the studies of Rodriguez-Toral, Morton and Mitchell [13]. In another similar study [14], twelve parameters were selected as decision variables affecting the exergetic efficiency, total cost and CO_2 emission which were the objective functions. The exergetic efficiency was increased by 6 % and in the same time CO_2 emission decreased by 5.63% using the optimum values for these variables.

In the present study, initially a basic model is developed using mass, energy and entropy balances for a combined gas vapor power system and in the second step the basic model is simulated under an optimization algorithm in order to find the optimum design parameters which yield maximum thermal efficiency.

MODELING AND OPTIMIZATION

In the present study, a combined gas-vapor power generation plant is taken into consideration. The mass, energy
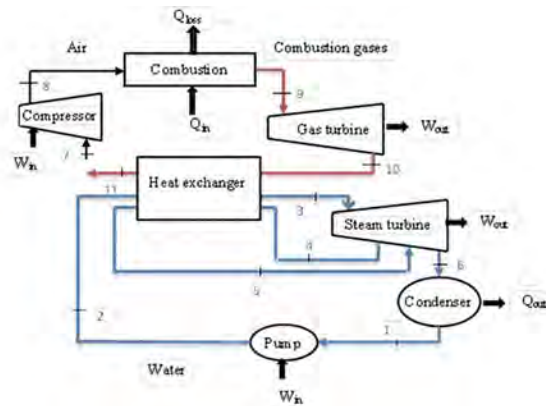
Figure 1. Flow diagram of the combined power plant

and entropy-based thermodynamic modeling of the plant [15, 16, 17] is simulated under an optimization algorithm.

The topping cycle is a gas-turbine power plant. A compressor, a combustion unit and a gas turbine are present in the gas cycle. The bottoming cycle is a non-ideal reheat Rankine cycle, which consists of a steam turbine, a boiler, a condenser and a pump. Steam turbine includes two stages as high pressure and low pressure, and the boiler is the heat recovery steam generator type. The flow diagram of the power plant simulated is given in Fig.1

The optimization problem has been formulated in order to determine the decision variables which maximize the objective function that is the thermal efficiency of a gas-vapor power generation plant.

$$\eta_{th} = \frac{\dot{W}_{net,plant}}{\dot{Q}_{in}}$$

The thermal efficiency is described (η_{th}) as the total net power achieved from the plant ($\dot{W}_{net,plant}$) divided by the inlet thermal energy ($\dot{Q}_{in}$). The objective function is subject to some other functions which describe the power plant by mass, energy and entropy balances. The functions can be expressed as equality constraints $h(x, y) = 0$ linear and/or nonlinear functions.The decision variables in the optimization algorithm are the followings;

- inlet temperature to compressor
- pressure ratios for compressor and gas turbine
- pump inlet pressure
- pump exit pressure
- exhaust gas temperature exiting HRGS system
- steam pressure entering LP turbine
- temperature of steam entering HP turbine
- gas-steam ratio
- air-fuel ratio

Therefore, we have 9 decision variables for the combined gas-vapor turbine cycle, and efforts are made to find the optimum quantities of these parameters which maximize the efficiency of the described plant. The decision variables have upper and lower limits.

$$x^L \le x \le x^U$$

where x is the vector of decision variables.

Mass, energy and entropy balances around the combined gas-steam turbine cycle

In the modeling of the plant, the following assumptions are accepted:

1. The operating conditions are steady.
2. Kinetic and potential energy changes between the inlet and the exit of the units are neglected.
3. Air is an ideal gas and enthalpy changes with temperature are taken into account.
4. The thermodynamic properties of combustion gases are equal to the properties of air.

Since the operation conditions are assumed to be steady, all the mass entering the units is equal to the mass leaving the units. Therefore, there is no need to show the mass balances around the system units. However, the energy and the exergy balances around all the most important units are taken into consideration and their bases are shown as follows:

Air Compressor and Gas Turbine

Under these conditions, air is assumed as an ideal gas and the enthalpy, entropy and relative pressure (P_r) values can be determined using ideal gas tables for air. For any process of ideal gases, the entropy change can be written as a function of temperature and pressure as follows;

$$s_{out} - s_{in} = \left(s^{\circ}_{out} - s^{\circ}_{in} \right) - R \ln \frac{P_{out}}{P_{in}} \tag{1}$$

where s is entropy, R is ideal gas constant, P is pressure. For any isentropic process for an ideal gas,

$$s_{out} = s_{in} \tag{2}$$

$$s^{\circ}_{out} = s^{\circ}_{in} + R \ln \frac{P_{out}}{P_{in}} \tag{3}$$

$$\frac{P_{out}}{P_{in}} = \frac{\exp(s^{\circ}_{out} / R)}{\exp(s^{\circ}_{in} / R)} \tag{4}$$

$$\left(\frac{P_{out}}{P_{in}}\right)_{s=const.} = \frac{P_{r,out}}{P_{r,in}} \tag{5}$$

Table 1. Decision variables: the assigned and optimum values

Parameter	Unit	Assigned Values	Optimum
Compressor inlet temperature	°C	15	15.2
Compressor pressure ratio		7	10.5
Pump inlet pressure	kPa	10	9.4
Pump outlet pressure	kPa	6000	6000
Air/fuel ratio		40	36.7
Gas/steam ratio		8,7	13
Temperature of steam entering HP turbine	°C	468	468
Pressure of steam entering LP turbine	kPa	1000	1000
Exhaust gas temperature leaving HRSG system	°C	200	199.7

where Pr is relative pressure and expressed as

$$P_r = \exp(s^{\circ}/R)$$

For non-isentropic processes take place in the compressor and the turbine calculated the equations 6 and 7 are used taking isentropic efficiencies into account.

$$\eta_C = \frac{h_{out,s} - h_{in}}{h_{out} - h_{in}} \quad (6)$$

$$h_{out} = h_{in} - \eta_T (h_{in} - h_{out,s}) \quad (7)$$

where h is enthalpy, η is isentropic efficiency.

Combustion Chamber

The enthalpy of the combustion gases exiting the combustion unit is determined by the following equation which is actually an energy based balance including an efficiency factor for the combustion chamber which represents the amount of heat leaving the combustion chamber by exhaust gases and the remaining part is representing the heat loss from combustion chamber.

$$\dot{m}_{air} (h_{air})_{in} + \dot{m}_{fuel} LHV_{fuel} + \dot{m}_{fuel} h_{fuel} =$$
$$(\dot{m}_{air} + \dot{m}_{fuel})(h_{air})_{out} +$$
$$(1 - \eta_{CC})(\dot{m}_{air}(h_{air})_{in} + \dot{m}_{fuel}(LHV_{fuel} + h_{fuel})) \quad (8)$$

where LHV_{fuel} is lower heating value and $\dot{m}_{fuel}$ is the flow rate of fuel in mass.

Heat Recovery Steam Generator (HRSG)
Energy Balance around HRSG

Table 2. The results of optimization algorithm for a simple combined power system

	Unit	Initial	Optimum
Q_{in}	kJ/s	2124900	2124900
W_{net}	kJ/s	648340	766570
n_{th}		30.51	36.08
Total exergy destroyed	kJ/s	1071700	966220

$$\dot{m}_S (h_{out} - h_{in})_{forHP} + \dot{m}_S (h_{out} - h_{in})_{forLP} =$$
$$(\dot{m}_{air} + \dot{m}_{fuel})\eta_{HRSG} (h_{in} - h_{out})_{gas} \quad (9)$$

Overall Energy Balances

$$\dot{Q}_{in} = \dot{m}_{fuel} LHV_{fuel} + \dot{m}_{air}(h_{air})_{in} + \dot{m}_{fuel} h_{fuel} \quad (10)$$

$$\dot{W}_{net,plant} = \dot{W}_{net,gas} + \dot{W}_{net,steam} =$$
$$\dot{W}_{T,gas} - \dot{W}_{C,gas} + \dot{W}_{T,steam} - \dot{W}_{P,steam} \quad (11)$$

$$\eta_{th} = \frac{\dot{W}_{net,plant}}{\dot{Q}_{in}} \quad (12)$$

Exergy Balances
Exergy balances for all the units in the power plant can be in the following forms:

$$\underbrace{\dot{X}_{in} - \dot{X}_{out}}_{\substack{\text{Rate of net exergy transfer} \\ \text{by heat, work, and mass}}} - \underbrace{\dot{X}_{destroyed}}_{\substack{\text{Rate of exergy} \\ \text{destruction}}} = \underbrace{\Delta\dot{X}_{system}}_{\substack{\text{Rate of change} \\ \text{of exergy}}} \quad (13)$$

The rate of change exergy with respect to time is zero by steady flow assumption. Then, the exergy destroyed during any steady flow process will be:

$$\dot{X}_{dest} = \dot{X}_{in} - \dot{X}_{out} =$$
$$\sum (1 - \frac{T_0}{T_k})\dot{Q}_k - \dot{W} + \sum \dot{m}\psi_{in} - \sum \dot{m}\psi_{out} \quad (14)$$

where is the heat transfer through the boundary at temperature Tk at location k,

$$\psi_{in} - \psi_{out} = [(h_{in} - h_{out}) - T_0(s_{in} - s_{out}) - \Delta ke - \Delta pe^{\nearrow 0}] \quad (15)$$

$$\dot{X}_{dest} = \dot{m}[T_0(s_{out} - s_{in}) - q] \quad (16)$$

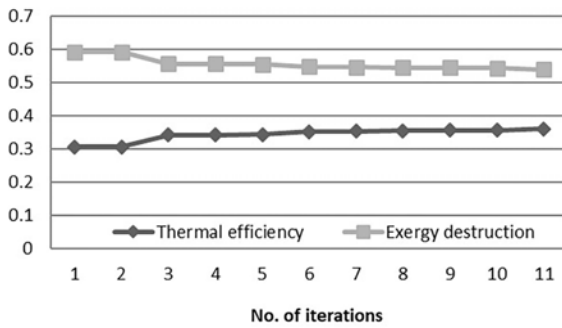since, from energy balance, $q - w = h_{out} - h_{in} + \Delta ke$

Figure 2. Thermal efficiency and exergy destruction

Figure 3. Exergy destruction of process units

$$\dot{X}_{dest} = T_0 \left(\dot{m}(s_{out} - s_{in}) - \dot{m}\frac{q}{T_0} \right) = T_0 \dot{S}_{gen} \qquad (17)$$

Alternatively, the exergy destroyed can be determined by entropy balances as follows:

$$\underbrace{\dot{S}_{in} - \dot{S}_{out}}_{\substack{\text{Rate of net entropy transfer} \\ \text{by heat and mass}}} + \underbrace{\dot{S}_{gen}}_{\substack{\text{Rate of entropy} \\ \text{generation}}} = \underbrace{\Delta\dot{S}_{system}}_{\substack{\text{Rate of change} \\ \text{of entropy}}}^{\overset{\searrow 0 \text{ (steady)}}{}} \qquad (18)$$

$$\rightarrow \quad \dot{S}_{gen} = \dot{S}_{out} - \dot{S}_{in}$$

The entropies of the liquid and vapor mixtures for water are determined by

$$s = s_f + x s_{fg} \qquad (19)$$

where x is the quality of the liquid-vapor mixture (mass percent of the steam in the mixture).

In entropy and exergy calculations; the amount of heat loss from the combustion and the condenser units are taken into account.

Optimization

A combined gas-steam turbine cycle model whose details are given above is simulated under an optimization algorithm written using MATLAB° [18, 19]. There are 20 parameters that must be entered initially into the algorithm: compressor inlet air temperature, fuel inlet temperature, pressure ratios for compressor and gas turbine, isentropic efficiencies for compressor, gas turbine, HP turbine and LP turbine, efficiencies for pump, combustion chamber and HRSG, pump inlet and outlet pressure, fuel rate in mass per time, air/fuel ratio, gas/steam ratio, pressure of steam entering LP turbine and the exhaust gas temperature leaving HRSG system, LHV of natural gas and finally, the temperature of steam entering the HP turbine. Amongst these parameters, nine parameters are selected as decision parameters given in Table 1 with their initially assigned values. In order to determine the steam and air properties, the algorithms appeared on Mathworks web [20] and [21] are used respectively.
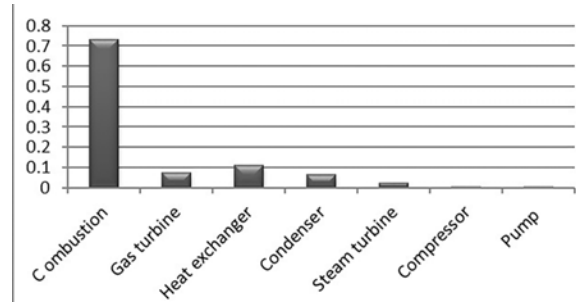
The algorithm which uses the power plant model described by the mathematical equations, the thermodynamic relations, the physical laws and the laws of thermodynamics is simulated under an optimization algorithm and the optimal values of these nine decision variables which make the objective function maximum are evaluated.

The steps in the optimization algorithm are as follows;
- The initial guesses for the decision parameters are assigned.
- Minimum and maximum constraints for the decision parameters are defined.
- The values of all the other system parameters are entered.
- The stopping criteria are given.
- The model is simulated with the initial guesses.
- Objective function is evaluated.
- The constraints and the stopping criteria are checked, if they are not suitable, new values for the decision parameters are determined by an embedded sub-program "fmincon"
- The iterations continue until the stopping criteria are reached.

RESULTS

The results achieved by the proposed optimization algorithm for a simple combined gas-vapor power system are shown in Table 1. In the algorithm, the initial quantities of the decision parameters are assigned for the defined system which can be seen in the third column on Table 1. The assigned values are taken from Çengel and Boles [15]. Then, an optimization sub-program "fmincon" is used to determine the optimal quantities for the decision parameters which make the thermal efficiency maximum. The fourth column indicates the optimal quantities of the decision parameters which make the objective function, or the thermal efficiency of the plant maximum. In the calculations, the efficiencies of units in the system are assigned to be 80 % (isentropic efficiencies of compressor, gas turbine, LP turbine and HP turbine, pump efficiency, and heat transfer efficiencies for combustion chamber and HRGS). LHV and the temperature of the fuel are taken as 47220 kJ/kg and 25°C, respectively. The fuel mass entering is 45 kg/s. The upper and lower boundaries are

0.5 and 1.5 times of the assigned values.

Table 2 shows the power produced as net power, the thermal efficiency of the plant and the total exergy destroyed by the main units of the plant for the assigned initial values and the optimum quantities of the decision parameters. The thermal efficiency increases from 30.51 % to 36.08 % when the optimum quantities for the decision parameters are used.

DISCUSSION

In the present study a combined gas-steam power cycle is modeled and then simulated by an optimization algorithm. Nine parameters are selected as decision parameters and the optimal values of these parameters are evaluated which give the maximum thermal efficiency. As it can be seen from Fig. 2 as thermal efficiency increases, the exergy destruction decreases as it is expected.

The exergy destruction according to the main units of the cycle is shown in Fig.3. The most important unit from the viewpoint of exergy destruction is the combustion chamber. 73 % of the total exergy destruction belongs to the combustion chamber. The heat exchanger follows it by 11 %. The exergy destruction percentages are determined by the optimal values of the decision parameters.

CONCLUSION

Upon analyzing Table 1 and Table 2 together, it can be concluded that the most important decision variables for the defined plant are air/fuel ratio, gas steam ratio and compressor pressure ratio as well as the gas turbine pressure ratio. Especially the gas-steam ratio and the compressor ratio reach the upper boundaries, implying that if the upper boundaries are increased, they too exceed beyond these figures. The other decision variables do not change much during the course of optimization. The results indicate that, using the same amount of thermal energy input, it is possible to higher the efficiency of the combined cycle by changing the decision variables. The cycle efficiency increases by 18.24 % and, in the meantime the exergy destroyed decreases by 8.92 % using optimum design variables determined by the optimization algorithm proposed. The maximum exergy destruction occurs in the combustion chamber and the heat exchanger follows it. In a future work, in order to satisfy the consistency with the actual power plants, the IP (intermediate pressure) turbine and an additional gas turbine unit are proposed embedded into the algorithm. Another suggestion will be the change of steam mass entering the HP, IP and LP as a decision variable.

REFERENCES

1. http://www.eia.gov/forecasts/ieo/electricity.cfm (download date 18.07.2016)
2. Tica A, Gueguen H, Dumur D, Faille D, Davelaar F. Design of a combined cycle power plant model for optimization. Applied Energy 98 (2012) 256–265.
3. Kaviri AG, Jaafar MNM, Tholudin ML, Barzegaravval H. Exergoenvironmental optimization of heat recovery steam generators in combined cycle power plant through energy and exergy analysis. Energy Conversion and Management 67 (2013) 27–33.
4. Ahmadi P. and Dinçer I. Thermodynamic analysis and thermoeconomic optimization of a dual pressure combined cycle power plant with a supplementary firing unit. Energy Conversion and Management 52 (2011) 2296–308.
5. Kaviri AG, Jaafar MNM Lazım TM. Modeling and multi–objective exergy based optimization of a combined cycle power plant using a genetic algorithm. Energy Conversion and Management 58 (2012) 94–103.
6. Kaviri AG, Jaafar MNM, Hosseini HS. Optimization and the effect of steam turbine outlet quality on the output power of a combined cycle power plant. Energy Conversion and Management 89 (2015) 231–243.
7. Nadir M, Ghenaiet A. Thermodynamic optimization of several (heat recovery steam generator) HRSG configurations for a range of exhaust gas temperatures. Energy 86 (2015) 685–695.
8. Bakhshmand SK, Saray RK, Bahlouli K, Eftekhari H, Ebrahimi A. Exergoeconomic analysis and optimization of a triple–pressure combined cycle plant using evolutionary algorithm. Energy 93 (2015) 555–567.
9. Noroozian A, Bidi M. An applicable method for gas turbine efficiency improvement. Case study: Montazar Ghaem power plant, Iran. Journal of Natural Gas Science and Engineering 28 (2016) 95–105.
10. Rezazadeh F, Gale WF, Hudges, KJ, Pourkashanian M. Performance viability of a natural gas fired combined cycle power plant integrated with post–combustion CO_2 capture at part–load and temporary non–capture operations. International Journal of Greenhouse Gas Control. 39 (2015) 397–406.
11. Pan M, Aziz F, Li B, Perry S, Zhang N, Bulatov I, Smith R. Application of optimal design methodologies in retrofitting natural gas combined cycle power plants with CO_2 capture 161 (2016) 695–706.
12. Açıkkalp E, Aras H, Hepbaslı A. Advanced exergy analysis of an electricity–generating facility using natural gas. Energy Conversion and Management 82 (2014) 146–153.
13. Rodriguez–Toral MA, Morton W, Mitchell DR. Using new packages for modeling, equation oriented simulation and optimization of a cogeneration plant. Computers and Chemical Engineering 24 (2000) 2667–2685.
14. Ganjehkaviri A, Jaafar MNM, Ahmadi P, Barzegaravval H. Modelling and optimization of combined cycle power plant based on exergoecenomic and environmental analyses. Applied Thermal Engineering 67 (2014) 566–578.
15. Çengel YA, Boles MA. Thermodynamics: An Engineering Approach, 8 th Ed.in SI Units, McGraw–Hill, 2015.
16. Borgnakke C, Sonntag RE. Fundamentals of Engineering Thermodynamics, 8 th Ed. SI Version, 2014.
17. Moran MJ. Shapiro HN. Fundamentals of Engineering

Thermodynamics, 5th Edition, John Wiley & Sons Inc., 2006.

18. The Mathworks. The language of technical computing. www.mathworks.com. (last accessed 03.03.2016).

19. Balku S. Comparison between alternating aerobic–anoxic and conventional activated sludge systems. Water Research, 41(10) (2007) 2220–2228.

20. http://www.mathworks.com/matlabcentral/fileexchange/9817–x– steam–– thermodynamic– properties– of–water– and– steam (download date: 04.02.2016)

21. http://www.mathworks.com/matlabcentral/fileexchange/25030–ideal– air–properties. (download date: 04.02.2016)

Geometric Soft Sets

Ömer Akgüller 🆔
Muğla Sıtkı Koçman University, Mathematics Department, Muğla, Turkey

ABSTRACT

Soft sets are efficient tools to determine uncertainty in systems. In this study, we introduce a new concept called geometric soft sets to present and analyze the geometrical, topological, and structural properties of complex networks.

Keywords:

Soft set sheory; Computational geometry; Soft computation; Network analysis

INTRODUCTION

Recently, the geometric structure of real network datasets has started to get a lot of attention amongst the researchers from various fields. The geometric characterization of such complex networks finds applications related to internet routing, community detection and data mining [3,5,7,24,28]. In real networks, geometrical, topological, and structural properties of data sets emerge from the spontaneous relation of each data element. In the literature, these relations are presented by the graph theoretical concepts [9,31,32]. Moreover, the structural analyses such as domination numbers of several types are presented in [15—18]. Besides, the theory of soft sets is also useful to express such relations [2,6,10,18,29,33].

The soft set theory introduced by Molodtsov in [27] is a mathematical tool dealing with the uncertainty of real-world problems which usually contain uncertain data. The soft set theory depends on the adequacy of the parametrization and differs from the similar theories such as fuzzy set theory, vogue set theory, and rough set theory, vague sets theory, and rough sets theory by the adequacy of the parametrization. Mathematically, one may conclude that a soft set over an initial universe is a parametrized family of subsets of the universe. It can be also seen that a soft set is not a set but set systems. By the introduction of the theory in [27], its algebraic [1,19] and topological properties [20,33], interlacing with other theories [14] and the application in other fields [2,6,11,21,30] have been studied intensively.

In this study, we present the emergent geometric structure of the systems expressed with the soft sets. In Section 2 we give the basic definitions and propositions on soft sets to construct geometric soft sets. We refer [26] to the interested readers for soft set theoretical analogues of the basic set operations. In Section 3, we present the concept of geometric soft sets. Basically we present the soft sets with the parameter mapping of hyperplane inclusions of the points in general positions. Right after the introduction of the geometric realization and structural concepts we study extremal properties of geometric soft sets in this section. Finally, in Section 4, we restrict our parameter mapping to similarity of the distances of points embedded in arbitrary metric spaces. We also construct two families of geometric soft sets which emerge from R^2 and a stock market network, then analyze them.

PRELIMINARIES
Definition 1
[26] A soft set over the universe set U is defined as a pair (F,E) such that E is a set of parameters and $F : E \to P(X)$ is a mapping. Mathematically, the soft set (F,E) is a parameterized family of subsets of the set U which can be stated as a set of ordered pairs

$$(F,E) = \left\{ \left(e, F(e) \right) : e \in E \ and \ F(e) \subset U \right\}.$$

Definition 2
Union of two soft sets of (F,A) and (G,B) over the common universe U is the soft set (H,C), where $C = A \cup B$ and $\forall e \in C$,

$$H(e) = \begin{cases} F(e), & \text{if } e \in A \setminus B \\ G(e), & \text{if } e \in B \setminus A \\ F(e) \cup G(e), & \text{if } e \in A \cap B \end{cases}.$$

The union of two soft sets is denoted by $(F,A) \widetilde{\cup} (G,B)$

Definition 3
[26] Intersection of two soft sets (F,A) and (G,B) over a common universe U is the soft set (H,C), where $C = A \cap B$ and $\forall e \in C$, H(e) = F(e) or G(e), (as both are same set).

The intersection of two soft sets is denoted by $(F,A) \widetilde{\cap} (G,B)$

Definition 4
[13] The soft set (F,E) is called a convex soft set if

$$F(ax + (1-a)y) \supseteq F(x) \cap F(y)$$

for every $x, y \in E$ and $a \in [0,1]$.

Definition 5
[25] The convex hull of a soft set (F,E), denoted by $\widetilde{conv}(F,E)$, is the smallest convex soft set over the universe U containing (F,E).

Preposition 1
[25] The convex hull of a soft set (F,E) is given by

$$\widetilde{conv}(F,E) = \bigcup_{n \in \mathbb{N}} \bigcup_{B \in C(e,n)} \bigcap \{F(e') : e' \in B\}$$

where

$$C(e,n) = \left\{ \begin{array}{c} \{e_1, \ldots, e_n\} \subset E : \exists \lambda_i \in [0,1] \, with \\ \sum_{i=1}^{n} \lambda_i = 1, e = \sum_{i=1}^{n} e_i \lambda_i = 1 \end{array} \right\}.$$

Preposition 2
[25] The intersection of an arbitrary collection of convex soft sets is a convex soft set.

GEOMETRIC SOFT SETS

A set in $\mathbb{R}^d$ is said to be in general position if no d+1 points lie on a hyperplane with co-dimension 1. Throughout this study we denote P(A,k) as the set of subsets of A with k elements and 2^A as the subsets of A.

Definition 6
Let $U \subset \mathbb{R}^d$ be the finite set of points in general position and $A \subseteq U$. For $F_A : E \to 2^A \setminus \{\emptyset\}$ incidence mapping, (F_A, E) is called a geometric soft set if

    i.   for $A = \{a_1, \ldots, a_k\}$, the tuple $(e_0, P(A,1)) \in (F_A, E)$;

    ii.   for all $i = 1, \ldots, k-2$; if $(e_{k-1}, P(A,k)) \in (F_A, E)$ and $\exists B \subset A$, then $(e_{i-1}, P(B,i)) \in (F_A, E)$.

Parameter mapping plays important role to define a soft set. Hence, in the view of geometric soft sets we define parameter mapping as incidence relation. Formally, if the tuple $(e_{k-1}, P(\{a_1, \ldots, a_k\}, k)) \in (F_A, E)$, then there is a hyperplane in $\mathbb{R}^k$ that contains $\{a_1, \ldots, a_k\}$.

To clarify the idea, we give the following example. Let us consider two sub-universes as A = {a, b, c} and B = {d, e, f, g}. The soft sets

$$(F_A, E) = \{(e_0, \{\{a\}, \{b\}, \{c\}\}), (e_1, \{\{a,b\}, \{a,c\}\}), (e_2, \{\{a,b,c\}\})\}$$

and

$$(F_B, E) = \{(e_0, \{\{d\}, \{e\}, \{f\}, \{g\}\}),$$
$$(e_1, \{\{d,e\}, \{d,f\}, \{d,g\}, \{e,f\}, \{e,g\}, \{f,g\}\}),$$
$$,(e_2, \{\{d,e,f\}, \{e,f,g\}, \{d,f,g\}, \{d,e,g\}\})\}.$$

The geometric realizations of the soft sets (F_A, E) and (F_B, E) are presented in Figure 1. with all triangular areas are included.

(F_A, E) (F_B, E)
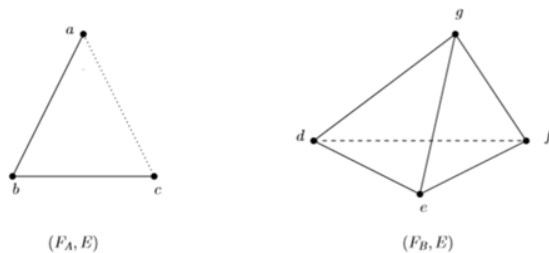
Figure 1. Lower dimensional examples of geometric soft sets.

Theorem 1
A geometric soft set with universe $\mathbb{R}^d$ has a geometric realization in $\mathbb{R}^{2d+1}$.

Proof
Let (F_A, E) be a geometric soft set with $F_A : E \to 2^A \setminus \{\emptyset\}$ and let $f : A \to \mathbb{R}^{2d+1}$ be an injection whose image is a set of points in general position. It is well known that any 2d + 1 or fewer points in general position are affine independent. Now let $(F_{\alpha 1}, E)$ and $(F_{\alpha 2}, E)$ are geometric soft subsets of (F_A, E) with $|F_{\alpha 1}(E)| = k_1$ and $|F_{\alpha 2}(E)| = k_2$. The soft union of these soft subsets has the cardinality

$$\left| (F_{\alpha_1}, E) \widetilde{\cup} (F_{\alpha_2}, E) \right| = \left| F_{\alpha_1}, E \right| + \left| F_{\alpha_1}, E \right| - \left| (F_{\alpha_1}, E) \widetilde{\cap} (F_{\alpha_2}, E) \right|$$
$$= k_1 + k_2 + 1 \leq 2d + 1$$

Henceforth, the points in α_1 and α_2 are affine indepen-

dent. This also implies that every convex combination x of points in $\alpha_1 \cup \alpha_2$ is unique. Besides, $\widetilde{conv}\left(F_{\alpha_1}, E\right) = \widetilde{conv}\left(F_{\alpha_2}, E\right)$ if and only if x is a convex combination of $\alpha_1 \cap \alpha_2$. Therefore, this implies that $F_{\alpha_1}(E) \cap F_{\alpha_2}(E)$ is either empty subset of the convex hull $conv f\left(\alpha_1 \cap \alpha_2\right)$ as it is required.

One of the mathematical concepts which may remind the geometric soft sets is the abstract simplicial complexes. Even though the abstract simplicial complexes are the collections of subsets of some vertex set, the main difference emerge from the hereditary structure. For each edge, abstract simplicial complexes contain all of its subsets; however geometric soft sets do not have to. For instance, in the above example, the geometric soft set (F_A,E) involves the triangle {a,b,c} along with the edges {a,b} and {a,c} but not the {a,c}. There is also one to one correspondence between the soft set (F_B,E) and the abstract simplicial complex with the vertex set {d,e,f,g}. It is possible to consider simplicial complexes as the hereditary geometric soft sets.

The dimension of a geometric soft set (F_A,E) is the maximum number k of $\left(e_{k-1}, P\left(\{a_1,\ldots,a_k\},k\right)\right)$, i.e. $\dim\left(F_A, E\right) = \max k$.

Definition 7
Let (F_A,E) be a geometric soft set. A soft subset (F_B,E) of (F_A,E) is a geometric soft subset if and only if (F_B,E) is also a geometric soft set. For any geometric soft set (F_A,E) with dimension d and for any $0 \le i \le d$ the geometric soft subset

$$\left(F_A, E\right)^{(i)} = \left\{\left(F_{B_j}, E\right) \tilde{\subset} \left(F_A, E\right) : \dim\left(F_{B_j}, E\right) \le d\right\}$$

for all $B_i \subset A$ is called the i-th soft skeleton of (F_A,E).

Remark 1
It is straightforward that a geometric soft set is connected if and only if its 1st soft skeleton is connected.

Definition 8
Let $\left(\mathcal{F}, \mathcal{E}\right) = \overset{n}{\underset{i=1}{U}}\left(F_{A_i}, E\right)$ be a family of geometric soft sets with dimension d. $\left(\mathcal{F}, \mathcal{E}\right)$ is homogeneous if and only if for all (F_{A_i},E), there exists j≠i and j=1,…,n such that $F_{A_i}\left(e_k\right) \cap F_{A_j}\left(e_k\right) \ne \varnothing$ for any k = 1,…,d. Moreover, $\left(\mathcal{F}, \mathcal{E}\right)$ is connected if and only if geometric realization of $\left(\mathcal{F}, \mathcal{E}\right)$ is connected.

The sense behind the notion of a homogeneous family of geometric soft sets is the result of gluing geometric soft sets all having the same dimension. For instance, let us define three geometric subsets

$$\left(F_A, E\right) = \left\{\left(e_0, \{\{a\},\{b\}\}\right), \left(e_1, \{\{a,b\}\}\right)\right\}$$

$$\left(F_B, E\right) = \left\{ \begin{array}{l} \left(e_0, \{\{b\},\{c\},\{d\}\}\right), \left(e_1, \{\{b,c\},\{c,d\}\}\right), \\ \left(e_2, \{\{b,c,d\}\}\right) \end{array} \right\},$$

$$\left(F_C, E\right) = \left\{ \begin{array}{l} \left(e_0, \{\{c\},\{d\},\{e\},\{f\}\}\right), \\ \left(e_1, \{\{c,d\},\{c,f\},\{d,f\},\{e,f\}\}\right), \\ \left(e_2, \{\{c,d,f\}\}\right) \end{array} \right\}$$

and $\left(\mathcal{F}, \mathcal{E}\right) = \left(F_A, E\right) \cup \left(F_B, E\right) \cup \left(F_C, E\right)$

The geometric realization of $\left(\mathcal{F}, \mathcal{E}\right)$ is presented in Figure 2.
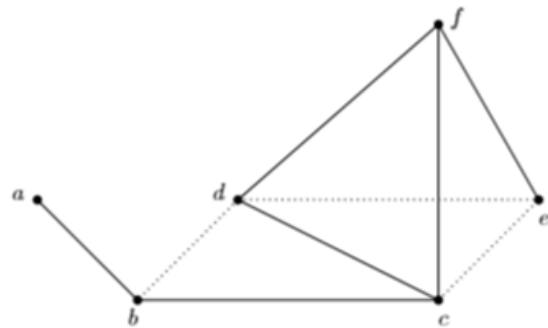

Figure 2. The geometric realization of a family of geometric soft sets

Definition 9
Let k ≥ 2 and $\left(\mathcal{F}, \mathcal{E}\right)$ be a family of geometric soft sets. $\left(\mathcal{F}, \mathcal{E}\right)$ is k-uniform if all of its elements have cardinality k, i.e. $\left|F_A(E)\right| = k$ for all $\left(F_A, E\right) \in \left(\mathcal{F}, \mathcal{E}\right)$.

Definition 10
Let $\left(\mathfrak{F}, \mathfrak{E}\right)$ be a family of k-uniform families of geometric soft sets. $\left(\mathfrak{F}, \mathfrak{E}\right)$ is called k-partite if A of $\left(\mathfrak{F}, \mathfrak{E}\right)$ can be partitioned into k pairwise disjoint soft sets $A = A_1 \cup A_2 \cup \ldots \cup A_k$ with $A_i \cap A_j = \varnothing$ for i≠j, such that $\left|S \cap A_i\right| \le 1$ for all i = 1,…,k and every $S \in F_A(E)$.

Definition 11
Let $\left(\mathfrak{F}, \mathfrak{E}\right)$ be a family of k-uniform families of geometric soft sets. If $\left(\mathfrak{F}, \mathfrak{E}\right)$ can be partitioned into pairwise disjoint soft sets with $\left|A_i\right| = \ell_i$ such that

$$F_A(E) = \left\{S \subset F_{A_i}(e) : \left|S \cap A_i\right| = 1\right\}$$

for all i=1,…,k, then $\left(\mathfrak{F}, \mathfrak{E}\right)$ is called complete k-partite

and denoted as $\left(\mathfrak{F},\mathfrak{E}\right)^{(k)}_{\ell_k}$.

One of the extremal problem arise in the context of k-uniform geometric soft sets is the maximum number of parameters assigned to sub-universe with fixed |A|=n and k values without containing certain soft subsets.

Definition 12

. Let k ≥ 2 and let $\left(\mathfrak{F},\mathfrak{E}\right)$ be a family of k-uniform families of geometric soft sets. A k-uniform family that contains no distinct copy of any $\left(\mathcal{F},\mathcal{E}\right)\in\left(\mathfrak{F},\mathfrak{E}\right)$ as a soft subset is called $\left(\mathfrak{F},\mathfrak{E}\right)$-free. The maximal number of $\left(\mathfrak{F},\mathfrak{E}\right)$-free k-uniform family on |A|=n, $\max\left(n,\left(\mathfrak{F},\mathfrak{E}\right)\right)$, can be given as the maximum number of $|F_A(E)|$, i.e. $\max\left(n,\left(\mathfrak{F},\mathfrak{E}\right)\right)=\max\left\{\left|F_A(E)\right|\right\}$.

Theorem 2

Let $\left(\mathfrak{F},\mathfrak{E}\right)$ be a family of k-uniform families of geometric soft sets and |A|=n. If $\left(\mathfrak{F},\mathfrak{E}\right)$ has no k-partite member, then there is a c > 0 such that $\max\left(n,\left(\mathfrak{F},\mathfrak{E}\right)\right)\geq cn^k$.

Proof

Let |A|=n and $\left(\mathfrak{F},\mathfrak{E}\right)$ be complete k-partite family with

$$\ell_i = \frac{n+i-1}{k}.$$

Since all soft subsets of $\left(\mathfrak{F},\mathfrak{E}\right)$ are k-partite they are $\left(\mathfrak{F},\mathfrak{E}\right)$-free. Hence $\left(\mathfrak{F},\mathfrak{E}\right)$ involves

$$\prod_{1\leq i\leq k}\frac{n+i-1}{k}\geq\left(\frac{n-l}{k}\right)^k$$

many families for some 0≤l<k. This completes the proof.

GEOMETRIC SOFT SETS IN METRIC SPACES

Different restrictions on the parameter map of a geometric soft set yield the soft analogues of well-known computational complexes. In this section, we let the universe of a geometric soft set be any metric space $\mathcal{P}$. Then, the geometric soft set $\left(F_A^\delta, E\right)$ can be defined with the parameter mapping

$$F_A^\delta : A \subset \mathcal{P} \rightarrow E$$

as if the tuple $\left(e_{k-1}^\delta, P\left(\{a_1,...,a_k\},k\right)\right)\in\left(F_A,E\right)$, then the points {a_1,...,a_k} are with the maximum pairwise distance δ.

An Example in $\mathbb{R}^2$

Now let us consider the randomly sampled 100 points in a sub-region of $\mathbb{R}^2$. The sub-region we choose is $4 \leq x^2 + y^2 \leq 16$ and the generated points are presented in Figure 3.
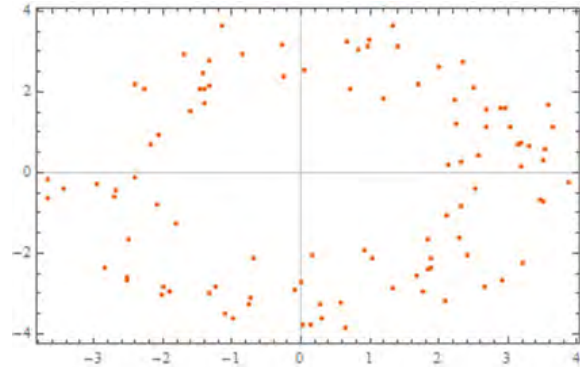

Figure 3. Randomly sampled points in $\mathbb{R}^2$

The results emerge from the families of $\left(F_A^\delta, E\right)$ with usual Euclidean metric are presented in Table 1 for different δ values.

Table 1. Computational results for the family of geometric soft sets

δ Value	Number of Soft Sets	Maximum Dimension	Connected
5	1	100	Yes
4.694	2	99	Yes
3	28	44	Yes
2	33	28	Yes
1	54	15	Yes
0.853	60	13	Yes
0.852	60	12	No
0.5	68	5	No
0.4	76	5	No
0.3	86	4	No
0.2	94	3	No
0.109	100	1	No

From the computational results presented in Table 1. it can be straightforwardly deduced that the connectivity and dimension of the family of geometric soft sets representation of randomly sampled points in $\mathbb{R}^2$ is decreasing as the δ value of $\left(F_A^\delta, E\right)$ decreases. Similarly, the number $\left|\left(\mathcal{F},\mathcal{E}\right)\right|$ increases as δ descreses. The threshold value of δ for the connectivity is 0.853. This yields that, for the δ=0.853 the system represented by the geometric soft sets involves the information with dimension 13 and there exists the continuous geometric flow of the information through the system.

Geometric Soft Sets Emerge From BIST

Since global stock markets are continuously in complex interaction they form a complex system and have long been studied by several researchers [4,12,23].

The data used in this section consists of daily data from

the period January 2013 to January 2015. 93 companies operating in Borsa Istanbul (BIST) 100 Index (XU100) are considered. Sessional return Cl_i for the i-th company is calculated as the logarithmic return in the value of index compared to previous session's closing value as the logarithmic difference.

The metric used for comparing time series of logarithmic returns is the correlation distance

$$d_{Corr}(i,j) = \sqrt{2(1-\rho_{ij})},$$

where

$$\rho_{ij} = \frac{\langle Cl_i, Cl_j \rangle - \langle Cl_i \rangle \langle Cl_j \rangle}{\sqrt{(\langle Cl_i^2 \rangle - \langle Cl_i \rangle^2)(\langle Cl_j^2 \rangle - \langle Cl_j \rangle^2)}}$$

with $\langle \ldots \rangle$ is the temporal average performed on all the trading days. The data and the correlation distance matrix is presented in Figures 4 and 5, respectively. In Figure 5, it can be concluded that the diagonal elements are zero and the rows and columns which has the darker color are the stocks with long distances. Here, the long distance directly corresponds the smaller correlation amongst the stock markets.
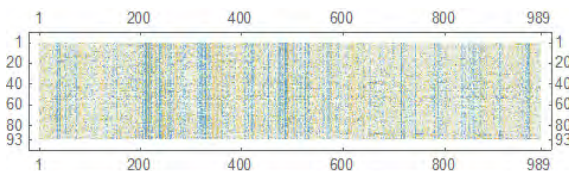

Figure 4. Logarithmic return of the 93 companies operating in 989 days
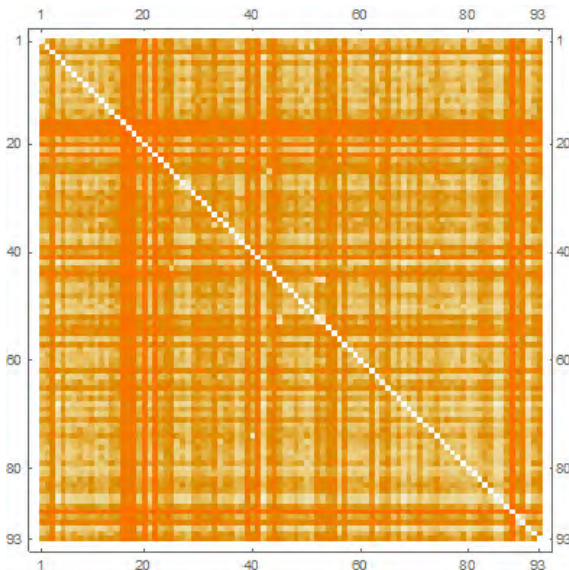

Figure 5. Correlation distances of logarithmic return 93 companies. Light and dark colors indicate strong and weak correlations, respectively

The results emerge from the families of (F_A^δ, E) with correlation distance are presented in Table 2 for different δ values.

Table 2. Computational results for the family of geometric soft sets

δ Value	Number of Soft Sets	Maximum Dimension	Connected
2	1	100	Yes
1	1	93	Yes
0.899	1	92	Yes
0.898	2	92	No
0.7	12	82	No
0.6	31	64	No
0.5	56	37	No
0.4	81	10	No
0.3	87	7	No
0.2	86	6	No
0.15	100	1	No

From the computational results presented in Table 2 it can be seen that the connectivity and dimension of the family of geometric soft sets representation of BIST is decreasing as the δ value of (F_A^δ, E) decreases as same as the previous example. Similarly, the number $\|(\mathcal{F}, \mathcal{E})\|$ increases as δ descreses. The threshold value of δ for the connectivity is 0.899 which is also similar to the previous example. This yields that, for the δ=0.898 the system represented by the geometric soft sets involves the information with dimension 92 and there exists the continuous geometric flow of the information through the system.

CONCLUSION

In this paper, we have presented a new concept called geometric soft set which emerge from the incidence parameter over the points in general position. After the introduction of the geometric realization of the families of geometric soft sets, we study extremal properties for such families. For fixed number of the sub-universe, we present an upper bound for the crossing of respected hyperplanes.

Several type of complex systems emerge a geometric structure. To obtain this, we have present a restriction on the parameter meter and study different type of geometric soft sets in different metric spaces. First one is the usual metric space of $\mathbb{R}^2$, and the second one is the metric space endowed with the correlation distance of time series. We have showed that the geometric soft sets emerge from the BIST has higher dimensions than the ones from usual metric space.

REFERENCES

1. Aktaş H, Çağman N. Soft sets and soft groups. Information sciences 177(13) (2007) 2726–2735.

2. Balcı MA, Akgüller Ö. Mathematical Morphology on Soft Sets for Application to Metabolic Networks. Advanced Computational Methods for Knowledge Engineering, 354

(2015) 209–218

3. Balcı MA. Hiearchies in Communities of Borsa Istanbul Stock Exchange. Hacettepe Journal of Mathematics and Statistics, (2016) In Press, DOI: 10.15672/HJMS.201614520777

4. Balcı MA. Fractional Virus Epidemic Model on Financial Networks. Open Mathematics 46 (2016) 1074–1086.

5. Balcı MA, Atmaca SP, Akgüller Ö. Hyperpath Centers. Advanced Computational Methods for Knowledge Engineering 473 (2016) 129–137.

6. Balcı MA, Akgüller Ö. Soft Vibrational Force on Stock Market Networks. Library Journal 3 (2016) e3050.

7. Boguñá M, Krioukov D, Claffy KC. Navigability of complex networks. Nature Physics 5 (2008) 74.

8. Boguñá M, Papadopoulos F, Krioukov D. Sustaining the internet with hyperbolic mapping. Nature Communications 1 (2010) 62.

9. Bullmore E, Sporns O. Complex brain networks: graph theoretical analysis of structural and functional systems. Nature Reviews Neuroscience 10 (3) (2009) 186–198.

10. Çağman N, Deli I. Means of FP–soft sets and their applications. Hacettepe Journal of Mathematics and Statistics 41 (5) (2012)

11. Çağman N, Enginoğlu S, Çıtak F. Fuzzy soft set theory and its applications. Iranian Journal of Fuzzy Systems 8 (3) (2011) 137–147.

12. Chi KT, Liu J, Lau FC. A network perspective of the stock market. Journal of Empirical Finance 17 (4) (2010) 659–667.

13. Deli I. Convex and concave soft sets and some properties. arXiv preprint (2013) arXiv:1307.4960.

14. Deli I. Interval–valued neutrosophic soft sets and its decision making. International Journal of Machine Learning and Cybernetics 8 (2) (2015) 1–12.

15. Dogan D. Average lower domination number for some middle graphs. Mathematical Combinatorics 4 (2012) 58–67.

16. Dogan D, Dundar P. The average covering number of a graph. Journal of Applied Mathematics 2013 (2013) Article ID 849817.

17. Dogan Durgun D, Altundağ FN. Liar's Domination in Graphs. Bulletin of International Mathematical Virtual Instutite 7 (2017) 407–415.

18. Dogan Durgun D, Lökçü B. Strong Domination Number of Some Graphs. CBU Journal of Science 11 (2) (2015) 89–91.

19. Jun YB. Soft BCK/BCI–algebras. Computers and Mathematics with Applications 56 (10) (2008) 2621–2628.

20. Ge X, Li Z, Ge Y. Topological spaces and soft sets. Journal of Computational Analysis and Applications 13 (5) (2011) 881–885.

21. Kalayathankal SJ, Singh GS. A fuzzy soft flood alarm model. Mathematics and Computers in Simulation 80 (5) (2010) 887–893.

22. Khan MS, Al-Garadi MA, Wahab AWA, Herawan T. An alternative data filling approach for prediction of missing data in soft sets (ADFIS). SpringerPlus 5 (1) (2016) 1348.

23. Kimoto T, Asakawa K, Yoda M, Takeoka M. Stock market prediction system with modular neural networks. In Neural Networks, paper presented at: 1990 IJCNN International Joint Conference, pp. 1–6, 1990.

24. Kleinberg R. Geographic routing using hyperbolic space. Paper presented at INFOCOM 2007. 2f6th IEEE International Conference on Computer Communication, 2007.

25. Majeed SN. Some notions on convex soft sets. Annals of Fuzzy Mathematics and Informatics 12 (4) (2016) 517–526.

26. Maji PK, Biswas R, Roy A. Soft set theory. Computers & Mathematics with Applications 45 (4–5) (2003) 555–562.

27. Molodtsov D. Soft set theory–first results. Computers & Mathematics with Applications 37 (4–5) (1999) 19–31.

28. Narayan O, Saniee I. Large–scale curvature of networks. Physics Review E 84 (2011) 066108.

29. Öztunç S. Some properties of soft categories. International Journal of Modeling and Optimization 6 (2) (2016) 91–95.

30. Öztunç S, İhtiyar S. Properties of Soft Homotopy in Digital Images. American Institute of Physics, 1798 (2017) 020120.

31. Sreejith RP, Mohanraj K, Jost J, Saucan E, Samal A. Forman curvature for complex networks. Journal of Statistical Mechanics: Theory and Experiment 6 (2016) 063206.

32. Strogatz SH. Exploring complex networks. Nature 410 (2001) 268–276.

33. Yüksel Ş, Güzel Ergül Z, Tozlu N. Soft covering based rough sets and their application. The Scientific World Journal (2014)

HİTİT
UNIVERSITY

Symmetry in Complex Contact Manifolds

Belgin Korkmaz ⓘD
Hitit University, Mathematics Department, Çorum, Turkey

ABSTRACT

We define complex locally $\mathcal{H}$-symmetric spaces. As an example we prove that complex (κ,μ)-spaces with $\kappa < 1$ are locally $\mathcal{H}$-symmetric.

Keywords:
Complex contact geometry; Symmetry; Local symmetry

INTRODUCTION

Takahashi defined local φ-symmetry for Sasakian manifolds by the curvature condition that

$$g((\nabla_X R)(Y,Z)W,T) = 0 \qquad (1)$$

for all horizontal vector fields X,Y,Z,W,T ([12]). There are two generalizations to contact metric manifolds. In [2], contact metric manifolds satisfying the curvature condition (1.1) are called locally φ-symmetric. In [6] another definition is given. A contact metric manifold is called locally φ-symmetric if characteristic reflections are local isometries. This condition leads to infinitely many curvature conditions including the above condition (1.1). Boeckx proved that (κ,μ)-spaces satisfy this condition ([5]). This gives a set of non Sasakian examples.

Symmetry for complex contact metric manifolds is studied by Blair and Mihai in [3], [4]. They defined a complex contact metric manifold to be *GH-locally symmetric* if the reflections in the integral submanifolds of the vertical bundle are isometries. They also proved in [4] that a complex (κ,μ)-space with $\kappa < 1$ is GH-locally symmetric.

In this paper, we will use the first generalization of local symmetry and define a complex contact metric manifold to be locally $\mathcal{H}$-symmetric (in order not to confuse with GH-locally symmetric) if it satisfies the curvature condition (1) and we will give a simple and detailed proof showing that complex (κ,μ)-spaces with $\kappa < 1$ satisfy this condition.

PRELIMINARIES

Let M be a complex manifold of dimension $2n+1$. It is called a *complex contact manifold* if it has an open covering $\{\mathcal{O}\}$ of coordinate neighborhoods such that:

1) On each $\mathcal{O}$ there is a holomorphic 1-form ω such that $\omega \wedge (d\omega)^n \neq 0$,

2) On $\mathcal{O} \cap \mathcal{O}' \neq \varnothing$ there is a non-vanishing holomorphic function f such that $\omega' = f\omega$.

The complex contact structure determines a non-integrable subbundle $\mathcal{H}$ by the equation $\omega = 0$; $\mathcal{H}$ is called the *complex contact subbundle* or simply the *horizontal subbundle*.

On a complex contact manifold M, there is a Hermitian metric g, local (real) 1 forms u and $v = u \circ J$, local (real) dual vector fields U and $V = -JU$, and (1,1) tensor fields G and $H = GJ$ such that:

1) $G^2 = H^2 = -I + u \otimes U + v \otimes V,$
   $G^2 = H^2 = -I + u \otimes U + v \otimes V,$
   $g(U,X) = u(X), \quad g(X,GY) = -g(GX,Y),$
   $GJ = -JG, \quad GU = 0, \quad u(U) = 1,$

2) On $\mathcal{O} \cap \mathcal{O}' \neq \varnothing$

   $u' = Au - Bv, \quad v' = Bu + Av,$
   $G' = AG - BH, \quad H' = BG + AH$

where A and B are functions with $A^2 + B^2 = 1$.

As a result of these conditions, the following identities also hold:

3) $HG = -GH = J + u \otimes V - v \otimes U$,

$JH = -HJ = G$, $g(HX,Y) = g(X,HY)$,

$GV = HU = HV = 0$, $uG = vG = uH = vH = 0$,

$JV = U$, $g(U,V) = 0$,

$du(X,Y) = g(X,GY) + (\sigma \wedge v)(X,Y)$,

$dv(X,Y) = g(X,HY) - (\sigma \wedge u)(X,Y)$

where $\sigma(X) = g(\nabla_X U, V)$, ∇ being the Levi-Civita connection of g (see [1], [7] and [9]).

Here $\omega = f(u - iv)$ where f is a non-vanishing complex-valued function. Also, on the intersections the subbundle generated by U and V is the same as the subbundle generated by U' and V'. Hence we have a global bundle V orthogonal to $\mathcal{H}$. This bundle is called the *vertical subbundle* and it is typically assumed to be integrable. We refer to a complex contact manifold with the above structure tensors satisfying these conditions as a complex *contact metric manifold*.

In order to split the covariant derivatives of U and V into symmetric and skew-symmetric parts, we define two other local structure tensors:

$$h_U = \frac{1}{2}\mathrm{sym}\mathcal{L}_U G \circ p \text{ and } h_V = \frac{1}{2}\mathrm{sym}\mathcal{L}_V H \circ p$$

where ``sym'' denotes the symmetric part and p denotes the projection $TM \to \mathcal{H}$. These operators satisfy the following properties [2,8]:

$h_U G = -Gh_U$, $h_V H = -Hh_V$,

$h_U U = h_U V = h_V U = h_V V = 0$,

$\nabla_X U = -GX - Gh_U X + \sigma(X)V$,

$\nabla_X V = -HX - Hh_V X - \sigma(X)U$.

In order to define a complex (κ,μ)-space, we consider complex contact metric manifold M with $h_U = h_V = h$. In this case, h anti-commutes with G and H, and hence commutes with J. If the following curvature conditions hold for some constants κ and μ, then M is called a *complex (κ,μ)-space* ([11]):

$R(X,Y)U = \kappa(u(Y)X - u(X)Y) + \mu(u(Y)hX - u(X)hY)$

$+ (\kappa - \mu)(v(Y)JX - v(X)JY)$

$+ 2((\kappa - \mu)g(JX,Y) + (4\kappa - 3\mu)u \wedge v(X,Y))V,$ (2)

$R(X,Y)V = \kappa(v(Y)X - v(X)Y) + \mu(v(Y)hX - v(X)hY)$

$- (\kappa - \mu)(u(Y)JX - u(X)JY)$ (3)

$- 2((\kappa - \mu)g(JX,Y) + (4\kappa - 3\mu)u \wedge v(X,Y))U,$

$\Omega(X,Y) = (2 - \mu)g(JX,Y) + 2g(JhX,Y) + 2((2 - \mu)u \wedge v(X,Y)).$ (4)

Here $\Omega = d\sigma$.

The following theorem is proved in [11].

Theorem 1

Let M be a complex (κ,μ)-space. Then $\kappa \leq 1$. If $\kappa = 1$, then $h = 0$ and M is normal. If $\kappa < 1$, then M admits three mutually orthogonal distributions $[0]$, $[\lambda]$ and $[-\lambda]$, defined by the eigenspaces of h, where $\lambda = \sqrt{1 - \kappa}$.

Curvature of a complex (κ,μ)-space is completely determined. For details see [11].

Curvature of complex (κ,μ)-spaces

In this section we will write the curvature tensor for a complex (κ,μ)-space. In the expression for the curvature tensor there are several terms. In order to give a simpler expression if we group some terms, we come up with the following tensors which are defined for vector fields X, Y:

$A(X,Y) = g(X,hY) + (1 - \mu/2)g(X,Y)$,

$B(X,Y) = g(X,Y) + (2 - \mu)/(2\lambda^2)g(X,hY)$,

$C(X,Y) = u(X)((\kappa - 1 + \mu/2)Y + (\mu - 1)hY)$,

$D(X,Y) = v(X)((\kappa - 1 - \mu/2)JY - hJY)$.

Here A, B are $(0,2)$ tensors and C, D are $(1,2)$ tensors.

We also define the following $(0,3)$ tensors:

$f(X,Y,Z) = g(C(X,Y) + D(X,Y) - C(Y,X) - D(Y,X),Z)$

$+ 2g(D(Z,Y),X) - 4(2\kappa - 1 - \mu)v(Z)2u \wedge v(X,Y),$

$k(X,Y,Z) = g(C(JX,Y) + D(JX,Y) - C(JY,X) - D(JY,X),Z)$

$+ 2g(D(JZ,Y),X) - 4(2\kappa - 1 - \mu)u(Z)2u \wedge v(X,Y).$

Note that when the vector fields are horizontal, the tensors C, D, f and k vanish.

Theorem 2

Let M be a complex (κ,μ)-space with $\kappa < 1$. Then, for vector fields X, Y, Z, the curvature tensor is given by

$$R(X,Y)Z = (A(Y,Z) + (\kappa - 1 + \frac{\mu}{2})(u(Y)u(Z) + v(Y)v(Z)))X$$

$$- (A(X,Z) + (\kappa - 1 + \frac{\mu}{2})(u(X)u(Z) + v(X)v(Z)))Y$$

$$+ (B(Y,Z) + (\mu - 1)(u(Y)u(Z) + v(Y)v(Z)))hX$$

$$- (B(X,Z) + (\mu - 1)(u(X)u(Z) + v(X)v(Z)))hY$$

$$- (A(Y,JZ) + (\kappa - 1 - \frac{\mu}{2})2u \wedge v(Y,Z))JX$$

$$+ (A(X,JZ) + (\kappa - 1 - \frac{\mu}{2})2u \wedge v(X,Z))JY$$

$$+ (2A(X,JY) + (2\kappa - 2 - \mu)2u \wedge v(X,Y))JZ$$

$$- (B(Y,JZ) - 2u \wedge v(Y,Z))hJX$$

$$+ (B(X,JZ) - 2u \wedge v(X,Z))hJY$$

$$+ (2B(X,JY) - 4u \wedge v(X,Y))hJZ$$

$$+ \frac{\mu}{2}(g(Y,GZ)GX - g(X,GZ)GY$$

$$+ g(Y,HZ)HX - g(X,HZ)HY)$$

$$+ \frac{2\kappa - \mu}{2\lambda^2}(g(Y,hGZ)hGX - g(X,hGZ)hGY$$

$$+ g(Y,hHZ)hHX - g(X,hHZ)hHY)$$

$$+ \mu(g(Y,GX)GZ + g(Y,HX)HZ)$$

$$+ f(X,Y,Z)U + k(X,Y,Z)V.$$

Proof

First, we write any vector field X uniquely as

$$X = X_\lambda + X_{-\lambda} + u(X)U + v(X)V$$

where $X_\lambda \in [\lambda]$ and $X_{-\lambda} \in [-\lambda]$. We can write the terms $R(X_{\pm\lambda}, Y_{\pm\lambda})Z_{\pm\lambda}$ using the formulas given in [11]. The terms $R(X,Y)U$, $R(X,Y)V$, $R(U,X)Y$, $R(V,X)Y$, $R(X,U)Y$ and $R(X,V)Y$, can be computed by using the conditions (2) and (3). Then, by using the identities

$$X_\lambda = \frac{1}{2}\left(X + \frac{1}{\lambda}hX - u(X)U - v(X)V\right),$$

$$X_{-\lambda} = \frac{1}{2}\left(X - \frac{1}{\lambda}hX - u(X)U - v(X)V\right),$$

we obtain the formula in the theorem. Keep in mind that $hX_\lambda = \lambda X_\lambda$, $hX_{-\lambda} = -\lambda X_{-\lambda}$ and $hU = hV = 0$. $\square$

When the vector fields are horizontal, the above expression simplifies to

$$R(X,Y)Z = A(Y,Z)X - A(X,Z)Y + B(Y,Z)hX - B(X,Z)hY$$

$$- A(Y,JZ)JX + A(X,JZ)JY + 2A(X,JY)JZ$$

$$- B(Y,JZ)hJX + B(X,JZ)hJY + 2B(X,JY)hJZ$$

$$+ \frac{\mu}{2}(g(Y,GZ)GX - g(X,GZ)GY$$

$$+ g(Y,HZ)HX - g(X,HZ)HY)$$

$$+ \frac{2\kappa - \mu}{2\lambda^2}(g(Y,hGZ)hGX - g(X,hGZ)hGY$$

$$+ g(Y,hHZ)hHX - g(X,hHZ)hHY)$$

$$+ \mu(g(Y,GX)GZ + g(Y,HX)HZ.$$

Now we can state and prove our main theorem.

Theorem 3

Let M be a complex (κ,μ) *-space with* $\kappa < 1$. *Then, for horizontal vector fields* X,Y,Z *and* W, *we have*

$$(\nabla_W R)(X,Y)Z = 0.$$

Proof

For a horizontal fields X,Y,Z and W, we need to compute

$$(\nabla_W R)(X,Y)Z = \nabla_W R(X,Y)Z - R(\nabla_W X,Y)Z$$
$$- R(X,\nabla_W Y)Z - R(X,Y)\nabla_W Z.$$

First, let us compare the coefficients of X in the 4 terms above. From $\nabla_W R(X,Y)Z$ we have

$$W(A(Y,Z)) = g(\nabla_W Y, hZ) + g(Y,\nabla_W hZ)$$
$$+ (1 - \mu/2)(g(\nabla_W Y,Z) + g(Y,\nabla_W Z)).$$

The coefficient of X in $R(X,\nabla_W Y)Z$ is

$$A(\nabla_W Y,Z) = g(\nabla_W Y,hZ) + (1 - \mu/2)g(\nabla_W Y,Z),$$

and in $R(X,Y)\nabla_W Z$ is

$$A(Y,\nabla_W Z) = g(Y,h\nabla_W Z) + (1 - \mu/2)g(Y,\nabla_W Z).$$

So the coefficient of X in $(\nabla_W R)(X,Y)Z$ is $g(Y,(\nabla_W h)Z)$.

By Lemma 3.5 in [11], for horizontal fields W,Z the covariant derivative of h is given by

$$(\nabla_W h)Z = (g(W,hGZ) - (\kappa - 1)g(W,GZ))U$$
$$+ (g(W,hHZ) - (\kappa - 1)g(W,HZ))V$$

and hence $g(Y,(\nabla_W h)Z) = 0$.

In $\nabla_W R(X,Y)Z$ we also have the term $A(Y,Z)\nabla_W X$ but that term also appears in $R(\nabla_W X,Y)Z$ and they cancel each other out.

Similarly the coefficient of Y also vanishes and the term $A(X,Z)\nabla_W Y$ in $\nabla_W R(X,Y)Z$ cancels out with its counterpart in $R(X,\nabla_W Y)Z$.

Similar situation happens with the terms hX and hY.

For the terms with JX, JY and JZ, we need $(\nabla_W J)Z$ and $(\nabla_W hJ)Z$. Since W and Z are horizontal, using Lemma 3.1, part (v) in [11] we can write

$$(\nabla_W J)Z = -\mu u(W)HZ + \mu v(W)GZ = 0,$$

and

$$(\nabla_W hJ)Z = (\nabla_W h)JZ + h(\nabla_W J)Z = (\nabla_W h)JZ.$$

Now, if we compute the coefficient of JX in $(\nabla_W R)(X,Y)Z$ we get

$$g(Y,(\nabla_W hJ)Z) + (1 - \mu/2)g(Y,(\nabla_W J)Z) = 0.$$

Similarly, the coefficients of JY and JZ vanish also.

Differentiating the term with JX we also get

$$-A(Y,JZ)\nabla_W JX + A(Y,JZ)J\nabla_W X = -A(Y,JZ)(\nabla_W J)X = 0.$$

Similarly for JY and JZ.

Same thing happens with the terms hJX, hJY and hJZ.

By Lemma 3.1, part (v) in [11], for horizontal fields X and W we have

$$(\nabla_W G)X = \sigma(W)HX, (\nabla_W H)X = -\sigma(W)GX.$$

So, by differentiating the term GX we get

$$(\mu/2)(g(Y,(\nabla_W G)Z)GX \atop +g(Y,GZ)(\nabla_W G)X) = {(\mu/2)\sigma(W)(g(Y,HZ)GX \atop +g(Y,GZ)HX)}.$$

By differentiating the term HX we get

$$(\mu/2)(g(Y,(\nabla_W H)Z)HX \atop +g(Y,HZ)(\nabla_W H)X) = {-(\mu/2)\sigma(W)(g(Y,GZ)HX \atop +g(Y,HZ)GX)}$$

and they cancel out. Similarly the terms we get from GY and HY, and the terms we get from GZ and HZ cancel each other out.

Same thing happens with the terms hGX and hHX, and with the terms hGY and hHY.

We conclude that, in a complex (κ,μ)-space with $\kappa < 1$, for horizontal vector fields $(\nabla_W R)(X,Y)Z = 0$. $\square$

REFERENCES

1. D. E. Blair, Riemannian Geometry of Contact and Symplectic Manifolds, Birkhauser 2002.

2. D. E. Blair, T. Koufogiorgos and B. J. Papantoniou, A classification of 3–dimensional contact metric manifolds with , Kodai Math. J. 13 (1990), 391–401

3. D. E. Blair, A. Mihai, Symmetry in complex contact geometry, Rocky Mountain J. Math. 42 (2012), no. 2, 451–465

4. D. E. Blair, A. Mihai, Homogeneity and local symmetry of complex –spaces, Israel J. Math. 187 (2012), no. 2, 451–464

5. E. Boeckx, A class of locally –symmetric contact metric spaces, Arch. Math. 72 (1999), 466–472

6. E. Boeckx and L. Vanhecke, Characteristic reflections on unit tangent sphere bundles, Houston J. Math. 23 (1997), 427–448

7. B. Foreman, Variational Problems on Complex Contact Manifolds with Applications to Twistor Space Theory, Thesis, Michigan State University 1996.

8. B. Foreman, Boothby–Wang fibrations on complex contact manifolds, Differential Geom. Appl., 13 (2000), 179––196.

9. S. Ishihara, M. Konishi, Complex almost contact structures in a complex contact manifold, Kodai Math. J., 5 (1982), 30––37.

10. S. Kobayashi, Remarks on complex contact manifolds, Proc. Amer. Math. Soc. 10 (1959), 164––167.

11. B. Korkmaz, A nullity condition for complex contact metric manifolds, J. Geom. 77 (2003), 108––128.

12. T. Takahashi, Sasakian –symmetric spaces, Tohoku Math. J. 29 (1977), 91––113.

NATIONAL & INTERNATIONAL SCIENTIFIC EVENTS

The Minerals, Metals & Materials Society 147th
Annual Meeting & Exhibit (TMS 2018)

Venue: Phoenix Convention Center
Location: Phoenix, Arizona, USA

BEGINS: March 11, 2018
Ends: March 15, 2018

Materials Research Society Spring Meeting &
Exhibit (MRS 2018)

Venue: Phoenix Convention Center
Location: Phoenix, Arizona, USA

BEGINS: April 2, 2018
Ends: April 6, 2018

ASME 2018 Annual Meeting

Venue: JW Marriott parq Vancouver
Location: Vancouver British Columbia , Canada

BEGINS: Jun 2, 2018
Ends: Jun 6, 2018

14th International Conference
On Diffusion In Solids And Liquids (DSL 2018)

Venue: Mercure Hotel Amsterdam City
Location: Amsterdam, The Netherlands

BEGINS: Jun 28, 2018
Ends: Jun 29, 2018

12th International Conference On Advanced
Computational Engineering And Experimenting
(Acex 2018)

Venue: Mercure Hotel Amsterdam City
Location: Amsterdam, The Netherlands

BEGINS: July 1, 2018
Ends: July 5, 2018

ASME Pressure Vessels & Piping Conference
(PVP 2018)

Venue: Hilton Prague
Location: Prague, Czech Republic

BEGINS: July 15, 2018
Ends: July 20, 2018

International Design Engineering Technical
Conferences & Computers & Information in
Engineering Conference (IDETC/CIE 2018)

Venue: Hilton Québec
Location: Québec, Canada

BEGINS: August 26, 2018
Ends: August 29, 2018

7th EuCheMS Chemistry Congress, Molecular
frontiers and global challenges

Venue: ACC Liverpool
Location: Liverpool, UK

BEGINS: August 26, 2018
Ends: August 30, 2018

XXV EFMC International Symposium on Medicinal
Chemistry (EFMC-ISMC 2018)

Venue: Ljubljana Exhibition and Conv. Centre
Location: Ljubljana, Slovenia

BEGINS: September 2, 2018
Ends: September 6, 2018

2018 International Conference on Solid State De-
vices and Materials (SSDM2018)

Venue: Hongo Campus, The University of Tokyo
Location: Tokyo, Japan

BEGINS: September 9, 2018
Ends: September 13, 2018

5th Nuclear Materials Conference (NuMat 2018)

Venue: Motif Seattle
Location: Seattle, WA, USA

BEGINS: Oct 14, 2018
Ends: Oct 18, 2018

19th International Metallurgy and Materials
Congress

Venue: TUYAP Fair, Conv. and Congress Center
Location: İstanbul, Turkey

BEGINS: Oct 25, 2018
Ends: Oct 27, 2018

HİTTİTE